CALCULATION OF KINEMATIC DEPENDENT VARIABLES FOR TRILINEAR HIGGS COUPLING DETERMINATION VIA SINGLE-HIGGS DIFFERENTIAL MEASUREMENTS AT THE CMS EXPERIMENT AT THE LHC

A THESIS SUBMITTED TO
THE GRADUATE SCHOOL OF NATURAL AND APPLIED SCIENCES
OF
MIDDLE EAST TECHNICAL UNIVERSITY

BY

ÖZGÜR DURMUŞ

IN PARTIAL FULFILLMENT OF THE REQUIREMENTS
FOR
THE DEGREE OF MASTER OF SCIENCE
IN
PHYSICS

MAY 2022

Approval of the thesis:

CALCULATION OF KINEMATIC DEPENDENT VARIABLES FOR TRILINEAR HIGGS COUPLING DETERMINATION VIA SINGLE-HIGGS DIFFERENTIAL MEASUREMENTS AT THE CMS EXPERIMENT AT THE LHC

submitted by **ÖZGÜR DURMUŞ** in partial fulfillment of the requirements for the degree of **Master of Science in Physics Department, Middle East Technical University** by,

Prof. Dr. Halil Kalıpçılar
Dean, Graduate School of **Natural and Applied Sciences** _____

Prof. Dr. Seçkin Kürkçüoğlu
Head of Department, **Physics** _____

Prof. Dr. Ali Murat Güler
Supervisor, **Department of Physics** _____

Dr. Ece Aşılar
Co-supervisor, **IN2P3, CNRS** _____

Examining Committee Members:

Prof. Dr. Bayram Tekin
Department of Physics, METU _____

Prof. Dr. Ali Murat Güler
Department of Physics, METU _____

Assoc. Prof. Dr. Deniz Yılmaz
Physics Engineering, Ankara University _____

Date: 11.05.2022

I hereby declare that all information in this document has been obtained and presented in accordance with academic rules and ethical conduct. I also declare that, as required by these rules and conduct, I have fully cited and referenced all material and results that are not original to this work.

Name, Surname: Özgür DURMUŞ

Signature :

ABSTRACT

CALCULATION OF KINEMATIC DEPENDENT VARIABLES FOR TRILINEAR HIGGS COUPLING DETERMINATION VIA SINGLE-HIGGS DIFFERENTIAL MEASUREMENTS AT THE CMS EXPERIMENT AT THE LHC

DURMUŞ, Özgür
M.S., Department of Physics
Supervisor: Prof. Dr. Ali Murat Güler
Co-Supervisor: Dr. Ece Aşılar

May 2022, 146 pages

After the Higgs boson discovery in 2012, it is only natural that experimentalists focus on measuring its properties. Although, various production cross sections and branching ratios have been measured, the trilinear Higgs self-coupling λ_3 is still largely unconstraint. Therefore, it is one of the most significant intense theoretical and experimental activities at LHC. Studying double Higgs production is the standard way for probing λ_3 as it directly depends on the λ_3 at the leading order. However, the cross section of the main production channel i.e. gluon fusion is only around 35 fb^{-1} at 13 TeV while the single Higgs production cross section is around 50 pb^{-1}. To further enhance the sensitivity studying differential dependencies is crucial. The aim of this thesis is to calculate kinematic and process dependent parameters that arise in the case of modified trilinear coupling. The calculated parameters will be provided to the CMS Higgs combination group for vector boson fusion, ttH, VH production modes in bins of transverse momentum of Higgs boson.

Keywords: Higgs coupling, CMS, LHC

ÖZ

BHÇ'DEKİ CMS DENEYİNDE TEK HİGGS DİFERANSİYEL ÖLÇÜMLERİ İLE HİGGS BOZONU ÖZ ÇİFTLENİMİNİN TESPİTİ İÇİN KİNEMATİK BAĞIMLI DEĞİŞKENLERİN HESAPLANMASI

DURMUŞ, Özgür
Yüksek Lisans, Fizik Bölümü
Tez Yöneticisi: Prof. Dr. Ali Murat Güler
Ortak Tez Yöneticisi: Dr. Ece Aşılar

Mayıs 2022 , 146 sayfa

2012'deki Higgs bozonu keşfinden sonra, deneyciler bu yeni bozonun özelliklerini ölçmeye odaklanmistir. Çeşitli üretim tesir kesitleri ve dallanma oranları ölçülmüş olmakla birlikte, Higgs öz etkileşim çiftlenimi λ_3 değeri ölçülememiş mevcut sınırlar ise oldukça zayıftır. Bu nedenle, BHÇ'deki teorik ve deneysel faaliyetlerin en çok odaklanılmış olanlarından biridir. Çift Higgs üretimini incelemek, λ_3'yi araştırmanın standart yoludur, çünkü doğrudan λ_3'ye ilk mertebede bağlıdır. Fakat ana üretim kanalının, yani gluon füzyonunun tesir kesiti 13 TeVde sadece 35 fb^{-1} iken, tek Higgs üretim kesiti 50 $\mathrm{pb}^{-}1$ civarındadır. Bu durumda bahsedilen çiftlenim sabitini ölçmek icin tek Higgs üretimi ve çift Higgs üretiminin birlikte kullanılması en mantıklı yoldur. Duyarlılığı daha da artırmak için kinematik değişkenlerin diferansiyel bağımlılıklarını incelemek çok önemlidir. Bu tezin amacı, değiştirilmiş λ_3 çiftlenim sabiti durumunda ortaya çıkan kinematik ve süreç bağımlı parametreleri hesaplamaktır. Bu parametreler Higgs bozonunun vektör bozon füzyonu, ttH, VH üretim kanalları icin çeşitli dik momentum değer aralıklarında ayrı ayrı hesaplanacaktır. Hesaplanan para-

metreler CMS Higgs kombinasyon grubuna sağlanacaktır.

Anahtar Kelimeler: Higgs çiftlenimi, CMS, BHÇ

To whomever it may concern

ACKNOWLEDGMENTS

I would like to express my deep gratitude to my supervisor Prof. Dr. Ali Murat Guler for his guidance. Also, I have to point out the fact that he kept calm, reasonable and solution oriented in the unexpected events occurred through the end of my studies. This is one the most important reason that I am able to finish my thesis and defend it. I will always be grateful to him.

My co-supervisor and mentor, Dr. Ece Asilar, is the main reason this thesis came into existence. She guided me from start to finish on how to be a researcher and then how to be a better researcher. Although, we worked remotely for the duration of this work, I had never felt that distance between us. I cannot thank her enough, so I have to stop for the moment.

I would like to thank my dear friends Mustafa Tek, Gokhan Alkac, Merve Demirtas and Hikmet Ozsahin for their great support, both on academic and on personal level, not only through this study but also through the years prior to this work. They have always been there for me whenever I need. I am beyond grateful.

Starting from our freshman year, Duygu Gizem Senturk became a very dear friend to me. I would like to thank her for the company she provides even when we are separated by thousands of kilometers. I also have to thank Alper Sevinc and Medya Bayrak Sevinc for their constant friendship and support over the years and through this study.

I need to acknowledge and appreciate the support of my parents, Hacer Durmus and Ali Ahmet Durmus, throughout my education, including this work. I know that I did not make it easy for them from time to time but they have never stopped being by my side and believing in me. I will always be grateful to you for that.

Other than the family in which we were born, we might have another *family* being there for us no matter what happens. I am really lucky to have one. Selin Ayas and Isil Ozge Isik, your support and the psychological comfort you provide got me through every obstacle. I may not have done it without you. Well, I probably would, but nonetheless, thank you.

TABLE OF CONTENTS

LIST OF TABLES

TABLES

LIST OF FIGURES

FIGURES

LIST OF ABBREVIATIONS

LHC	Large Hadron Collider
CMS	Compact Muon Solenoid
SM	Standard Model
BSM	Beyond Standard Model
QFT	Quantum Field Theory
QCD	Quantum Chromodynamics
QED	Quantum Electrodynamics
STXS	Simplified Template Cross Section
EW	Electroweak
EWSB	Electroweak Symmetry Breaking
VEV	Vacuum Expectation Value
VBF	Vector Boson Fusion
ggF	Gluon-Gluon Fusion
PDF	Parton Distribution Function
LO	Leading Order
NLO	Next-to-Leading Order
UFO	Universal FeynRules Output
C.L.	Confidence Level

CHAPTER 1

INTRODUCTION

In 2012, the long awaiting discovery of Higgs boson has been made at the LHC [1, 2]. Since then, physicists have been studying the properties of Higgs, as predicted by the Standard Model, relentlessly. Several production cross sections and branching ratios have been measured, yet the trilinear Higgs self-coupling, λ_3, is still largely unconstrained. The Higgs self-coupling refers to the interaction of the Higgs boson with itself. Then, trilinear Higgs coupling means that three Higgs bosons interacting with each other.

The importance of the trilinear Higgs coupling and putting constraints on it can be understood through a historical example as mentioned in [3]. In 1977 Lee, Quigg and Thacker realized that a theory without a Higgs field, tree-level unitarity is violated in UV region via the scattering of longitudinally polarized W and Z bosons. They used this fact for finding a model-independant upper bound on the scale of the Higgs sector. Starting from their work, this bound is refined in many times such as [4, 5]. These studies were used for setting the energy scale of the LHC, therefore paved the way for the discovery of the Higgs boson. For the discussion at hand, provided that all the observed couplings have the exact same values as predicted by the SM, the use of the current minimal theory with the observed particles can be extrapolated to large energy scales in a consistent manner. However, this brings the fact that the deviations from SM predictions leads to novel physics, as the existence of massive W and Z bosons leaded to the scale of the Higgs sector. Therefore, the need of the precise measurement of the trilinear Higgs coupling, λ_3, is abundantly clear. If there is any deviation in λ_3 from its SM value, then we expect a *new* physics as a result.

The most obvious way of measuring Higgs self-coupling is to study the double Higgs

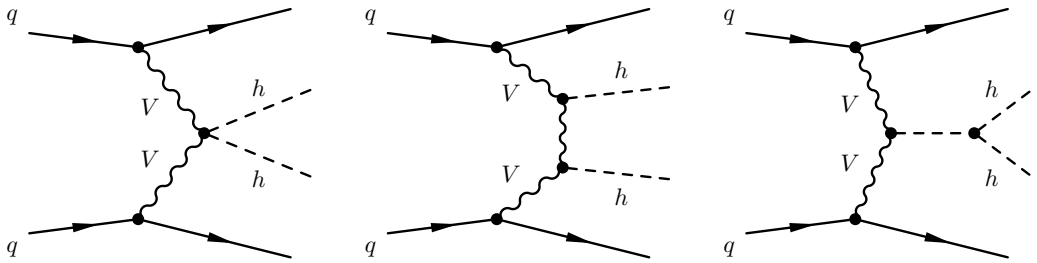

Figure 1.1: Leading order Feynman diagram of double Higgs production through VBF channel

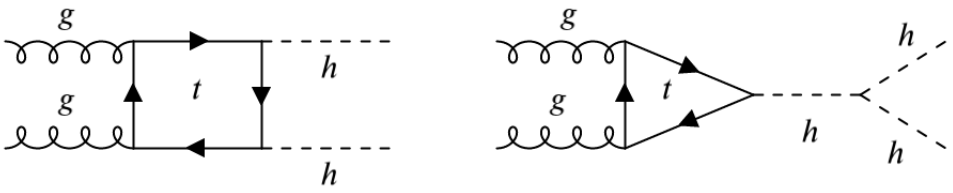

Figure 1.2: Leading order Feynman diagram of double Higgs production through ggF channel

production. The reason for that is the contribution on trilinear coupling of double Higgs production is on tree-level (see Fig. 1.1, taken from [6]). Except, the ggF channel of which the LO contributions are on one-loop level as in Fig. 1.2 (the figure is taken from [7]). For the single Higgs production, the contributions comes from the one-loop EW corrections (Fig. 2.5). Again, except from the ggF channel (Fig. 2.4). Its contributions to single Higgs coupling comes from two-loop corrections. However, the dominant channel of the double Higgs production, ggF, has a cross section about 35 fb^{-1} [8, 9, 10]. On the other hand, single Higgs production channels have a cross section about 50 pb^{-1} [11]. Therefore, single Higgs channel contributions to the Higgs self-coupling is expected to be easier to observe and measure. The combination of both channels, however, is the way best to further constraint λ_3.

An indirect approach to constrain the single Higgs coupling proposed for e^+e^- colliders in [12]. The proposition is made for associated Higgs production, *i.e.* $e^+e^- \longrightarrow HZ$ or $e^+e^- \longrightarrow HZZ$. This approach utilizes the fact that the cross-section is indirectly sensitive to the Higgs coupling at NLO. The model dependency of the approach limits its applications, however it is shown that there are specific channels where the

NLO effects dominate the LO contributions. Therefore, it is possible to constrain the Higgs coupling with this indirect method. A similar idea is adapted to pp-colliders, described in [13, 14, 15]. It is shown that it is possible to further constraint the trilinear Higgs coupling via single Higgs channels via precise EW measurements [16, 17]. The method is to measure the parameter C_1 , which has process and kinematic dependencies and exploit those dependencies by measuring the parameter in different bins of phase space for each single Higgs production channel. The main purpose of this study is to study the production channels, the calculation method of C_1 and automatizing the calculation in STXS bins.

During the development of this thesis, the status of the work at that time was presented to Higgs Combination Group [18], to CMS France [19] and to the CMS Lyon Group [20]. The well-received community reaction and interest was highly motivating and appreciated.

In this thesis we first present some theoretical and phenomenological background of the Standard Model, the Higgs mechanism and the Higgs couplings in Chapter 2. Then, in Chapter 3, experimental background for the Higgs coupling and its measurements are reported. Also, the technical role of the CMS detector is introduced. The method of calculation of the single Higgs coupling using MADGRAPH5_AMC@NLO is introduced in Chapter 4. Automatizing the code to study the coupling in STXS bins are also discussed. In Chapter 5 the results of this study are reported and discussed. In the last chapter, Chapter 6, the conclusion remarks of this thesis are given.

CHAPTER 2

THE STANDARD MODEL AND THE HIGGS MECHANISM

2.1 The Standard Model

The Standard Model (SM) is the best model at hand, describing the elementary particles and their interactions. SM is developed using Quantum Field Theory, which is described in [21] as a theoretical framework combining the principle of relativity, the concept of field and the quantum theory. Particles in SM are described as the excitations of the corresponding fields. The fields are divided into two types, fermions and bosons. The former is called matter fields as well since it describes the the particles that constructs the matter in the universe. So, the fluctuations in fermion field are called fermions, and the fluctuations in boson fields are called bosons. Former obeys the Fermi-Dirac statistics while the latter obeys the Bose-Einstein statistics. One particular difference of fermions and bosons are their spin values. Fermions have half integer spin values $s = \pm\frac{1}{2}$,, while bosons have integer values of spin as $s = 0$ and 1.

Fermions can be divided into two groups as *quarks* and *leptons*. The main difference of quarks and leptons is that while leptons exists on their own, quarks cannot. Leptons interacts through electromagnetic and weak interactions. Quarks, in addition to electromagnetic and weak interactions, are sensitive to strong force as well. They have to constitute bound states. The bound state of a quark and an anti-quark is called a *meson* like $\pi^0, \pi^\pm$ or κ^0 and $\kappa^\pm$ and the bound state of 3 quarks is called as a *baryon* like proton and neutron. Together, mesons and baryons are called *hadrons*.

The Higgs boson is a spin-0 scalar boson, differs from the other vector (or gauge) bosons with its function as well. It is basically responsible for giving mass to particles [22, 23]. The masses of the fundamental particles are proportional to the strength of

their coupling with Higgs, *i.e.* how strong they interact with the Higgs field.

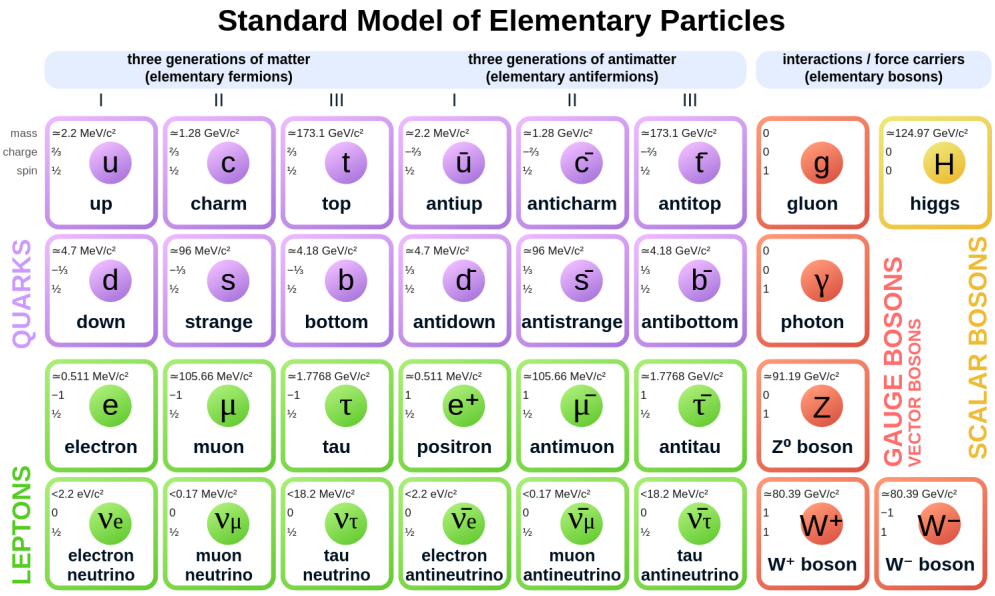

Figure 2.1: Standard Model Elementary Particles

In SM of particle physics there are 3 fundamental interactions, Strong, Weak and Electromagnetic interactions. The theory explaining the strong interaction is called Quantum Chromodynamics (QCD). The other two interactions can be merged into one and called Electroweak interaction. Therefore, all the single Higgs production channels can have QCD and QED vertices.

EW interactions, however, are not affected by colour charges or gluons for that matter. The mediator of the EW fields are W^+, W^- and Z bosons (for weak interactions) and photons (for electromagnetic interactions). The Higgs boson is the product of a process called Electroweak Symmetry Breaking (EWSB).

QCD interactions are considered for the particles having so called colour charge. There are only gluons, the constituents of hadrons, carry colour charge. The color charges of quarks and gluons consist of the three primary colors, red, green and blue. These colors not related to the colors of our daily life. It is just an analogy, but it also has a purpose. Since we can observe only $colorless$ states, this analogy can help us visualize that. One key difference of QCD from QED is its mediators have charge. In QED, we know that photons do not carry charge, so there is no vertex of only photons, *i.e.* no cubic term of the gauge field in the QED Lagrangian. Another way

of saying that is gluons may interact with each other in Quantum Chromodynamics. We do not see this in photons. They do not interact with each other. In p-p Colliders such as LHC, QCD interactions have great importance and should be considered for each process, when quarks and gluons are a part of the process.

In a group theoretical view, SM has a $SU(3) \otimes SU(2) \otimes U(1)$ symmetry that can be spontaneously broken. The broken part is $SU(2) \otimes U(1)$, which is the group of Electroweak interactions. With that, *almost* all observed phenomena in particle physics can be explained.

2.2 Gauge Symmetries

Symmetries in physics have an important role. Physicists seek symmetries in their theories and of the breaking of those symmetries are searched as well. Both situations have different significance. In most basic terms, symmetries in the action of any theory in physics states that there has to be a conserved charge associated to the symmetry. This is called as Noether's Theorem [24]. The breaking of the symmetries also gives rise to other physical quantities to study and understand. Some examples of those symmetries are Parity, Charge Conjugation and Time Reversal symmetries. Together, the symmetry of the combination is called CPT symmetry and it is the strongest symmetry of QFT. However, separately, they do not have to be conserved and whenever the symmetry is broken, as in CP violation, it gives rise to a *new* physics that makes our understanding of the universe deeper and deeper.

Noether's Theorem is valid for classical systems as well. The symmetry in translation of time is associated with conservation of energy, the symmetry in translation of space with conservation of momentum and so on. The breaking of those of symmetries, such as in translation of space gives rise to a net force of a body, Newton's 2^{nd} Law of Motion.

In our context, gauge symmetries are symmetries of transformations of fields that are commutative with space-time. There are no non-trivial conserved charge of gauge symmetries, *i.e.* there are still conserved charges following Noether's theorem but all of them are zero [25].

QED and QCD of SM are gauge theories, meaning they have gauge symmetries. In order to understand the Higgs mechanism and EWSB, we shal investigate the $U(1)$ and $SU(2)$ Gauge symmetries of Electroweak theory.

2.2.1 The U(1) Gauge Symmetry

In this section, we shall investigate the local gauge symmetry of QED in order to understand the QED Lagrangian. An electron can be represented by the field $\psi(x)$ and positron $\bar{\psi}(x)$ with the transformations;

$$\psi(x) \longrightarrow e^{i\alpha(x)}\psi(x) \tag{2.1a}$$

$$\bar{\psi}(x) \longrightarrow e^{-i\alpha(x)}\bar{\psi}(x) \tag{2.1b}$$

For the system of electrons and positrons, we have the Dirac Equation, and the corresponding Lagrangian is;

$$\mathcal{L} = i\bar{\psi}\gamma^{\mu}\partial_{\mu}\psi - m\bar{\psi}\psi \tag{2.2}$$

However, this Lagrangian is not invariant under the transformations in Eq. 2.1a and 2.1b. The term causes the non-invariance is the derivative of the field and the reason is α depends on space-time. Under the unitary transformation, the field derivative transforms as;

$$\partial_{\mu}\psi \longrightarrow e^{i\alpha(x)}\partial_{\mu}\psi(x) + ie^{i\alpha(x)}\psi(x)\partial_{\mu}\alpha \tag{2.3}$$

and the Lagrangian becomes;

$$\mathcal{L} = i\bar{\psi}\gamma^{\mu}\partial_{\mu}\psi - \bar{\psi}\gamma^{\mu}\psi\partial_{\mu}\alpha - m\bar{\psi}\psi \tag{2.4}$$

What we need is a derivative operator transforms with the field such that;

$$D_\mu \psi \longrightarrow e^{i\alpha(x)} D_\mu \psi \tag{2.5}$$

D_μ is called as covariant derivative and it is defined as;

$$D_\mu \equiv \partial_\mu - ieA_\mu \tag{2.6}$$

where A_μ is the gauge field needed for the invariance. It is transformed as;

$$A_\mu \longrightarrow A_\mu + \tfrac{1}{e}\partial_\mu \alpha \tag{2.7}$$

Then the Lagrangian can be written as;

$$\mathcal{L} = i\bar{\psi}\gamma^\mu D_\mu \psi - m\bar{\psi}\psi \tag{2.8}$$

However, the gauge field is not physical since there is no kinetic term, $\partial_\mu \Psi$. We need to add the kinetic term by hand in order to make it a physical quantity, which will be photon field. For the sake of invariance, the kinetic term should only include the gauge field. Thus, we come up with the kinetic term;

$$F^{\mu\nu}F_{\mu\nu} = \partial_\mu A_\nu - \partial_\nu A_\mu \tag{2.9}$$

Adding this final term gives us the gauge invariant Lagrangian of QED,

$$\mathcal{L} = i\bar{\psi}\gamma^\mu D_\mu \psi - m\bar{\psi}\psi - \tfrac{1}{4}F_{\mu\nu}F^{\mu\nu} \tag{2.10}$$

or, it can be written in a more explicit form so that the photon field can be recognized easily;

$$\mathcal{L} = \bar{\psi}(i\gamma^\mu \partial_\mu - m)\psi + e\bar{\psi}\gamma^\mu A_\mu \psi - \tfrac{1}{4}F_{\mu\nu}F^{\mu\nu} \tag{2.11}$$

2.2.2 The Spontaneous Symmetry Breaking and The Higgs Mechanism

In SM description of particle physics, the particles are massless. However, by introducing a scalar field, the symmetry of the theory is spontaneously broken. This, eventually gives the raise of the mass terms for the particles that interact with this scalar field.

2.2.3 An example with a real scalar field

The spontaneous symmetry breaking can be examined by investigating the simplest renormalizable scalar field Lagrangian. Let $\mathcal{L}$ be the Lagrangian, describing a system with only scalar particles. Then,

$$\begin{aligned} \mathcal{L} &= T - V \\ &= \frac{1}{2}(\partial_\mu \Phi)(\partial^\mu \Phi) - \left(\frac{1}{2}\mu^2(\Phi^\dagger \Phi) + \frac{1}{4}\lambda(\Phi^\dagger \Phi)^2\right) \end{aligned} \tag{2.12}$$

This is the simplest Lagrangian because for the a renormalizable $\mathcal{L}$, since we need a reflection symmetry, *i.e.* $\Phi \longrightarrow -\Phi$ should not change the Lagrangian. Note that the higher order of the field terms are omitted for simplicity. This can be considered as a low energy approximation. The potential term of that Lagrangian is the following;

$$\begin{aligned} V(\Phi) &= \frac{1}{2}\mu^2(\Phi^\dagger \Phi) + \frac{1}{4}\lambda(\Phi^\dagger \Phi)^2 \\ &= \frac{1}{2}\mu^2 \Phi^2 + \frac{1}{4}\lambda \Phi^4 \end{aligned} \tag{2.13}$$

There are two possible forms of this potential with $\lambda > 0$ and $\mu^2 > 0$ or $\mu^2 < 0$. Both possibilities are shown in Fig. 2.2 (the figure is taken from [26]. On the left, Fig. 2.2a is the case where $\mu^2 > 0$ and on the right, Fig. 2.2b where $\mu^2 < 0$. There

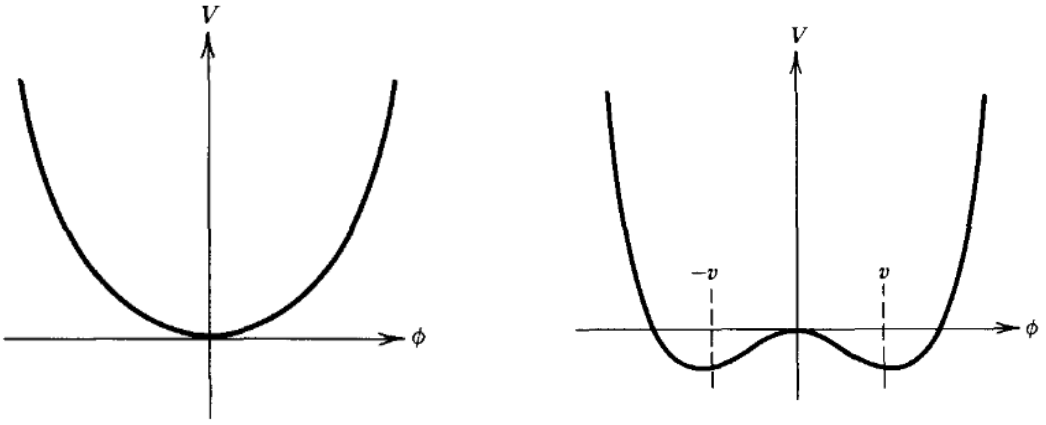

(a) $\mu^2 > 0, \lambda > 0$

(b) $\mu^2 < 0, \lambda > 0$

Figure 2.2: The possible shapes of the potential in 2.13

are 3 extrema of the potential in case 2.2b;

$$\Phi = 0 \tag{2.14a}$$

$$\Phi = \pm\sqrt{\frac{-\mu^2}{\lambda}} \tag{2.14b}$$

where, Eq. 2.14a is the local maximum of the the potential. *Note* that this is not the ground state of the potential. By defining $v = \sqrt{\frac{-\mu^2}{\lambda}}$, either $+v$ or $-v$ can be chosen as the ground state. This choice is completely arbitrary, but important to apply the perturbation theory. Then, the field parameter should be re-defined as;

$$\eta = \Phi \pm v \tag{2.15}$$

Substituting the new field variable η into the old one Φ in Eq.2.13 gives;

$$\mathcal{L}' = \frac{1}{2}(\partial_\mu \eta)(\partial^\mu \eta) - \lambda v^2 \eta^2 \pm \lambda v \eta^3 - \frac{1}{4}\lambda \eta^4 + \frac{1}{2}\lambda v^4 \tag{2.16}$$

The choice of the coefficients in Eq. 2.13 may seem arbitrary at first but this serves a simple purpose. If one sets the coefficients of the terms as a and b, it can be seen easily that the linear term disappears with these coefficients only.

One important observation can be made regarding this transformation. A transformation like Eq.2.15 does not change the physics, therefore both $\mathcal{L}$ and $\mathcal{L}'$ are equivalent. However, since we need to apply perturbation theory to the given Lagrangians and the minimum of the potential in $\mathcal{L}$ is not the ground state, perturbation theory does not apply. This is the reason we use $\mathcal{L}'$, instead of $\mathcal{L}$ so that we can get the correct picture.

From the Lagrangian $\mathcal{L}'$, ignoring the constant term for simplicity, since any constant term of a Lagrangian would not cause a physical affect, the potential of the new field can be written as;

$$V(\eta) = \lambda v^2 \eta^2 \mp \lambda v \eta^3 + \frac{1}{4}\lambda \eta^4 \tag{2.17}$$

Therefore, the mass term for the field η can be defined as;

$$\begin{aligned} m_\eta &\equiv \sqrt{2\lambda v^2} \\ &\equiv \sqrt{-\mu^2} \end{aligned} \tag{2.18}$$

This *spontaneous* symmetry breaking gives rise to a mass term for the field η which was not apparent in $\mathcal{L}$.

2.2.4 An example with a complex scalar field with global symmetry

In order to complete the discussion we should check the complex scalar field as well. For a complex scalar field $\Phi = (\Phi_1 + i\Phi_2) \,/\, \sqrt{2}$, the Lagrangian can be written as;

$$\mathcal{L} = (\partial_\mu \Phi)^* (\partial^\mu \Phi) - \mu^2 \Phi^* \Phi - \lambda (\Phi^* \Phi)^2 \tag{2.19}$$

This Lagrangian has the $U(1)$ global gauge symmetry, *i.e.* it is invariant under the gauge transformation of $\Phi \longrightarrow e^{i\alpha}\Phi$. If Φ is substituted into Eq.2.19;

$$
\begin{aligned}
\mathcal{L} &= \frac{1}{2}[\partial_\mu(\Phi_1 + i\Phi_2)]^*[\partial^\mu(\Phi_1 + i\Phi_2)] - \frac{\mu^2}{2}[(\Phi_1 - i\Phi_2)(\Phi_1 - i\Phi_2)] \\
&\quad - \frac{\lambda}{4}[(\Phi_1 - i\Phi_2)(\Phi_1 - i\Phi_2)]^2 \\
&= \frac{1}{2}[(\partial_\mu\Phi_1)^* - i(\partial^\mu\Phi_2)^*][\partial_\mu\Phi_1 + i\partial^\mu\Phi_2] - \frac{\mu^2}{2}(\Phi_1^2 + \Phi_2^2) \\
&\quad - \frac{\lambda}{4}(\Phi_1^2 + \Phi_2^2)^2 \\
&= \frac{1}{2}(\partial_\mu\Phi_1)^*(\partial^\mu\Phi_1) + \frac{1}{2}(\partial_\mu\Phi_2)^*(\partial^\mu\Phi_2) - \frac{\mu^2}{2}(\Phi_1^2 + \Phi_2^2) \\
&\quad - \frac{\lambda}{4}(\Phi_1^2 + \Phi_2^2)^2
\end{aligned}
$$

which finally becomes;

$$
\mathcal{L} = \frac{1}{2}(\partial_\mu\Phi_1)^2 + \frac{1}{2}(\partial_\mu\Phi_2)^2 - \frac{\mu^2}{2}(\Phi_1^2 + \Phi_2^2) - \frac{\lambda}{4}(\Phi_1^2 + \Phi_2^2)^2 \tag{2.20}
$$

As we did for the real scalar field, we look for the extrema of the potential term of the Lagrangian so that we can find the minima. The potential term is,

$$
V = \frac{\mu^2}{2}(\Phi_1^2 + \Phi_2^2) + \frac{\lambda}{4}(\Phi_1^2 + \Phi_2^2)^2 \tag{2.21}
$$

Taking derivative of V, with respect to either Φ_1 or Φ_2 and equating it to zero gives,

$$
\Phi_{1,2} = 0 \tag{2.22a}
$$

$$
\Phi_1^2 + \Phi_2^2 = -\mu^2/\lambda = v^2 \tag{2.22b}
$$

The Eq.2.22b describes a circle of minima (Figure 2.3). This means that in the (Φ_1, Φ_2) plane, the minima of the potential is a circle with radius v. Then the choice of direction for the vacuum is arbitrary again. For simplicity, let $\Phi_1 = v$ and $\Phi_2 = 0$. Similarly to the real scalar field example, the Lagrangian is expanded around the vacuum by introducing two new field parameters this time, so that;

$$
\Phi = \sqrt{\tfrac{1}{2}}(v + \eta + i\xi) \tag{2.23}
$$

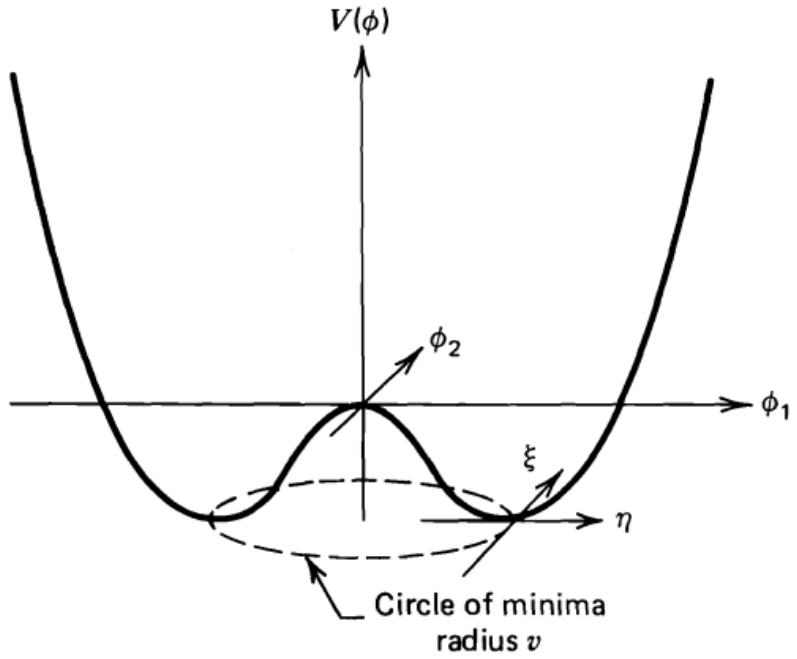

Figure 2.3: Potential $V(\Phi)$ of a complex scalar field with $\lambda > 0$ and $\mu < 0$

Substituting Eq.2.23 into Eq.2.20, one gets;

$$\begin{aligned}\mathcal{L}' &= \frac{1}{2}(\partial_\mu \xi)^2 + \frac{1}{2}(\partial_\mu \eta)^2 - \frac{\mu^2}{2}(v+\eta-i\xi)(v+\eta+i\xi) \\ &\quad - \frac{\lambda}{4}[(v+\eta-i\xi)(v+\eta+i\xi)]^2 \\ &= \frac{1}{2}(\partial_\mu \xi)^2 + \frac{1}{2}(\partial_\mu \eta)^2 - \frac{\mu^2}{2}\left((v+\eta)^2+\xi^2\right) - \frac{\lambda}{4}\left((v+\eta)^2+\xi^2\right)^2\end{aligned}$$

and, with careful calculations, the Lagrangian $\mathcal{L}'$ becomes;

$$\begin{aligned}\mathcal{L}' &= \tfrac{1}{2}(\partial_\mu \xi)^2 + \tfrac{1}{2}(\partial_\mu \eta)^2 + \mu^2\eta^2 - \lambda v\eta^3 - \lambda v\eta\xi^2 \\ &\quad - \frac{\lambda}{2}\eta^2\xi^2 - \frac{\lambda}{4}\eta^4 - \frac{\lambda}{4}\xi^4 + \frac{\mu^4}{4\lambda}\end{aligned} \tag{2.24}$$

The first two terms of the Lagrangian are kinetic terms of the fields η and ξ. The third term has the mass term for the field η, which is $m_\eta = \sqrt{-2\mu^2}$. The difference from the real scalar example, is that there is no mass term for ξ-field. This means we have a massless boson, called as Goldstone boson. The problem of having the

Goldstone boson in the theory is that we want to generate massive bosons by spontaneously breaking the gauge symmetry, yet we cannot. This is in fact an example of the Goldstone theorem which states that whenever a continuous symmetry of a physical system spontaneously broken, we get massless scalars. We do not achieve the desired result of having a theory of weak interactions with massive gauge bosons by breaking the global gauge symmetry. We should then investigate the local gauge symmetry.

2.2.5 An example with a complex scalar field with local gauge symmetry

In order to understand the local gauge symmetry, one can start with the simplest example, $U(1)$ symmetry. The gauge transformation is similar to the global one with the difference of the space-time dependence of the phase α such that, $\Phi \longrightarrow e^{i\alpha(x)}\Phi$. However, Eq.2.19 is not invariant under this transformation. This can be seen by applying the transformation to Eq.2.19,

$$\begin{aligned}\mathcal{L} = (\partial_\mu\Phi)^*(\partial^\mu\Phi) + i(\partial_\mu\Phi)^*\Phi\partial^\mu\alpha(x) - i\Phi^*(\partial^\mu\Phi)\partial_\mu\alpha(x) \\ + \Phi^*\Phi\partial_\mu\alpha(x)\partial^\mu\alpha(x) - \mu^2\Phi^*\Phi - \lambda(\Phi^*\Phi)^2\end{aligned} \tag{2.25}$$

The non-invariance comes from the locality of the phase α. This problem is almost identical with the one we had in 2.2.1. Then we shall implement the same solution, introducing a covariant derivative;

$$D_\mu \equiv \partial_\mu - ieA_\mu \tag{2.26}$$

transforming with the field such that;

$$D_\mu\Phi \longrightarrow e^{i\alpha(x)}D_\mu\Phi \tag{2.27}$$

and the gauge field introduced in covariant derivative transforms as,

$$A_\mu \longrightarrow A_\mu + \tfrac{1}{e}\partial_\mu\alpha \tag{2.28}$$

The only missing term is the kinetic term of the gauge field with the same definition;

$$F^{\mu\nu}F_{\mu\nu} = \partial_\mu A_\nu - \partial_\nu A_\mu \tag{2.29}$$

Then we have the complete picture for the *spontaneous* breaking of the $U(1)$ symmetry.

The invariant Lagrangian is, then,

$$\mathcal{L} = (\partial^\mu + ieA^\mu)\Phi^*(\partial_\mu - ieA_\mu)\Phi - \mu^2\Phi^*\Phi - \lambda(\Phi^*\Phi)^2 - \tfrac{1}{4}F_{\mu\nu}F^{\mu\nu} \tag{2.30}$$

Then, we shall repeat the procedure in the Section 2.2.4.

Let Φ be;

$$\Phi = (v + \eta + i\xi) \,/\, \sqrt{2}$$

and substitute in Eq.2.30, which gives;

$$\begin{aligned}\mathcal{L}' = {} & \tfrac{1}{2}(\partial_\mu\xi)^2 + \tfrac{1}{2}(\partial_\mu\eta)^2 - v^2\lambda\eta^2 + \tfrac{1}{2}e^2v^2A_\mu A^\mu \\ & - evA_\mu\partial^\mu\xi - \tfrac{1}{4}F_{\mu\nu}F^{\mu\nu} + \text{interaction terms}\end{aligned} \tag{2.31}$$

where the ξ-field corresponds to the Goldstone bosons. There is also another problem with this Lagrangian. The gauge filed A_μ has also a mass of $m_A = ev$. The reason this is a problem is the fact that just by re-defining the field variables, we raised the the polarization degrees of freedom by 1. Therefore, there is a nonphysical field which must be got rid of by applying another gauge transformation. This way, the extra degree of freedom will be gone. In order to do that, we should first realize that;

$$\begin{aligned}\Phi &= \tfrac{1}{2}(v + \eta + i\xi) \\ &\simeq \tfrac{1}{2}(v + \eta)e^{i\xi/v}\end{aligned} \tag{2.32}$$

for the lowest order in ξ. Then, we can re-define the field variables in the form as Eq.2.32,

$$\Phi = \tfrac{1}{2}(v + h(x))e^{i\theta(x)/v} \tag{2.33}$$

and the gauge field transforms, in terms of the new field variables, as

$$A_\mu \longrightarrow +\tfrac{1}{ev}\partial_\mu\theta \tag{2.34}$$

Substituting Eq.2.33 and Eq.2.34 into the Lagrangian in Eq.2.31 gives;

$$\begin{aligned}\mathcal{L}'' = \tfrac{1}{2}(\partial_\mu h)^2 - \lambda v^2 h^2 + \tfrac{1}{2}e^2 v^2 A_\mu^2 - \lambda v h^3 - \tfrac{1}{4}\lambda h^4 \\ + \tfrac{1}{2}e^2 A_\mu^2 h^2 + v e^2 A_\mu^2 h - \tfrac{1}{4}F_{\mu\nu}F^{\mu\nu}\end{aligned} \tag{2.35}$$

The Lagrangian $\mathcal{L}''$ has no Goldstone bosons. It has only two massive fields interacting with each other. The h-field is what is called a Higgs field and the field A_μ is the gauge boson of the theory. Note that the field parameter of Goldstone boson become the polarization parameter of the gauge boson. This is what is called as the *Higgs mechanism*.

Since we know that the Electroweak theory has $U(1) \otimes SU(2)$ symmetry, it is necessary to study the local SU(2) symmetry breaking as well.

2.2.6 An example with a complex scalar field having local SU(2) symmetry

In order to deal with the complex field, we may start with the following Lagrangian,

$$\mathcal{L} = (\partial_\mu\phi)^\dagger(\partial^\mu\phi) - \mu^2\phi^\dagger\phi - \lambda(\phi^\dagger\phi)^2 \tag{2.36}$$

where ϕ is a SU(2) doublet of complex scalar fields. It is defined as;

$$\begin{aligned}\phi &= \begin{pmatrix}\phi_\alpha \\ \phi_\beta\end{pmatrix} \\ &= \tfrac{1}{2}\begin{pmatrix}\phi_1 + i\phi_2 \\ \phi_3 + i\phi_4\end{pmatrix}\end{aligned} \tag{2.37}$$

As it is done before the local gauge invariance must be tested under the transformation,

$$\phi \longrightarrow e^{i\alpha_a(x)\tau_a/2}\phi$$

By doing the transformation we realize that we need a covariant derivative in order to have gauge invariance. We can define the covariant derivative as;

$$D_\mu = \partial_\mu + ig\frac{\tau_a}{2}W_\mu^a \tag{2.38}$$

where τ_a are set of linearly independent traceless 2×2 matrices,

$$T_1 = \begin{pmatrix}0 & i \\ i & 0\end{pmatrix},\ T_2 = \begin{pmatrix}0 & -1 \\ 1 & 0\end{pmatrix},\ T_3 = \begin{pmatrix}i & 0 \\ 0 & -1\end{pmatrix} \tag{2.39}$$

and the three gauge fields are W_μ^a, $a = 1, 2, 3$, the summation over a is implied. They transform as;

$$\boldsymbol{W}_\mu \longrightarrow \boldsymbol{W}_\mu - \frac{1}{g}\partial_\mu\boldsymbol{\alpha} - \boldsymbol{\alpha} \times \boldsymbol{W}_\mu \tag{2.40}$$

and the field ϕ transforms as;

$$\phi(x) \longrightarrow (1 + \boldsymbol{\alpha}(x) \cdot \boldsymbol{\tau}/2)\phi(x) \tag{2.41}$$

Combining all these (Equations 2.36 - 2.41), one get the gauge invariant Lagrangian as;

$$\begin{aligned}\mathcal{L}' = &\left(\partial_\mu\phi + ig\tfrac{1}{2}\boldsymbol{\tau}\cdot\boldsymbol{W}_\mu\phi\right)^\dagger\left(\partial^\mu\phi + ig\tfrac{1}{2}\boldsymbol{\tau}\cdot\boldsymbol{W}^\mu\phi\right)\\ &-\mu^2\phi^\dagger\phi - \lambda(\phi^\dagger\phi)^2 - \frac{1}{4}\boldsymbol{W}_{\mu\nu}\cdot\boldsymbol{W}^{\mu\nu}\end{aligned} \tag{2.42}$$

where the kinetic energy term is,

$$\boldsymbol{W}_{\mu\nu} = \partial_\mu\boldsymbol{W}_\nu\partial_\nu\boldsymbol{W}_\mu - g\boldsymbol{W}_\mu\times\boldsymbol{W}_\nu \tag{2.43}$$

The last term is due to the non-abelian nature of the theory. A non-abelian group can be defined simply by the fact that its matrices do not commute with each other. The non-commutative terms in our theory are τ's.

As it is done before, the minima of the potential can be found as;

$$\Phi_{1,2,3,4} = 0 \tag{2.44a}$$

$$\Phi_1^2 + \Phi_2^2 + \Phi_3^2 + \Phi_4^2 = -\frac{\mu^2}{\lambda} \equiv v^2 \tag{2.44b}$$

Any minimum of the potential can be obtained,

$$\phi_1 = \phi_2 = \phi_4 = 0 \tag{2.45a}$$

$$\phi_3 = -\frac{\mu^2}{\lambda} \tag{2.45b}$$

This is basically the same as the symmetry breaking in the sense that the symmetry does not explicit anymore. We need to expand around the chosen vacuum state, which is;

$$\phi_0 \equiv \frac{1}{2}\begin{pmatrix}0\\ v\end{pmatrix} \tag{2.46}$$

We have the state;

$$\phi(x) = \frac{1}{2}\begin{pmatrix} 0 \\ v + h(x) \end{pmatrix} \tag{2.47}$$

Substituting Eq.2.47 into Eq.2.42 gives a *small* problem. There is no field other than h(x) remains. To check whether we loss any generality, similar to the previous section, we parametrize the vacuum fluctuations in terms of 4 scalar fields, such that;

$$\phi(x) = \frac{1}{2}e^{i\boldsymbol{\tau}\cdot\boldsymbol{\theta}(x)/v}\begin{pmatrix} 0 \\ v + h(x) \end{pmatrix} \tag{2.48}$$

where $\boldsymbol{\tau}$ are T_a and the scalar fields $\boldsymbol{\theta}$ are θ_a, $a = 1, 2, 3$ and we check the small perturbations around the vacuum;

$$\phi(x) = \frac{1}{2}\begin{pmatrix} 1 + i\theta_3/v & i(\theta_1 - i\theta_2)/v \\ i(\theta_1 + i\theta_2)/v & 1 - i\theta_3/v \end{pmatrix}\begin{pmatrix} 0 \\ v + h(x) \end{pmatrix} \tag{2.49}$$

This is simply,

$$\phi(x) = \frac{1}{2}\begin{pmatrix} \theta_2 + i\theta_1 \\ v + h + i\theta_3 \end{pmatrix} \tag{2.50}$$

This shows that the fields have independent deviations from the vacuum. We, now, have a Lagrangian that is locally SU(2) invariant. Then, it is possible to *gauge* the three massless scalar fields $\theta_{1,2,3}$ so that we get rid of the Goldstone bosons.

All the examples studied here shows that we can have a broken EWSB with only one massive gauge boson, *i.e.* Higgs.

2.3 Trilinear Higgs Coupling

In previous section, we got potential that have the same form with what we will call the Higgs potential. For example, in Eq.2.17, Eq.2.31 or Eq.2.35 all have potentials

in the same form with Higgs potential, which is, in low energies;

$$V(H) = \frac{1}{2}m_H^2 H^2 + \lambda_3 v H^3 + \frac{1}{4}\lambda_4 H^4 + O(H^5), \tag{2.51}$$

where m_H is the Higgs mass and λ_3 is the trilinear Higgs coupling, v is the vacuum expectation value with the approximate value of 246 GeV.

We study the trilinear Higgs coupling with the assumption is that the new physics affects only λ_3. If the parameter λ_3 deviates from the SM values, we can re-define the coupling value as $\lambda_3 = \kappa_\lambda \lambda_3^{SM}$, where λ_3^{SM} is the SM trilinear Higgs coupling and λ_3 is the so-called Beyond Standard Model (BSM) coupling value. Therefore, κ_λ is defined as a scaling factor.

For a generic observable, the cross-section or decay width can be written as,

$$\Sigma_{\lambda_3}^{\mathrm{BSM}} = Z_H^{\mathrm{BSM}} \Sigma_{\mathrm{LO}} (1 + \kappa_\lambda C_1 + \delta Z_H) \tag{2.52}$$

where Σ is the observed value, Z_H^{BSM} is the renormalization of the wave function and C_1 is the process and kinematic dependant part of the observable.

$$C_1 = \frac{2\Re(\mathcal{M}^{0*}\mathcal{M}^1_{\lambda_3^{\mathrm{SM}}})}{|\mathcal{M}^0|^2}\,, \tag{2.53}$$

where, $\mathcal{M}^0$ is the LO amplitude of a given process. Let $\mathcal{M}^1$ be the virtual EW amplitude. Then, $\mathcal{M}^1$ involves the one-loop contributions for the processes having tree-level diagrams as LO, and two-loop contributions for the ones having one-loop diagrams as leading order. Most of all the production channels of trilinear single Higgs falls into the former description. Only the ggF process has one-loop diagram as LO, therefore only ggF process falls into the latter category. $\mathcal{M}^1_{\lambda_3}$ in Eq. 2.53 is defined as the λ_3-linearly-dependant contributions in $\mathcal{M}^1$. It can be obtained by the diagrams having one trilinear Higgs coupling in SM, which denoted as $\mathcal{M}^1_{\lambda_3^{\mathrm{SM}}}$, then rescaling them by κ_λ [14]. The particular gauge to consider the correct contributions for $\mathcal{M}^1_{\lambda_3^{\mathrm{SM}}}$ is unitary gauge.

The renormalization value $Z_H^{\rm BSM}$ in Eq. 2.52 can be written as Eq. 2.54 by re-summing only the *new physics* contributions at one loop, as described in [27].

$$\begin{aligned} Z_H^{\rm BSM} &= \frac{1}{1-(\kappa_3^2-1)\delta Z_H} \\ \delta Z_H &= -\frac{9}{16\sqrt{2}\pi^2}\left(\frac{2\pi}{3\sqrt{3}}-1\right) G_\mu m_H^2 \\ &= -1.536\times 10^{-3}. \end{aligned} \tag{2.54}$$

Note that when $\lambda_3 \longrightarrow \lambda_3^{SM}$, as κ_λ goes to 1.

In order to calculate the deviations of κ_λ from 1, one should be precise not only about the cross-sections, but also about the parameter C_1 , since it is the only parameter to be able to decide κ_λ.

One can extend the Eq.2.52 so that it includes the NLO EW contributions as well. The form of the equation becomes,

$$\Sigma_{\rm NLO}^{\rm BSM} = Z_{\rm NLO}^{\rm BSM}\left[\Sigma_{\rm LO}(1+\kappa_3 C1+\delta Z_H+\delta_{EW}\big|_{\lambda_3=0})\right] \tag{2.55}$$

where $\kappa_3=\kappa_\lambda$ and $\delta_{EW}\big|_{\lambda_3=0}$ is defined as;

$$\delta_{EW}\big|_{\lambda_3=0} \equiv K_{EW}-1-C_1-\delta Z_H \tag{2.56}$$

and K_{EW} is simply,

$$K_{EW} = \frac{\Sigma_{\rm NLO}^{\rm SM}}{\Sigma_{\rm LO}} \tag{2.57}$$

what $\Sigma_{\rm NLO}^{\rm SM}$ means here is Σ at LO + NLO EW order. Therefore, in the limit $\lambda_3 \longrightarrow 1$, $\Sigma_{\rm NLO}^{\rm BSM} \longrightarrow \Sigma_{\rm NLO}^{\rm SM}$.

2.3.1 Single Higgs Production Modes in pp Colliders

The Higgs production in p-p Colliders like LHC has different channels. These processes are given in decreasing order of the cross-sections [28]:

1. Gluon fusion (ggF)
2. Vector boson fusion (VBF)
3. Associated production with vector bosons (VH)
4. Production with top quark pair (ttH)
5. Production with single top quark and a jet (tHj)

In order to constrain Higgs self-coupling further, other than direct measurements via double Higgs production, one has to investigate it *indirectly* via single Higgs productions. The single Higgs production in hadron colliders can be examined in five different production modes. The production channels listed above are also the production channels for a single Higgs production.

2.3.1.1 ggF Mode

The gluon-gluon fusion to single Higgs process is the most dominant channel for single Higgs productions [29]. The LO Feynman diagram of ggF process is shown in Figure 2.4. Since the LO of the ggF process has one-loop, the NLO corrections come from two-loop. The method of calculation of C_1 requires the matrix elements of NLO contributions. This is not possible for the moment since there is no available machinery for the calculations Therefore, ggF processes is not included in this work.

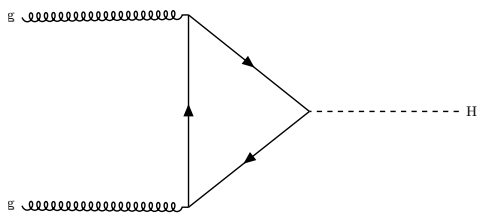

Figure 2.4: ggF Feynman diagram on tree level

2.3.1.2 VBF Mode

The vector-boson fusion processes can be described as Electroweak production of the Higgs boson with two jets. The VBF processes include the decays of vector bosons to two jets as well but these processes are studied separately as the associated production with vector bosons, or VH, processes described in the next section. The sample diagram of a LO VBF process can be seen in Figure 2.5.

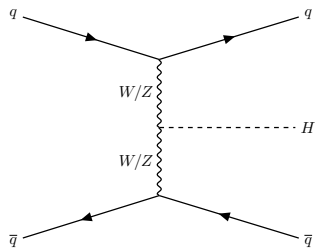

Figure 2.5: VBF Diagram on tree level

2.3.1.3 VH Mode

The VH channel consists of two distinct processes. One is ZH production and the other is WH production channels.

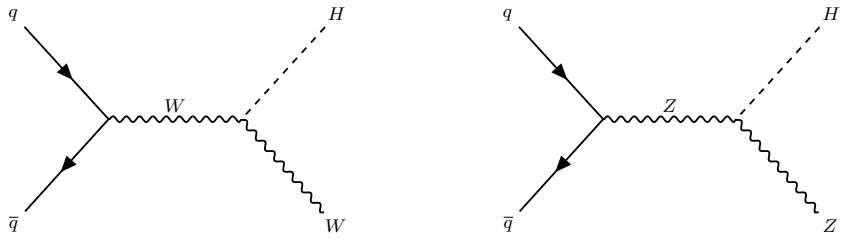

Figure 2.6: Tree-level Feynman diagrams of VH processes. HW on the left and HZ on the right.

What separates these processes from the VBF process is that vector bosons of VH processes do not decay into jets. Figure 2.6 shows the LO diagrams for WH and ZH

channels, respectively.

2.3.1.4 $t\bar{t}H$ Mode

This channel might be the most important production channel studied in this work. Although the cross-section of this channel is fairly low, its kinematic dependency is much higher in comparison with the other channels. Figure 2.7 shows the Feynman diagram of the channel on tree-level.

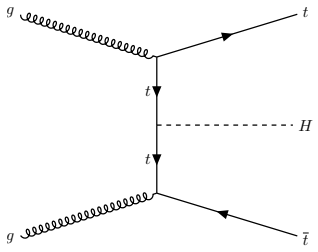

Figure 2.7: The Feynman diagram of $t\bar{t}H$ channel on tree-level

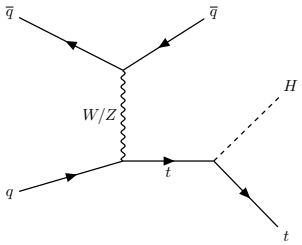

Figure 2.8: The tree-level Feynman diagram of tHj process

2.3.1.5 tHj Mode

The tHj channel differs from the ttH channel simply by the resultant quarks. Instead of a top quark pair, tHj processes have one top quark and one jet alongside Higgs boson. This cause some technical difficulties described in [27], as the calculation of tHj needs a careful and constant check on EW gauge invariance and UV finiteness.

CHAPTER 3

EXPERIMENTAL BACKGROUND

This chapter is about the experimental part of the Higgs particle. First, the Large Hadron Collider is introduced in Section 3.1. In this section, LHC experiments will be briefly discussed. In particular the CMS Experiment will be discussed in detail. After that, the experimental results on Higgs self coupling are given in Section 3.3. Both ATLAS and CMS results on the trilinear coupling are presented on both single and double Higgs production channels. Then the motivation for differential measurements of single Higgs coupling are discussed and the STXS bins are introduced.

3.1 Large Hadron Collider

The Large Hadron Collider is a hadron accelerator and collider with two separate vacuum rings, where the hadrons are accelerated and bent by a magnetic field around 8 T. The magnetic field is produced by superconducting electromagnets working at extremely low temperatures, around 2 K. Although the main purpose of the LHC is to investigate the EWSB and to discover the Higgs boson, which has already been achieved, it is motivated with BSM physics To archive its objectives, LHC consists of a few experiments dedicated for precision measurements and searching new sectors.

3.1.1 LHC Experiments

In order to have the general picture, short descriptions of the LHC experiments are given [30];

ATLAS[31]: The ATLAS experiment is one of the biggest experiments in LHC. It is

also one of the two general purpose detectors. Other than the Higgs investigations, extra dimensions and dark matter studies are also in the scope of ATLAS experiment.

CMS[32]: The Compact Muon Solenoid (CMS) is the other general-purpose detector in the LHC. Similar to the ATLAS experiment, the purpose of the CMS experiment goes beyond the Higgs studies. It involves BSM physics, extra dimensions and dark matter as well. CMS and ATLAS have the same scientific goals yet the design of the detectors differ highly from each other.

ALICE[33]: ALICE is dedicated to heavy-ion physics and designed to study strongly interacting matter. At high densities, they form what is called quark-gluon plasma. The studies are to understand and explain the color confinement phenomena in QCD and the problem called chiral-symmetry restoration.

LHCb[34]: LHCb detector is specially designed to study b-quark. It is designed to detect mostly the forward particles. By studying the b-quarks the LHCB experiment investigates CP violation and and the slight differences in matter and anti-matter.

TOTEM[35]: TOTEM experiment studies protons in the *forward* region. The detectors are situated about half a kilometer around the CMS detector. These detectors are designed to measure the particles emerged from the collisions at small angles.

LHCf[36]: The LHCf is an experiment having the purpose to study cosmic rays. The detectors are situated around the ATLAS detectors and designed to collect the forward particles, emerged from collisions at almost zero degrees. LHCf uses the data to simulate cosmic rays in laboratory conditions.

3.2 CMS Experiment

The CMS detector is a general-purpose detector operating at the LHC at CERN. The experiment successfully discovered the Higgs boson together with ATLAS. After Long Shutdown 2, Run 3 will start to search for BSM.

In the early design period, the detector requirements for CMS were established as follows[32];

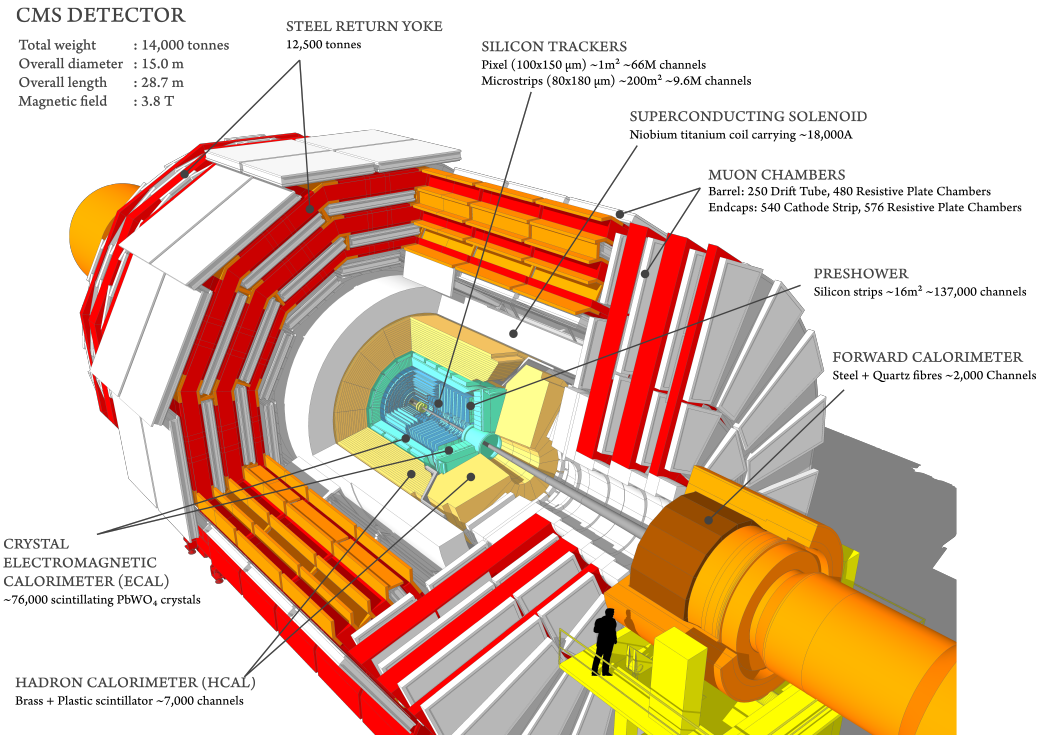

Figure 3.1: CMS Detector

- Good muon identification and momentum resolution over a wide range of momenta and angles, good dimuon mass resolution ($\approx 1\%$ at 100 GeV), and the ability to determine un-ambiguously the charge of muons with $p < 1$ TeV
- Good charged-particle momentum resolution and reconstruction efficiency in the inner tracker. Efficient triggering and offline tagging of τ's and b-jets, requiring pixel detectors close to the interaction region
- Good electromagnetic energy resolution, good diphoton and dielectron mass resolution ($\approx 1\%$ at 100 GeV), wide geometric coverage, π^0 rejection, and efficient photon and lepton isolation at high luminosities
- Good missing-transverse-energy and dijet-mass resolution, requiring hadron calorimeters with a large hermetic geometric coverage and with fine lateral segmentation.

The design of the detector fulfilled the requirements above. The main features of the detector are a high-field solenoid, a silicon based inner tracking system and a homogeneous scintillating-crystals-based electromagnetic calorimeter.

3.2.1 Coordinate System

The coordinate system chosen for CMS is a right-handed system and can be described as follows;

- The origin is the nominal collision point inside the detector
- The direction of the beam is z-direction
- The y-direction is vertically upwards
- The x-direction is radially towards the center of LHC
- The azimuthal angle is from x to y on x-y plane
- The polar angle is measured from z-axis

The pseudorapidity in this coordinate system can be defined as;

$$\eta = -ln(tan(\theta/2)) \tag{3.1}$$

Also, the transverse momentum, P_T and transverse energy, E_T are measured in x and y directions.

The coordinate system is shown in Fig.3.2.

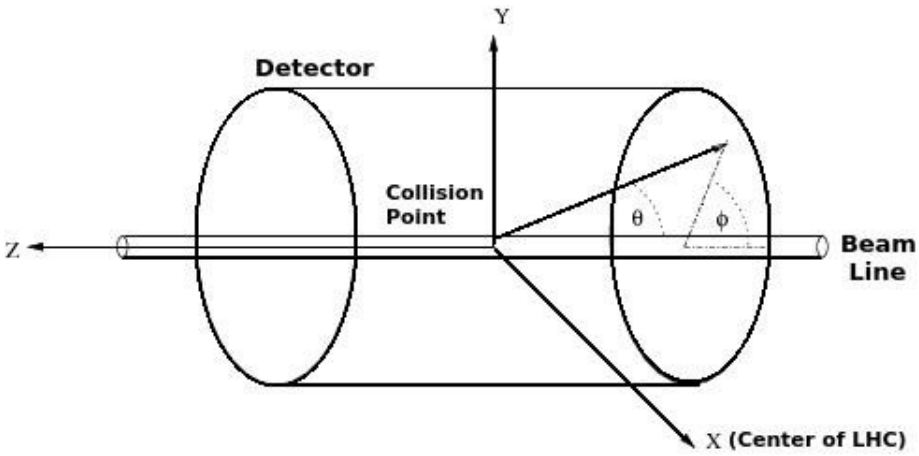

Figure 3.2: The coordinate system adopted for CMS

3.2.2 Superconducting Magnet

The Niobium-Titanium (NbTi) coil of the magnet carries 18000 A of current, and can generate a magnetic field of 4 T. The CMS coil has a very high stored energy over mass ratio (11.6 KJ/kg). A comparison of E/M value with several other detector magnets are shown in Fig.3.3. This is a very distinctive value and causes a great mechanical stress during powering. Therefore, most of the selenoid has a purpose of supporting the structure. What separates the superconducting solenoid of CMS from previous detector magnets are the following[32];

- Due to the number of ampere-turns required for generating a field of 4 T (41.7 MA-turn), the winding is composed of 4 layers
- The conductor, made from a Rutherford-type cable co-extruded with pure aluminium (the so-called insert), is mechanically reinforced with an aluminium alloy
- The dimensions of the solenoid are very large (6.3-m cold bore, 12.5-m length, 220-t mass)

Although, it has a large dimensions, it is rather thin ($\Delta R/R \approx 0.1$).

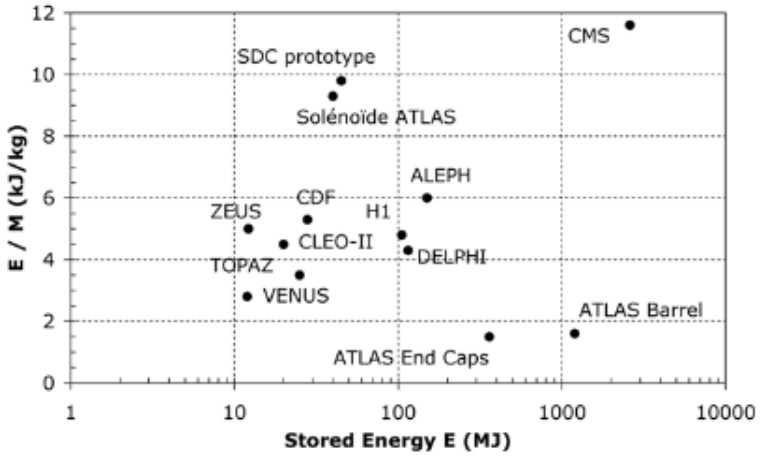

Figure 3.3: The energy/mass ratio of several detector magnets

The strong magnetic field produced by the solenoid bends the path of the charged particles inside tracker. The bent trajectory provides the necessary information to

calculate the momentum of the charged particles. The magnetic field is needed to be strong so that the path of the particles such as muons can be bent.

3.2.3 Inner Tracking System

The inner tracking system of CMS is designed to measure the trajectories of the charged particles emerging from the hadron collisions with high precision. The CMS solenoid provides a uniform magnetic field to the whole volume of the tracker. The tracker system is consists of a pixel detector and a silicon strip tracker. The system has an acceptance of pseudorapidity, $|\eta| < 2.5$.

A schematic representation of the CMS tracker is given in Fig.3.4. Each line corresponds to a detector module, while the double lines are back-to-back modules, delivering stereo hits.

A three layer hybrid pixel modules surround the interaction point and two disk modules are placed at the end of each side. The silicon strip tracker consists of three subsystems; the Tracker Inner Barrel and Disks (TIB/TID), surrounding the TIB, the Tracker Outer Barrel and covering the z-axis, Tracker End Caps at each side.

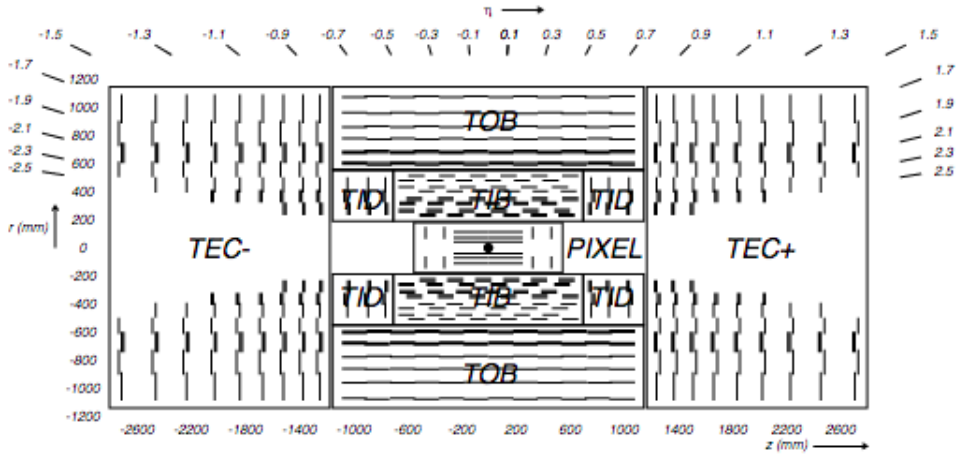

Figure 3.4: A schematic representation of the CMS tracker

3.2.3.1 Pixel Detector

The pixel detector is the closest detector to the collision point, consisting of 65 million pixels, about 8 cm far from the collision. This close range causes millions of particles through the detector. The rate is about 10 million particles per square centimeter per second. It is designed to be in use over ten-year duration of the experiment.

Each silicon sensor has dimensions of 100 μm by 150 μm so that similar resolution can be achieved in both $r - \phi$ and z directions.

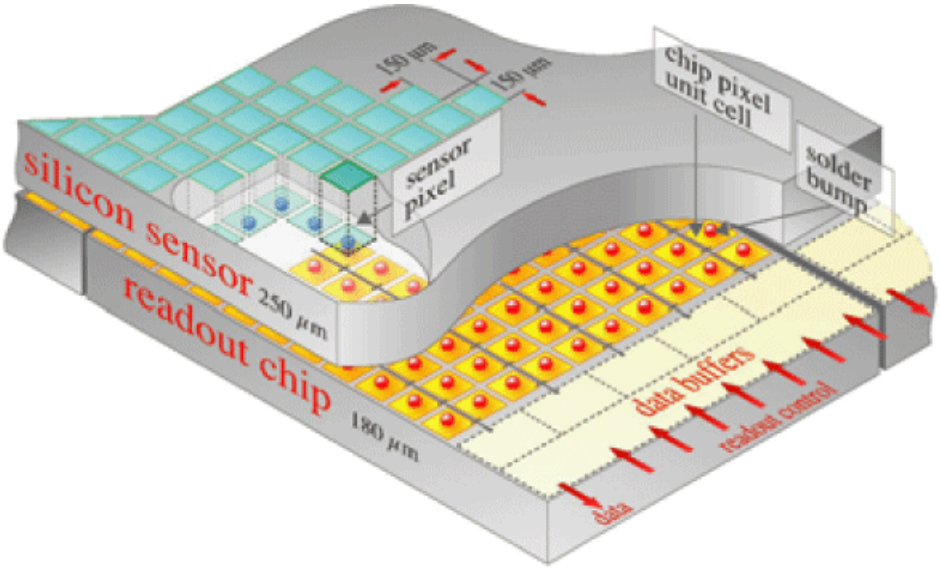

Figure 3.5: CMS Silicon Pixel Detector

Fig.3.6 shows the layout of the pixel detector and the hit coverage as a function of pseudorapidity. The 2 disk points are combined in the high η region.

3.2.3.2 Silicon Strip Detector

The silicon strip detector having an inner radius of 130 cm, comes after the pixel detectors. As shown in Fig.3.7, silicon strip detector consists of 4 inner barrel (TIB) layers and 6 outer barrel (TOB) layers. The outer layers are divided into two groups as 2 double-sided outer barrel layers and 4 single-sided outer barrel layers. Not shown in the figure, there are two end caps (TEC) close off the detector.

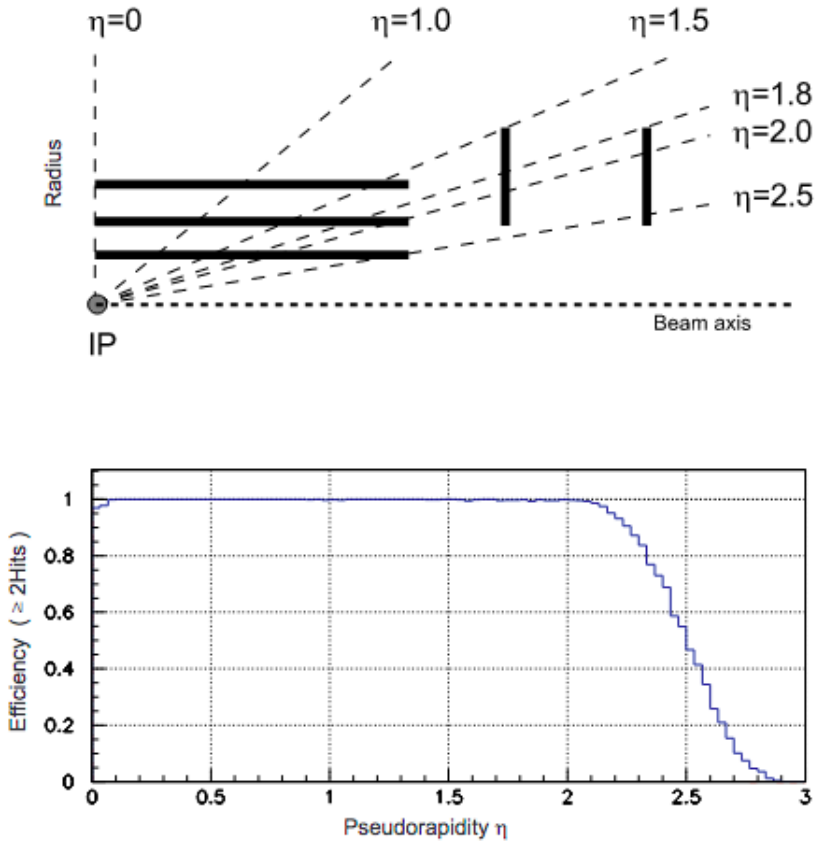

Figure 3.6: Geometric layout of the pixel detector and hit coverage as a function of pseudorapidity

The strip detector consists of 15200 high-sensitivity modules with a total of 10 million detector strips. In order to cover many regions, 15 different silicon sensor geometries are implemented. The sensors are designed to receive many particles in a small space since the fast response time and great spatial resolution they have. The basic working principle of the detectors are very similar to the pixel detector. When a charged particle passes through the detector, it interacts with electrons of the atoms of the detector material. This causes a small impulse inside the applied electric field, lasting a few nanoseconds. This signal is then amplified and stored.

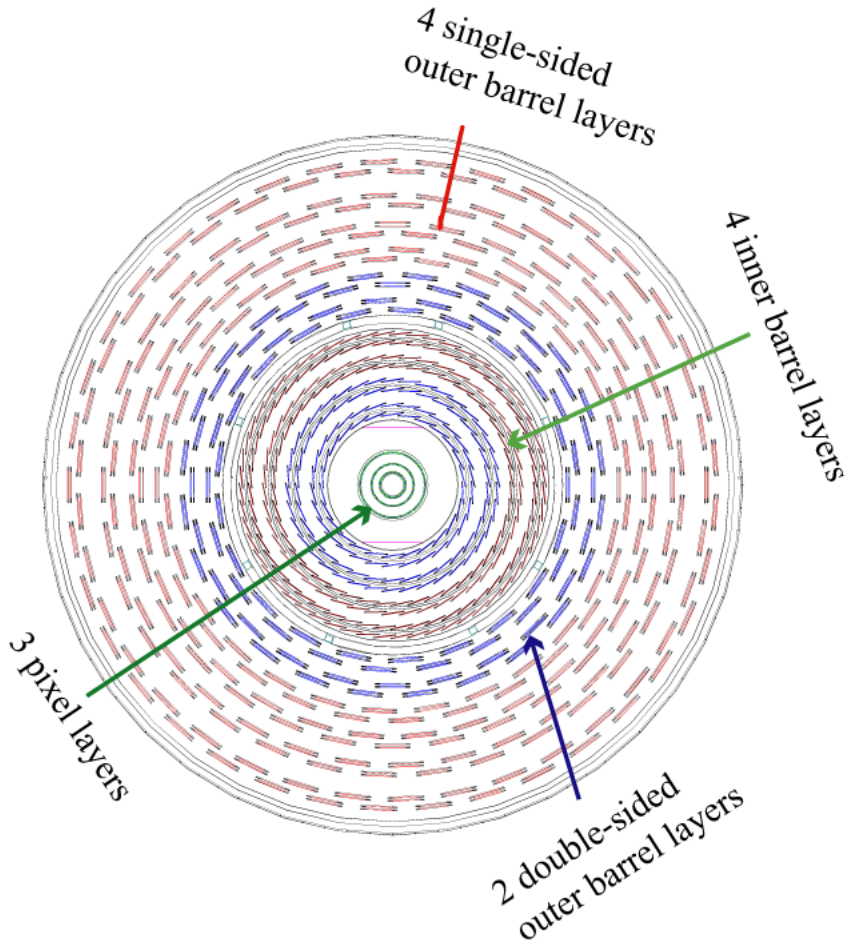

Figure 3.7: The tracker layers of the CMS

3.2.4 The Electromagnetic Calorimeter

The purpose of the Electromagnetic Calorimeter (ECAL) is to measure electron and photon energies. The necessity of high precision in a highly radiative conditions and 25 nanoseconds in between collisions are forced a particular material for the detector. Fulfilling the necessary requirements, lead-tungsten crystals ($PbWO_4$) was the appropriate choice. The central barrel of the ECAL has 61200 crystals while the end caps have 7324 crystals each.

Electrons and photons in the detector interacts with $PbWO_4$ crystals and cause excitation of atomic electrons. The de-excitatiıon of the atomic electrons gives photons that are detected by photo-detectors attached to crystals. This well-defined photons allow great precision.

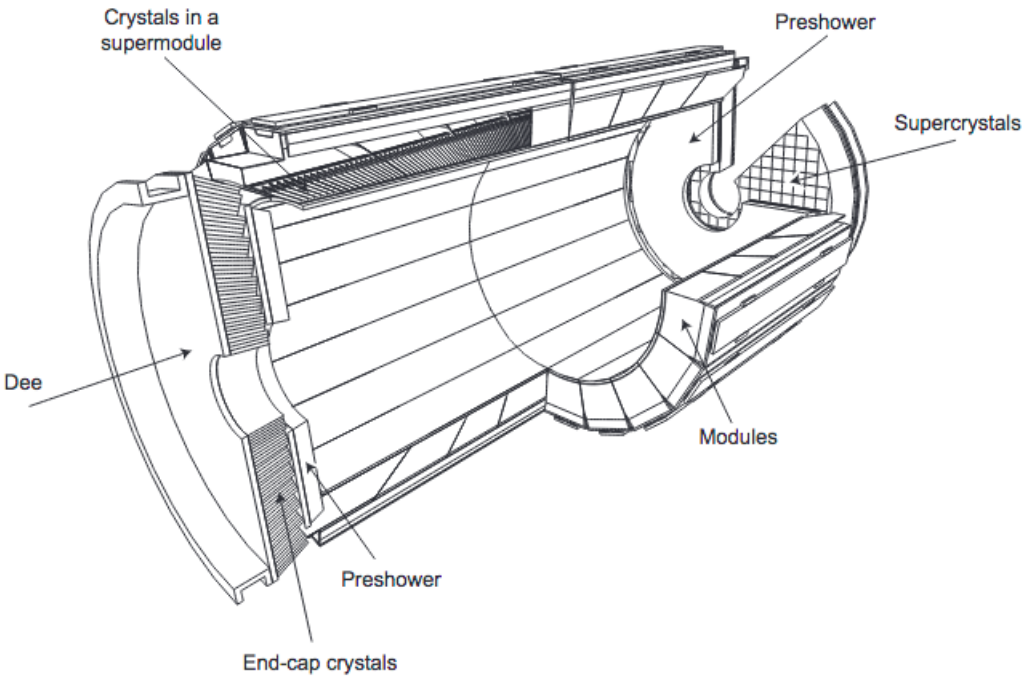

Figure 3.8: The layout of the CMS ECAL showing the module arrangements

ECAL has Preshower detectors in front of the end caps, providing extra spatial precision. They help to distinguish single high-energy photons and close pairs of low-energy photons

3.2.5 The Hadron Calorimeter

The Hadron Calorimeter (HCAL) is used for measuring the energy of hadrons and indirect detection of neutrino.

The HCAL aims to capture every particle emerging from the collisions. This way if we detect an imbalance in energy and momentum measured from the opposite sides of the detector, we can state that there are *invisible* particles produced. In order to guarantee these invisible particles are new particles, the HCAL is designed not to let any familiar particle go undetected.

HCAL is a sampling calorimeter, meaning it is made by alternating layers of dense absorber and plastic scintillator. Each time a hadron passes through an absorber, it may decay into secondary particles. Those particles can decay into other particles as

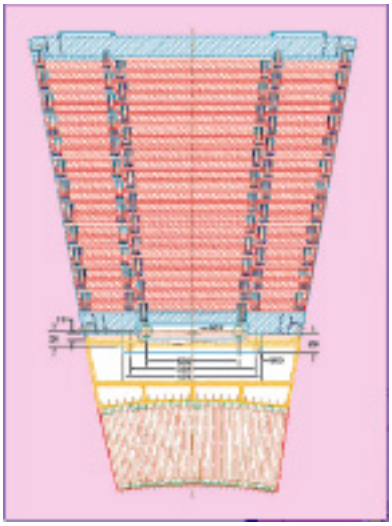

Figure 3.9: An HCAL module showing sampling layers

they interact with the following absorber. This causes a cascade of particles which is called a shower. Those particles cause the scintillating part to emit photons to be detected by Photo Multiplier Tubes. No photon can escape to other tile due to the design of the tiles. This is necessary to measure the energy of the particles passing through the tiles.

3.2.6 The Muon System

The defining goal of the CMS detector is to detect muons with high precision. The system has three functions, namely, muon identification, momentum measurement and triggering. The field created by the superconducting magnet and the magnet's flux-return yoke provides the great muon momentum resolution and trigger capability of the detector.

The reason that the muon chambers are the outer part of the detector is they are the only particles not stopped by the calorimeters. Also, they can penetrate several meters of iron without interacting with it. The muon path is measured by tracking its position through the multiple layers of the four muon stations in combination with the tracker data. This results in a great precision for the muon path. The momentum and energy of the muon is calculated by this data.

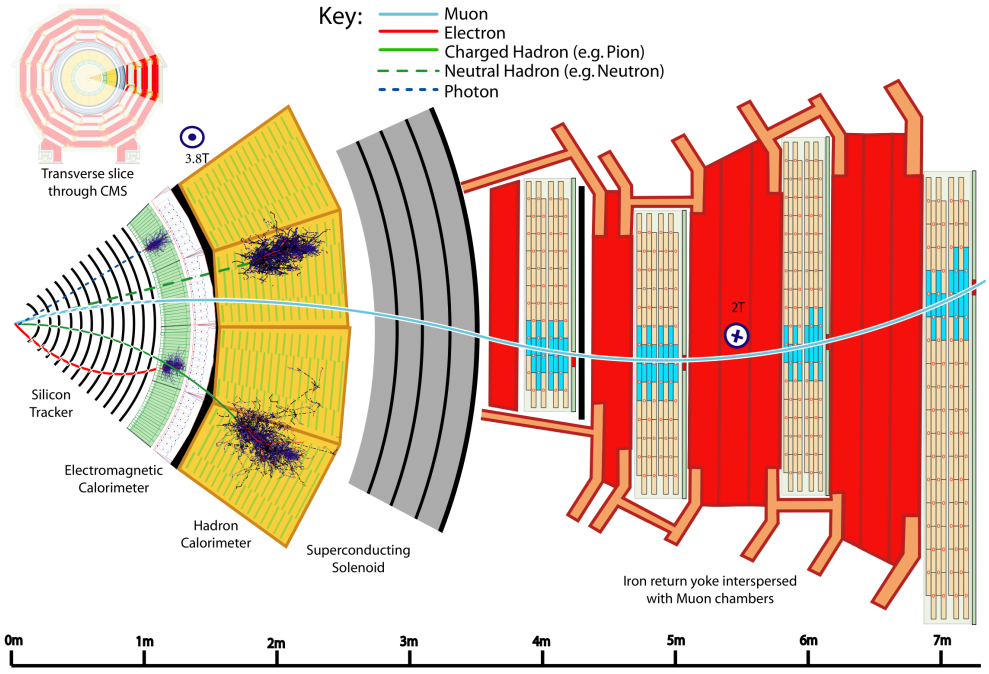

Figure 3.10: A transverse slice of the CMS detector

Fig.3.10 [37] is a sketch of some example of particle interactions in a transverse slice of the CMS detector, from the beam interaction region to the muon detector.

3.3 Experimental Background on Higgs Self Coupling Measurement

One of the important properties to be studied of the Higgs boson is its self coupling. If there are deviations from SM predictions, this might indicate that there are *new physics* effects in action. Therefore it is essential to study those couplings with higher precision. One of the expectations is that the so-called new physics effects can be found at the measurements of trilinear Higgs coupling. This investigation can be done in two ways; either via direct measurements through a double Higgs production or indirectly through a single Higgs production. Both channels are studied at LHC by ATLAS and CMS collaborations thoroughly.

The introduction of $\kappa_\lambda = \lambda_3/\lambda_3^{SM}$ helps the investigation of new physics elements. If κ_λ is differs from 1, which is the SM value, for a particular channel this could actually indicate the possibility of the new physics to be found through that produc-

tion channel, so it should be studied further. The importance of the parameter κ_λ is understandable, however, the measurements of it are not as precise as needed. This does not mean that we need more precision because we could not find any evidence of new physics. It means we do not have a precise value of κ_λ, or simply κ_λ is largely unconstrained. This is the main reason why both ATLAS and CMS collaborations are focusing on the trilinear Higgs coupling.

Both ATLAS and CMS Collaborations published combined measurements of Higgs boson at 7 and 8 TeV [38, 39] (Run 1), and at 13 TeV [40, 41] (Run 2). There is also a combination of the Run 1 results of CMS and ATLAS Collaborations at $\sqrt{s} = 7$ and 8 TeV [42].

The constraints on κ_λ from CMS double Higgs analysis at 36 fb^{-1} are given as; $-11.8 < \kappa_{\lambda_3} < 18.8$ at 95% C.L. [43]

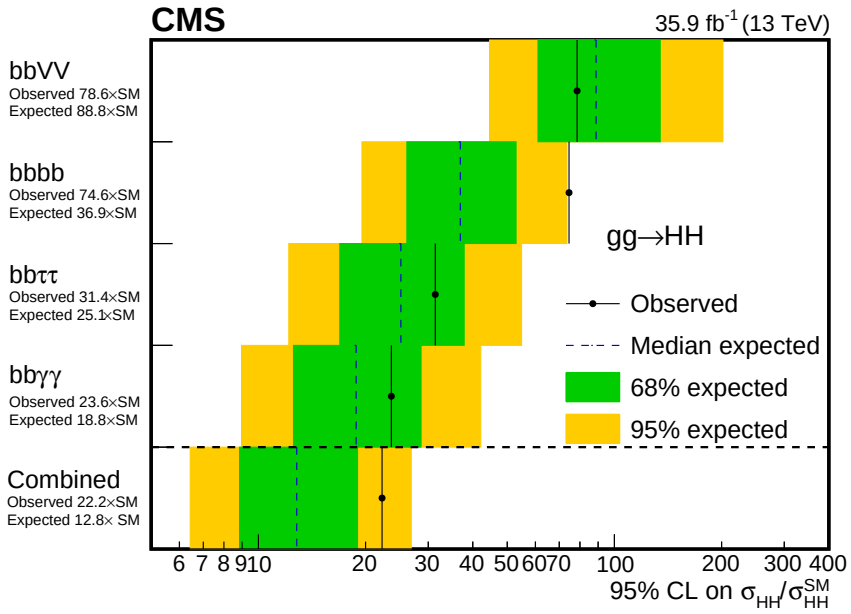

Figure 3.11: Double Higgs signal strength

CMS reported the observed and expected limits on nonresonant HH production signal strength are 22.2 and 12.8 times the SM expectations respectively[43]. The confidence level on the measurement is reported as 95%. The results for the individual channels and their combination are shown in Figure 3.11. The green and yellow bands in the figure corresponds to 68% and 95% C.L.intervals, respectively. In the

same study, the result for the κ_λ scan is also reported. The upper limits on the double Higgs production cross section as a function of κ_λ are shown in Figure 3.12.

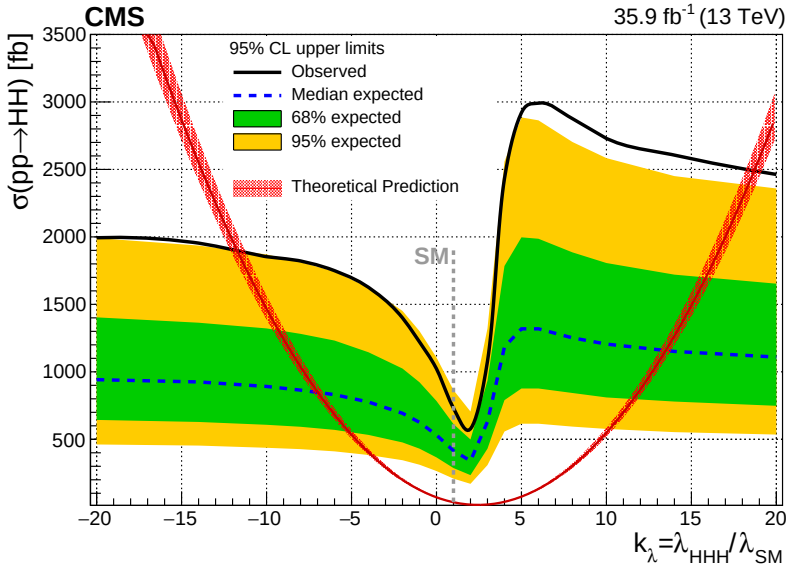

Figure 3.12: Result of κ_λ scan done for double Higgs production at CMS

For combined (single and double) Higgs boson production, CMS only considered inclusive measurements so far. The results are reported in [44]. This study will contribute to the differential measurements of the trilinear Higgs self coupling at CMS.

The constraint on κ_λ from ATLAS Double Higgs at 36 fb^{-1} are given as;
$-5.0 < \kappa_{\lambda_3} < 12.0$ at 95% C.L. [45]

The ATLAS studies [46] shows the expected change in cross-section a and branching ratio b of several production and decay channels with respect to κ_λ.

The ATLAS collaboration had considered the STXS bins described in Section 3.4.1 also for the differential measurements. The results of those studies can be found in Table 3.1.

In [14], they put constraints on κ_λ by using the ggF and VBF data in [42] as a reference, and by assuming a χ^2 distribution (Fig.3.14), they reported;

$$\kappa_\lambda^{best} = -0.24,\ \kappa_\lambda^{1\sigma} = [-5.6, 11.2],\ \kappa_\lambda^{2\sigma} = [-9.4, 17.0] \tag{3.2}$$

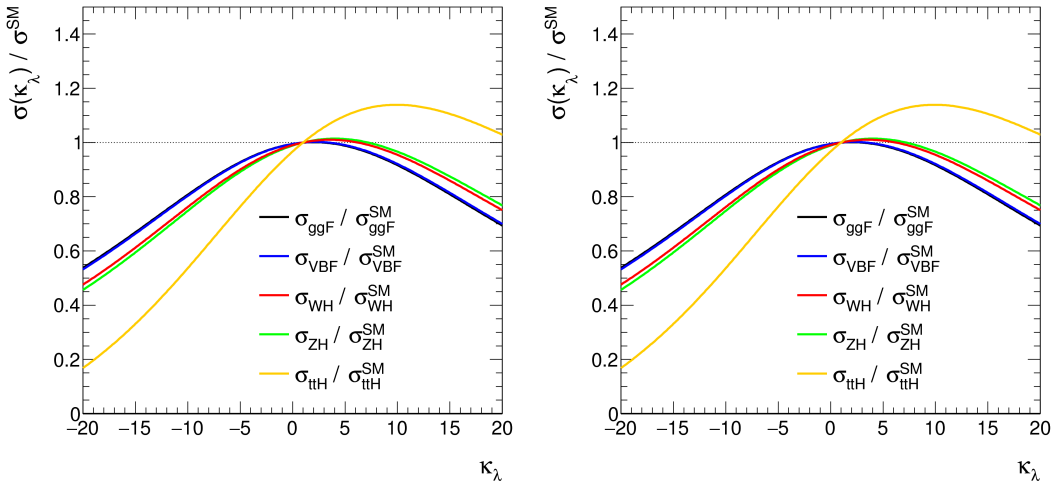

(a) (b)

Figure 3.13: Variation in cross-sections (right) and branching ratios (left) of single Higgs decay channels with respect to κ_λ

where κ_λ^{best} is the best value, $\kappa_\lambda^{1\sigma}$ and $\kappa_\lambda^{2\sigma}$ are the 1σ and 2σ intervals, respectively. In Fig.3.14, the left panel, Fig.a shows χ^2 as a function of κ_λ for various distributions. The left panel, Fig.b, shows the p-value as a function of κ_λ.

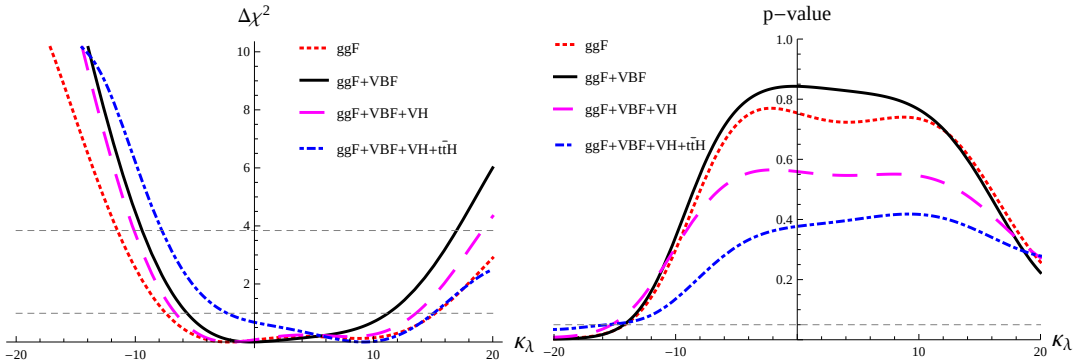

(a) (b)

Figure 3.14: χ^2 (right) and p-value (left) as functions of κ_λ

Also, the same procedure is applied on "CMS-II" (300 fb^{-1}) and "CMS-HL-II" (3000

fb^{-1}) cases and resulted in;

$$\kappa_\lambda^{1\sigma} = [-1.8, 7.3],\ \kappa_\lambda^{2\sigma} = [-3.5, 9.6],\ \kappa_\lambda^{p>0.05} = [-6.7, 13.8] \tag{3.3}$$

for the "CMS-II" case. "CMS-HL-II" case yielded the following result;

$$\kappa_\lambda^{1\sigma} = [-0.7, 4.2],\ \kappa_\lambda^{2\sigma} = [-2.0, 6.8],\ \kappa_\lambda^{p>0.05} = [-4.1, 9.8] \tag{3.4}$$

Figure 3.15 shows the χ^2 (Fig.a) and p-value (Fig.b) as a function of κ_λ for various distributions.

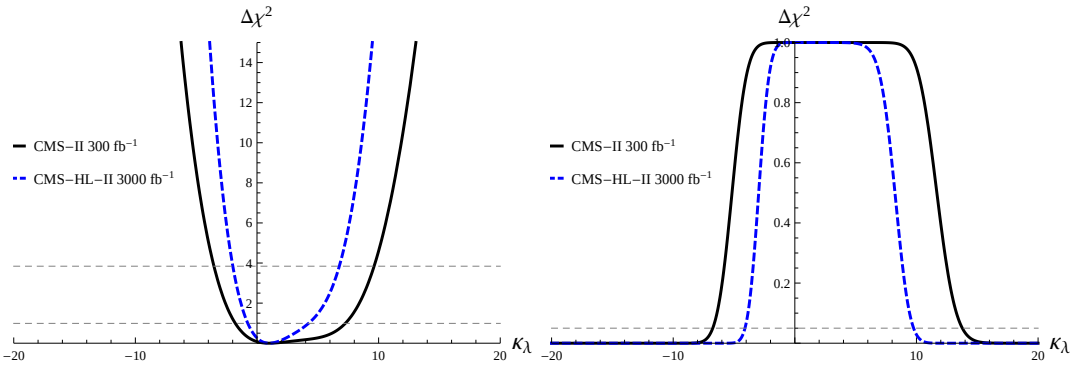

(a) (b)

Figure 3.15: χ^2 (right) and p-value (left) as functions of κ_λ for CMS-II and CMS-HL-II

In addition to these results, by assuming a relative uncertainty of 0.01, the reported result for ggF, VBF, VH and ttH case is,

$$\kappa_\lambda^{1\sigma} = [0.86, 1.14],\ \kappa_\lambda^{2\sigma} = [0.74, 1.28],\ \kappa_\lambda^{p>0.05} = [0.28, 1.80] \tag{3.5}$$

Figure 3.16 shows the χ^2 (Fig.a) and the p-value (Fig.b) as a function of κ_λ for various distributions with the assumption of 1% relative uncertainty.

Another study done to constraint κ_λ through a global fit is done in [47]. At the 1σ

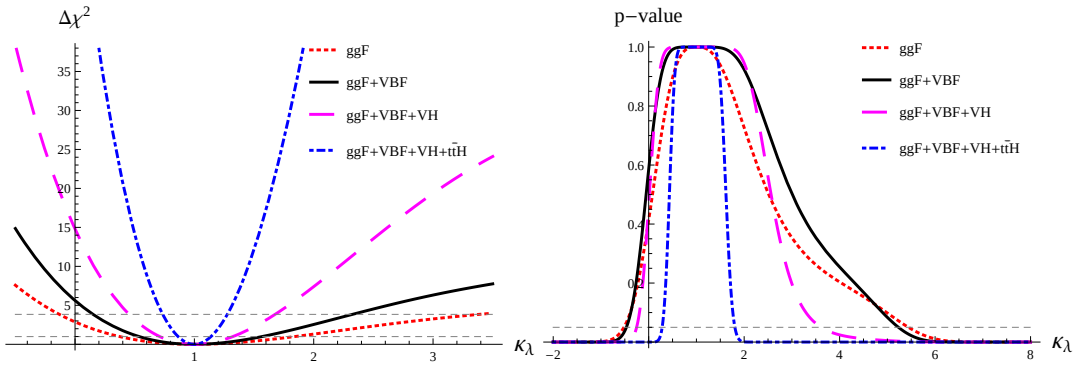

(a) (b)

Figure 3.16: χ^2 (right) and p-value (left) as functions of κ_λ with a relative uncertainty of 0.01

level, the interval for κ_λ is given as;

$$\kappa_\lambda \in [-1.1, 4.7] \tag{3.6}$$

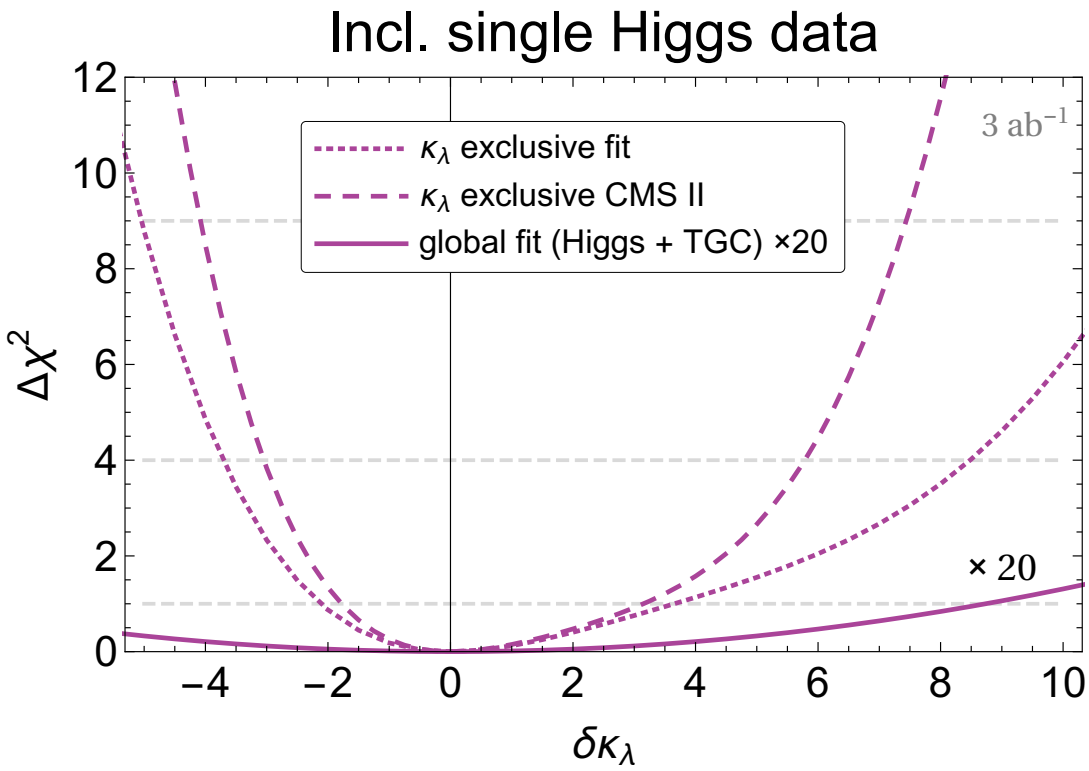

Figure 3.17: χ^2 as a function of κ_λ obtained by a global fit

Figure 3.17 shows the result obtained by the applied global fit including the constraints from the EW boson trilinear gauge couplings (TGC) and the bounds on the $h \longrightarrow Z\gamma$ decay (solid line). It can be seen easily that the the κ_λ is virtually unconstrained.

A similar study done in [47] for combined (single and double) Higgs production removes the flatness of the curve, as in Figure 3.18. The intervals for the coupling are given as;

$$\begin{aligned} &\kappa_\lambda \in [0.0, 2.5] \cup [4.9, 7.4] \text{ at } 68\% \text{ C.L.} \\ &\kappa_\lambda \in [-0.8, 8.5] \text{ at } 95\% \text{ C.L.} \end{aligned} \tag{3.7}$$

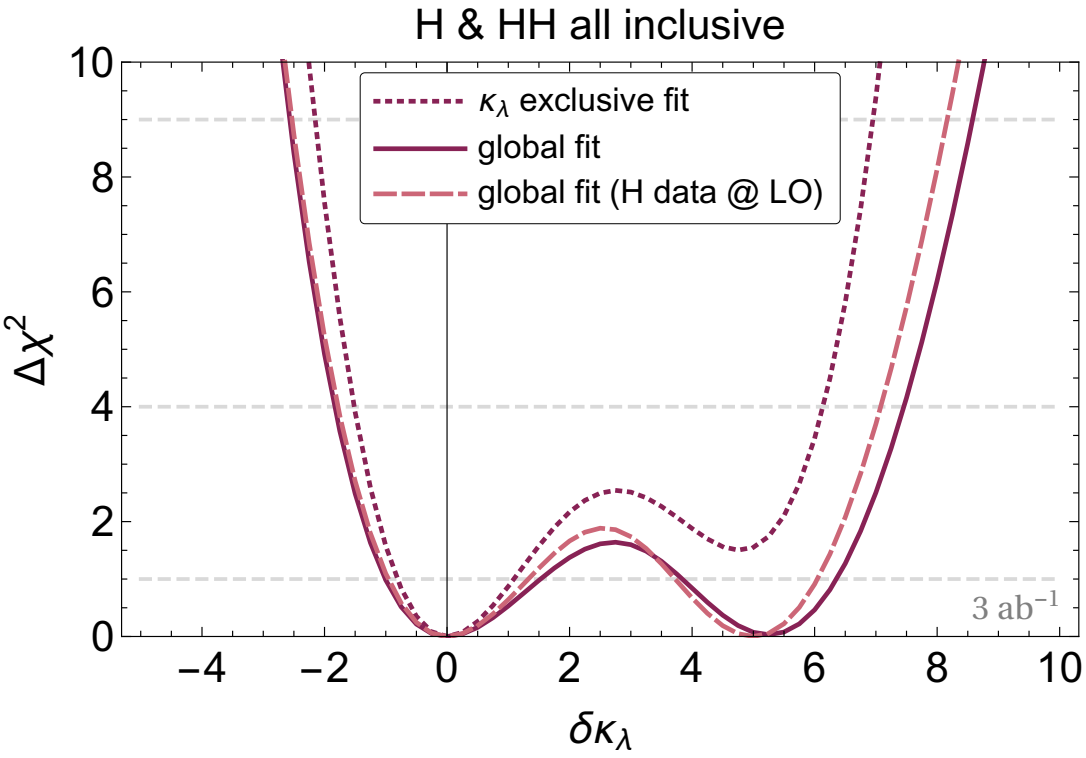

Figure 3.18: χ^2 as a function of κ_λ from a global fit performed on both single and double Higgs on inclusive level

In [47], the differential information on Higgs pair production is also considered. Figure 3.19 shows the χ^2 as a function of κ_λ with the inclusion of the differential information.

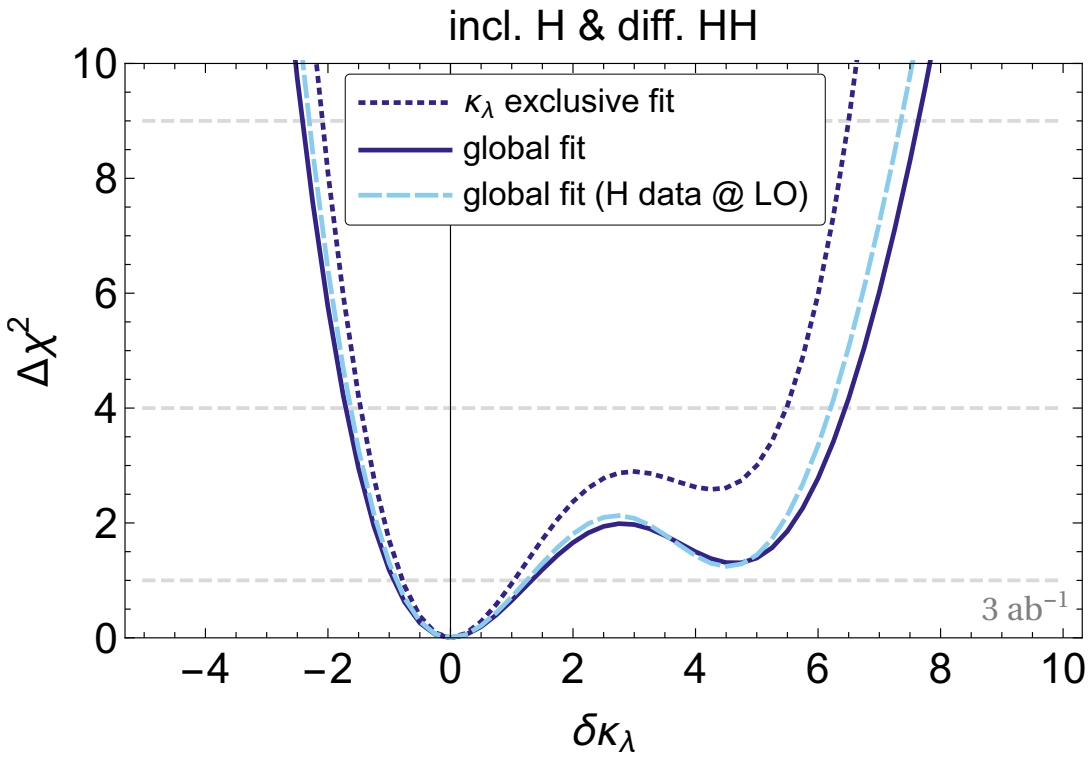

Figure 3.19: χ^2 as a function of κ_λ with the fits involving inclusive single Higgs and differential double Higgs

The 1σ and 2σ intervals for κ_λ are further reduced and became;

$$\begin{aligned} \kappa_\lambda &\in [0.1, 2.3] \text{ at } 68\% \text{ C.L.} \\ \kappa_\lambda &\in [-0.7, 7.5] \text{ at } 95\% \text{ C.L.} \end{aligned} \tag{3.8}$$

These results suggest;

1. The combined measurements of both single and double Higgs constrain the trilinear coupling better than the separate ones

2. The differential measurements could yield better constraints on trilinear Higgs coupling than the inclusive measurements

Following the conclusions made above, we shall look into the motivation for differential measurements of trilinear Higgs coupling in the following section.

3.4 Motivation for Differential Measurements of Trilinear Higgs Coupling

The motivation of the measurements of trilinear Higgs coupling is discussed in the previous sections. It is obvious that more precision is needed for the coupling measurements. The differential measurements provides that even without new measurements, *i.e.* with the existing data. Since the parameter C_1 has a kinematic and process dependence, investigating this parameter in different kinematic regions may provide a better precision than the inclusive measurements. Therefore, κ_λ might be measured more precisely. Indeed, the results provided by the ATLAS collaboration at Table 3.1 shows that the differential measurements put better constraints on κ_λ.

Table 3.1 shows that the expected limit for κ_λ is narrower in differential measurements rather than in inclusive calculations. The results are obtained by the ATLAS group and the table is taken from [46].

POIs	Granularity	${\kappa_F}^{+1\sigma}_{-1\sigma}$	${\kappa_V}^{+1\sigma}_{-1\sigma}$	${\kappa_\lambda}^{+1\sigma}_{-1\sigma}$	$\kappa_\lambda[95\%C.L.]$
κ_λ	STXS	1	1	$4.0^{+4.3}_{-4.1}$	[-3.2, 11.9]
				$1.0^{+8.8}_{-4.4}$	[-6.2, 14.4]
κ_λ	Inclusive	1	1	$4.6^{+4.3}_{-4.2}$	[-2.9, 12.5]
				$1.0^{+9.5}_{-4.3}$	[-6.1, 15.0]

Table 3.1: ATLAS differential results for κ_λ

Other than the ATLAS and CMS studies, the differential study on single Higgs and double Higgs on differential level reduced the κ_λ intervals even further in [47], comparing with the inclusive results they reported in the same study as they discussed in previous section.

Figure 3.20 shows the χ^2 as functions of κ_λ for both differential measurement on single Higgs (Fig.a) and the combined differential measurements (Fig.b).

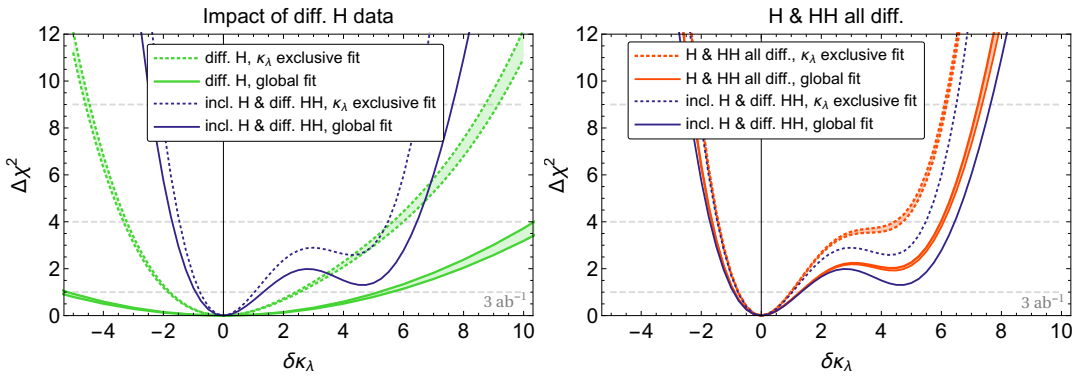

(a) (b)

Figure 3.20: χ^2 as functions of κ_λ for single Higgs differential measurements (right) and combined differential measurements (left)

3.4.1 STXS Bins

Simplified Template Cross Sections (STXS) are introduced in order to provide a natural way to evolve the coupling measurements in the future. The basic idea behind the STXS bins is to have a compromise between direct measurements and fiducial measurements. The direct measurements have maximum sensitivity but also highly theory dependence. Fiducial measurements on the other hand have the most model and theory independence however less sensitivity. The goal of STXS framework is to maximize the sensitivity of the measurements while minimizing their theory dependent.

STXS bins proposes measuring the cross sections in different regions of phase space. This regions are defined for different masses or different number of jets for each process.

3.4.1.1 Bin definitions

The bin definitions are motivated by minimizing theory dependence and maximizing experimental sensitivity. Also, possible BSM effects are aimed to be isolated. The bins are defined specifically for different production modes. The bins used in this study are revised from the original Stage 1.1 to Stage 1.2 with certain modifica-

tions. The associated production with a single quark channel (tHj) is not considered in STXS bin definitions. In this study, the bins for ttH is also used for tHj.

In Figure 3.21 the process is defined as a usual gluon fusion production including the EW corrections to $gg \longrightarrow H$. As mentioned in previous sections, the differential calculations for ggH requires the EW corrections as suggested in the STXS bins defined for ggF. However, there is no method for this calculation for the present.

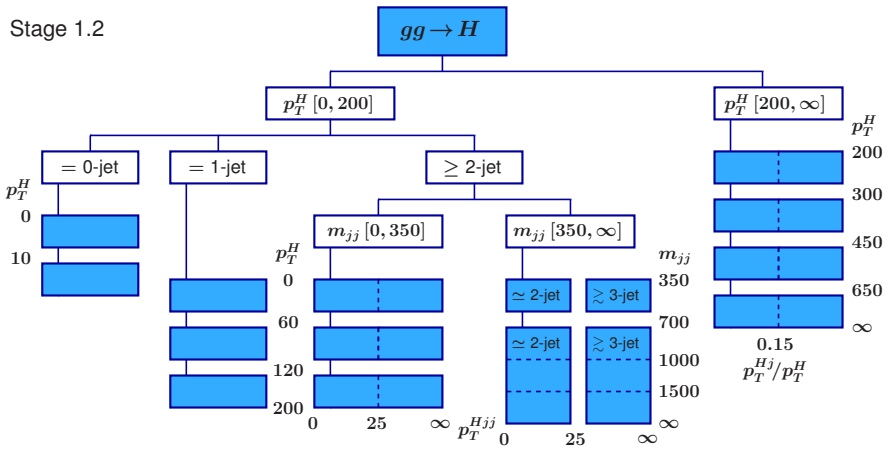

Figure 3.21: STXS bins for gluon-gluon fusion production channel of the Higgs boson

Figure 3.22 shows the binning of $t\bar{t}H$ production channel. The bins for $t\bar{t}H$ channel are defined only for the different phase space regions. The reason for that there are no additional jets to be considered here. Therefore, there is no need for dividing the bins according to the jet pair mass or the number of jets.

The bins for VBF is shown in Figure 3.23. There are two different *categories* for the bins of VBF channel. Both the jet pair mass and transverse momentum are considered for the binning.

The bins for the VH channel is defined for all the different processes of VH channel. In this study, only $q\bar{q} \longrightarrow WH$ and $q\bar{q} \longrightarrow ZH$ processes are considered. $gg \longrightarrow ZH$ process is not studied because of the need of EW two-loop corrections, which cannot be calculated as explained before.

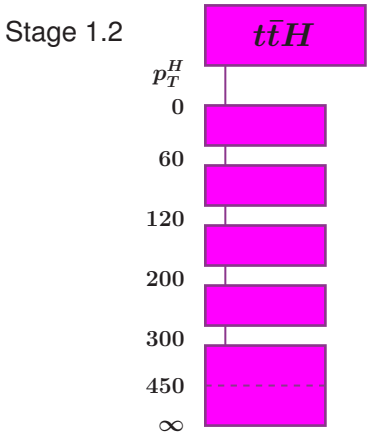

Figure 3.22: STXS bins for $t\bar{t}H$ production channel of the Higgs boson

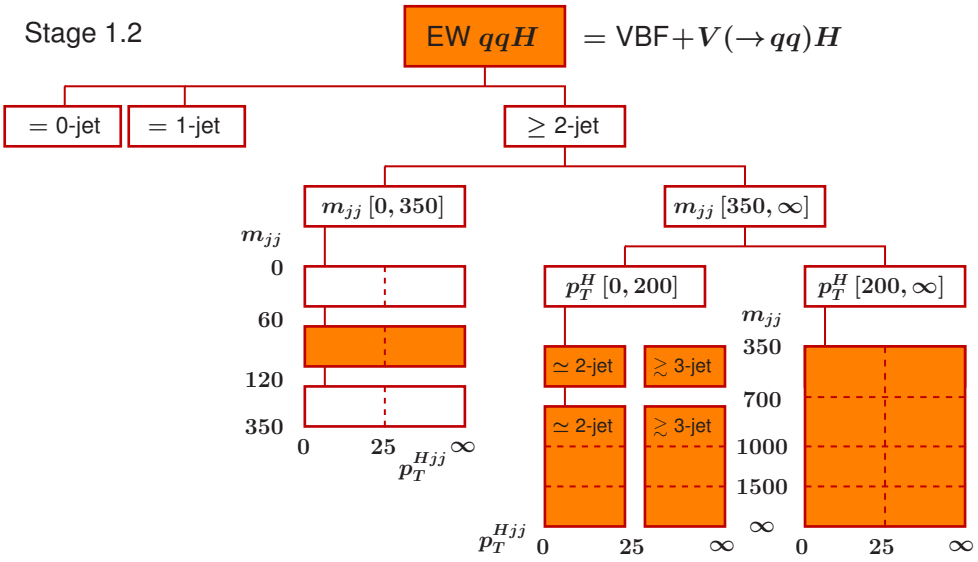

Figure 3.23: STXS bins for the vector-boson fusion production channel of the Higgs boson

3.5 The Impact of the Calculation

The Figure 3.25 shows this work in the big picture. The κ_λ scan is done through the proper analysis of CMS data by the use of Higgs combine tools. In this work, the existing framework for calculating C_1 is automatised to calculate it in STXS bins. Then κ_λ scan in STXS bins is done by the use of Higgs Combine Tools in STXS bins.

The combination of double and single Higgs production analysis, as expected, yields

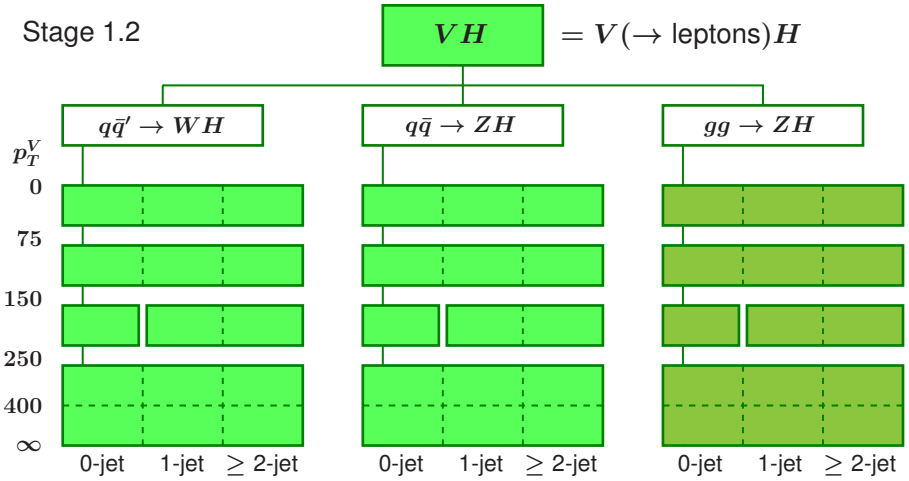

Figure 3.24: STXS bins for the associated vector-boson production channel of the Higgs boson

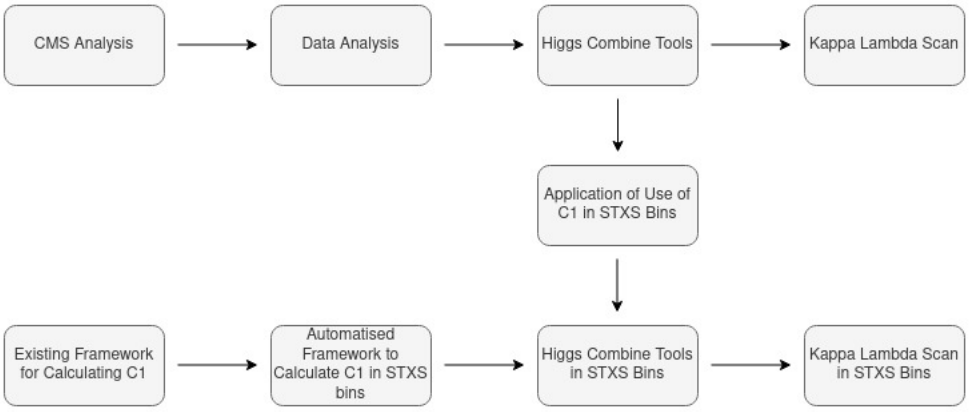

Figure 3.25: The flowchart showing the steps of κ_λ scan.

better constraints on κ_λ .

The standard procedure of κ_λ scan is described simply at the upper raw of Figure 3.25. The similar steps will be carried out in order to do κ_λ scan in STXS bins. Our contribution is automatizing the framework in STXS bins so that the C_1 calculations can be done with ease and high accuracy for each bin.

The precise and accurate calculation of C_1 contributes to a κ_λ value with narrower constraints. It can be seen easily from Eq.2.52 that given the cross-sections or decay widths of a process, the remaining free parameter is C_1. Therefore, more precise and accurate C_1 leads to a more precise and accurate κ_λ .

CHAPTER 4

CALCULATION METHOD

This chapter is dedicated to the framework established for the calculation of C_1 parameter and its automatizing. The core program used in our calculations is MADGRAPH5_AMC@NLO which is comprised of MADGRAPH and MC@NLO . A new code is written to calculate the C_1 parameter in STXS bins. This calculation is automatized for the use of the CMS collaboration. After that the Trilinear-RW package is explained. This package is written specifically to calculate C_1. Then the installation of all the necessary programs and packages will be explained. Finally the method of automatizing the framework to calculate C_1 in STXS bins will be discussed.

4.1 MadGraph 5

MADGRAPH/MADEVENT [48, 49, 50] is a general purpose matrix element generator alike to COMPHEP/CALCHEP [51, 52, 53], SHERPA [54] and WHIZARD [55]. MADGRAPH 5 [56] is the latest version of MADGRAPH. MADGRAPH5 is written in Python language, while the previous versions are written in Fortran 77. This results in faster run of the code with new algorithms and fewer restrictions.

Since MADGRAPH5 is and open source program, it can provide collaborative development. One important feature of the MADGRAPH5 is that it might generate any tree-level matrix elements for a given Lagrangian. It does not matter whether the Lagrangian is a renormalizable or an effective Lagrangian. This is provided via the FEYNRULES [57], a MATHEMATICA [58] based package. Other than the calculation of matrix elements from the Lagrangian itself, FEYNRULES provides a common

syntax for model creation. This is important since all the matrix element generators mentioned uses their own syntax. This way, it is simpler to implement a new model for the simulations. Also, the need to modify the generator code for a new model implementation become redundant with FEYNRULES, thus the models can be used for any matrix element generator. The common model format which is integrated with FEYNRULES is called UFO [59] or The Universal FEYNRULES Output. It is a standardized model format that makes FEYNRULES to communicate with any matrix element generator so that the output can be used in any of the generators.

4.2 MC@NLO

MC@NLO [60] is a method developed to automatize the calculation of QCD NLO contributions to the scattering processes so that the cross-sections and final state distributions can be calculated reliably. There are several methods discussed regarding the problem, *i.e* combining tree level matrix elements with hard jets production from parton showers. In order to achieve the desired solutions, there are two main methods; one is the subtraction method and the other is phase-space slicing method.

The slicing method is a simple enough method seemingly complete to match the parton shower calculations and NLO computations. However, in order to apply the method to achieve its goal, a slicing parameter has to be introduced. The problem is that the slicing parameter should go to zero but in practice it cannot be too small. Therefore, it only has been used to produce phenomenological results.

The subtraction methods considered prion to the introduction of MC@NLO mainly considered to match the NLO matrix element calculations to next-to-leading logarithmic parton showers. However, there was no algorithms for that when MC@NLO is introduced.

MC@NLO is a method based on the subtraction method for matching the matrix elements of NLO and the parton showers. It is an automatized framework providing a smooth transition from soft-emission regions to hard-emission regions.

4.3 MadGraph5_aMC@NLO

MADGRAPH5_AMC@NLO [61], in simple terms, is the combination of both MADGRAPH and MC@NLO . Therefore, it replaces them both and should be used instead of them. It is written to calculate the cross-sections and decays of LO and NLO QCD processes. Although these calculations might be made separately for each process, there was no particular need for high precision automatized framework. However, the progress in LHC resulted in need for high precision calculations. One reason is the events with large transverse momentum tails, turns out, not as rare, even though the probabilities are low. The other is simply the BSM phenomenology. The present precision is not enough to make any distinction between SM and BSM signals. Even though there is no general method for calculating an arbitrarily high order, it is possible to have a generalized method if we consider up to NLO contributions. MADGRAPH5_AMC@NLO as introduced in [61] provides such a method for calculating LO and NLO QCD calculations for any arbitrary observable and any arbitrary process. In addition to that, MADGRAPH5_AMC@NLO is also capable of doing the *same* calculations for LO and NLO Electroweak processes [62].

4.4 Trilinear-RW

The methods for calculating trilinear Higgs coupling from measurements of a single Higgs process are discussed thoroughly in [14]. Therefore, two packages working on MADGRAPH5_AMC@NLO are introduced in [27], namely, Trilinear-FF and Trilinear-RW. Both are MADGRAPH5_AMC@NLO modules, for calculating trilinear Higgs self-coupling including the one-loop contributions. The package files are public and can be found on MADGRAPH WIKI FOR HIGGS SELF COUPLING website [1]. However, the calculation methods are completely different.

In Trilinear-FF, the one-loop corrections are parameterized as form factors which are functions of external momenta. Then the form factors used as effective vertices in a UFO model written for that purpose. Then this UFO model is used in MADGRAPH5_AMC@NLO. In [27], this method is applied for only VBF and VH pro-

[1] https://cp3.irmp.ucl.ac.be/projects/madgraph/wiki/HiggsSelfCoupling#no1

duction channels.

Trilinear-RW implements a totally different method to calculate C_1. It creates a sample of LO unweighted events. Then, the events are used as an input to compute the weights. Finally, the generated LO events are reweighted by their corresponding weights calculated in the previous step. It is noted that this method is faster and more efficient than Trilinear-FF. Therefore, C_1 value is calculated for ttH and tHj channels as well as VBF and VH channels by using this method.

The framework established in [27] is used for the calculation of C_1 on inclusive level and results for differential distributions are provided. However, the package does not include the calculations of C_1 values for specific differential bins. Therefore, one must add necessary cuts to achieve C_1 values on any kinematic region. The method applied to do that is explained in Section 4.5

4.5 Automatizing the calculation of C_1 in STXS bins

The necessity for automatizing of the calculation of C_1 was always there since running the package is not that straightforward. It can be seen easily from the description in Appendix B that in order to run the package several steps should be followed. This allows a lot of room for mistakes. Therefore automatized calculation is the way to go.

It might seem tedious at first but it is way more tedious than the initial thought. There are several reasons for that. First of all, for each run, one needs to be careful about the process running and the labeling of the output at the first step. The other reason is regarding a specific process, $t\bar{t}H$, since its loop diagram generation code is different than the one in the example. One challenge might also be to remember to change the number of events for each time running it. The last one is to set the scaling factors. Although they are arbitrary and their effects are minimal to the result, the accepted framework describes them as the average of the sum of the masses of resulting particles. The suggested scale factors in [63] is also $\mu_R = \mu_f = \Sigma m_i/2$ which provides a more stable perturbative expansions at both fixed order and the resummed level.

One of our main contributions to this package is to be able to apply cuts for trans-

verse momentum, P_T, for certain particles in the processes. This is not a feature of Trilinear-RW package but in order to calculate C_1 in STXS bins, it is needed. Without automatizing the package, one should also be careful about the lower and upper bounds of P_T.

The script for automatization takes lower and upper bounds of P_T and number of events, calculates C_1 in selected bins. So far, each process has its own script. Further step is to combine all scripts into one so that it takes the process as an input as well. This way, to run the package and calculate C_1 for desired processes becomes as easy as writing a one line of command with 4 inputs. For the moment, the command

Example:

```
./autorun_HW_wcut.sh 300 500 500000
```

In the example given above, the automatized script autorun_HW_wcut.sh takes 3 values as inputs and gives C_1 as the output. The output is written in a text file called result_hw_300_500. The 3 inputs are lower P_T bound, upper P_T bound and the number of events, respectively. This means that when the script is run, the C_1 value of P_T interval of 300 and 500 [MeV] is calculated for 500k events.

The installation and set-up of the automatized script is given in Appendix B.

CHAPTER 5

RESULTS AND DISCUSSION

5.1 Proof of Concept

We have constructed the same framework in [27] to calculate C_1 values.

The comparison of the results are given below. The histograms shows the number of events with respect to the transverse momentum. There are slight deviations in VBF and tHj channels that are addressed below.

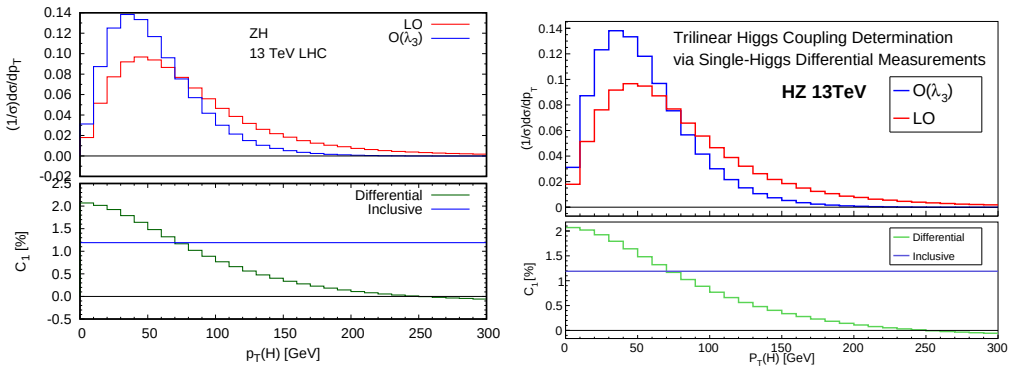

Figure 5.1: ZH channel results from the established framework (left) and our framework (right)

There are two problems that should be addressed in our framework. First one is that the VBF process has around 1% deviation from the result in [27]. The reason for that it is not possible to apply any cut to the jet pair invariant mass. This was necessary to filter the diagrams with VH processes in it, such as in the Figure 5.6. The most likely solution is to apply parton shower. However, due to the mismatch of the versions of MADGRAPH5_AMC@NLO , PYTHIA8 and the Trilinear-RW package, it is not possible to do the analysis with parton shower.

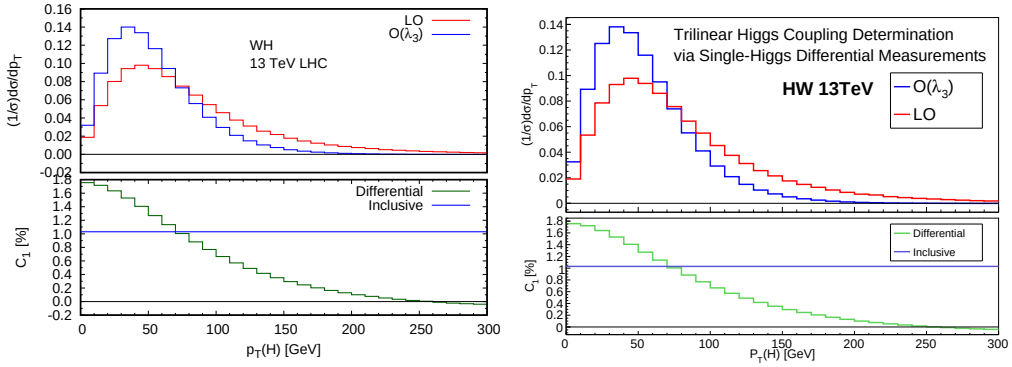

Figure 5.2: WH channel results from the established framework (left) and our framework (right)

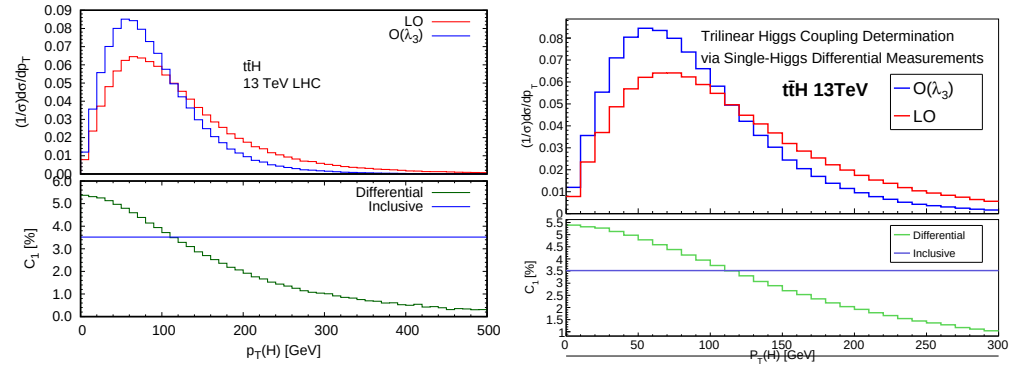

Figure 5.3: $t\bar{t}H$ channel results from the established framework (left) and our framework (right)

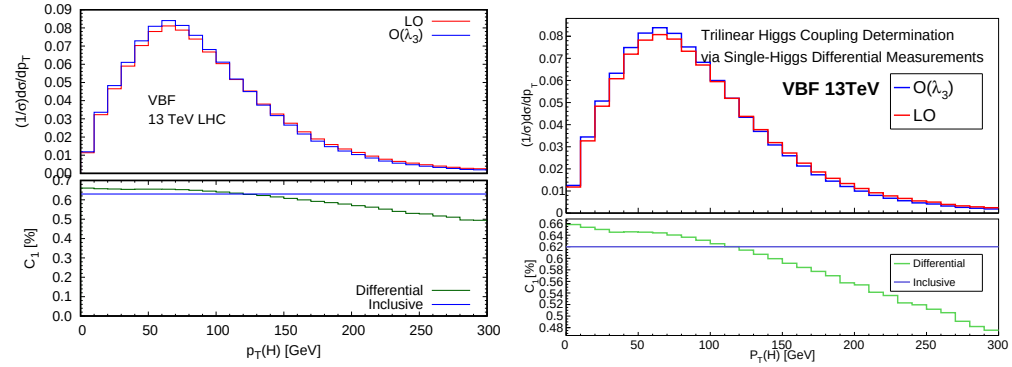

Figure 5.4: VBF channel results from the established framework (left) and our framework (right)

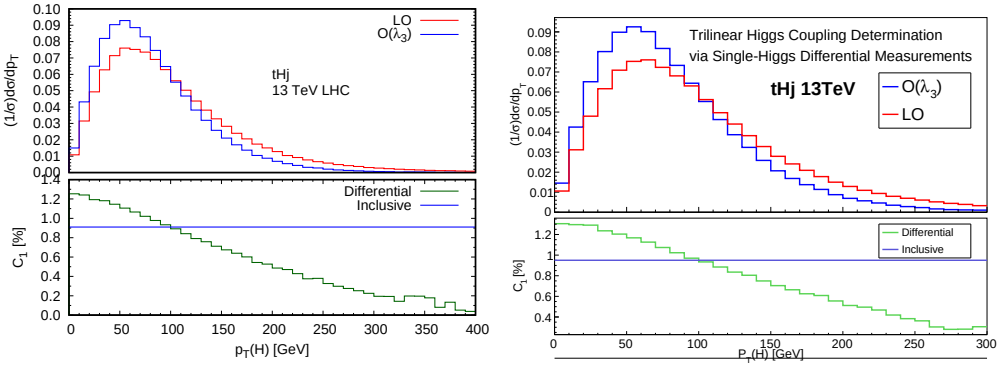

Figure 5.5: tHj channel results from the established framework (left) and our framework (right)

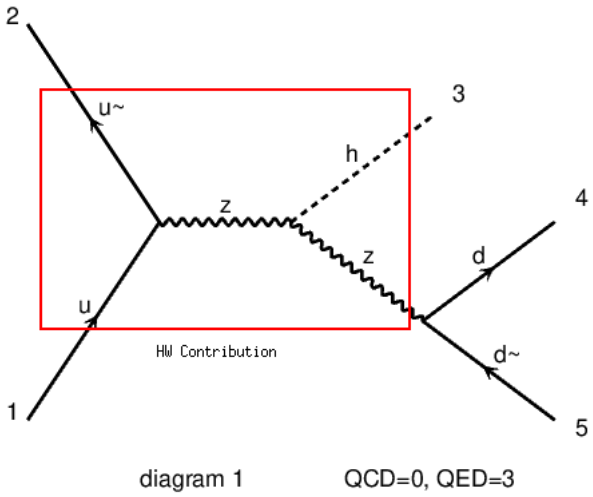

Figure 5.6: This diagram is an example of an unwanted diagram for VBF calculations.

The second one is about the tHj process. We have 4% deviation from the paper results. This should be studied further to identify the problem. There were no cuts specified for this process. The same possible solution of parton shower is applicable for tHj channel as well.

Although there are deviations in two processes, the rest of the production channels work properly and the results obtained from differential calculations of those channels are consistent with the predictions.

5.2 Comparison of the results of inclusive calculations

As it can be seen in Table 5.1, the inclusive calculations of C_1 values for VH processes match exactly with the reference paper as well as the C_1 value for $t\bar{t}H$ process. There is a slight difference in VBF process and somewhat more difference in tHj process.

Channels	VBF	ZH	WH	$t\bar{t}H$	tHj
$C_1(\%)$ Paper	0.63	1.19	1.03	3.52	0.91
$C_1(\%)$ Ours	0.62	1.19	1.03	3.52	0.95

Table 5.1: Comparison of C_1 values with the paper

The general form of the command used to calculate C_1 is the following;

./<script_name>.sh <lower bin border> <upper bin border> <number of events>

These results are obtained using 500k MC events. So far, each process has its own script. The following command gives the results in Table 5.1;

./autorun_<process>_<cut>.sh 0 -1 500000

Setting upper bin border to -1 means that there is no upper bin border, so the above command calculates C_1 inclusively.

5.3 Differential results

The C_1 results obtained from the application of the method described in the previous section are given below for every single Higgs production channel.

5.3.1 VH

The differential calculations for C_1 could not be done in the given STXS bins. The bins for $P_T(V) > 150\ GeV$ had to be merged since C_1 was calculated to be negative in those bins, which is not physical. The results for ZH and WH are given in Tables 5.2 and 5.3 respectively. Note that this is not caused by any error on the construction of

the framework. Comparing the histograms in [27], one can notice the same *problem* exists there too.

$P_T(Z)[GeV]$	0-75	75-150	>150
$C_1(\%)$	1.64	0.80	0.14

Table 5.2: C_1 results in STXS bins for HZ

$P_T(W)[GeV]$	0-75	75-150	>150
$C_1(\%)$	1.41	0.69	0.12

Table 5.3: C_1 results in STXS bins for HW

5.3.2 VBF

Differential calculations for VBF channels in STXS bins requires cuts on the jet pair mass. This cannot be achieved at the moment. It will be added. Note that, because of the 1% deviation, the results of differential calculations would not be accurate. This problems will be solved together by applying cuts on the jet pair mass.

5.3.3 $t\bar{t}H$

The $t\bar{(}t)H$ channel on inclusive level match perfectly with the already established and accepted framework. Therefore, the differential results given in Table 5.4 is the correct values of C_1 in STXS bins. It is seen that the kinematic dependence of C_1 in the $t\bar{(}t)H$ process is the highest among all single Higgs production channels.

$P_T(H)[GeV]$	0-60	60-120	120-200	200-300	300-450	>450
$C_1(\%)$	5.06	4.08	2.75	1.52	0.72	0.22

Table 5.4: C_1 results in STXS bins for $t\bar{t}H$

5.3.4 tHj

The STXS bins for tHj channel is chosen to be the same bins as in $t\bar{(}t)H$ channel. Note that this results are not accurate. The reason for that is our inclusive calculations of C_1 has 4% deviation from the correct value. Therefore, the results presented in the Table 5.5 are not correct values. This should be solved by applying a parton shower model.

$P_T(H)[GeV]$	0-60	60-120	120-200	200-300	300-450	>450
$C_1(\%)$	1.23	1.01	0.72	0.42	0.18	0.02

Table 5.5: C_1 results in STXS bins for tHj

5.4 Current Status of Calculating C_1 in STXS Bins on CMS

In [64], the current status on the study of the single Higgs modelling for constraining the trilinear Higgs coupling in STXS bins is published. Although it is a draft, not a finalized version, the initial results are given in Tables 5.6, 5.7 and 5.8. The bins used for the calculations are given in Figures 3.22, 3.24 and 3.23.

For the $t\bar{t}H$ channel, C_1 results are given in Table 5.6. The statistical uncertainties and the uncertainties from the scale and PDF variations are also reported. *Note* that the C_1 and the uncertainties are scaled by 10^2.

STXS Bin	C_1	σ(stat.)	σ(scale + pdf)
TTH_FWDH	3.33 ± 0.04	0.03	0.02
TTH_PTH_0_60	5.15 ± 0.04	0.01	0.04
TTH_PTH_60_120	4.23 ± 0.03	0.007	0.02
TTH_PTH_120_200	2.92 ± 0.01	0.006	0.01
TTH_PTH_200_300	1.688 ± 0.006	0.006	0.002
TTH_PTH_GT300	0.703 ± 0.005	0.005	0.002

Table 5.6: $t\bar{t}H$ results in STXS bins (Stage1.2)

This channel highly sensitive to the κ_λ especially in low P_T. This sensitivity can be realized in Figure 5.7.

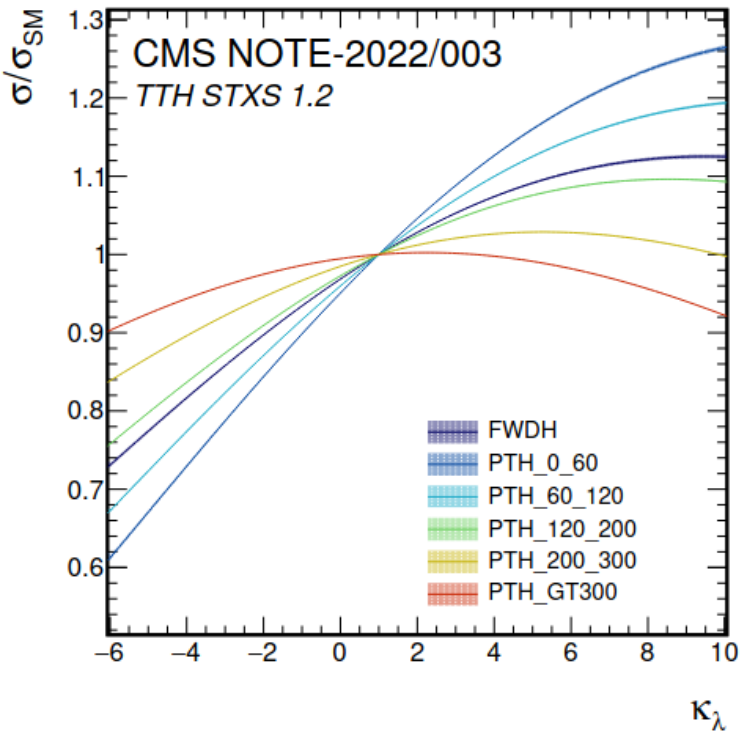

Figure 5.7: The variations in $t\bar{(}t)H$ cross-section as a function of κ_λ

For the VH channel, two cases are considered. One is the ZH channel where Z decays into two leptons ($Z \longrightarrow ll$) and the other is the WH channel with W decaying into a lepton and its neutrino ($W \longrightarrow l\nu$). The former denoted as Z(ll)H and the letter as W(lν)H. The results of C_1 and corresponding uncertainties are reported in Table 5.7.

The change in the cross-sections with respect to κ_λ is given for both Z(ll)H () and W(lν)H (a) channels. The Figure 5.8 shows the sensitivity in κ_λ when the calculations done in STXS bins.

The VBF channel results in STXS bins, including V(qq)H process, are given in Table 5.8. The process is binned with respect to the number of jets, invariant of the jet pairs, and transverse momentum of the Higgs boson.

It can be seen easily form the Figure 5.9 that the channel is not particularly sensitive to κ_λ for different kinematic regions.

STXS Bin	C_1	σ(stat.)	σ(scale + pdf)
QQ2HLL_FWDH	1.350 ± 0.009	0.004	0.008
QQ2HLL_PTV_0_75	1.632 ± 0.005	0.002	0.004
QQ2HLL_PTV_75_150	0.870 ± 0.005	0.002	0.005
QQ2HLL_PTV_150_250_0j	0.209 ± 0.002	0.001	0.001
QQ2HLL_PTV_150_250_GE1j	0.395 ± 0.007	0.002	0.006
QQ2HLL_PTV_GT250	0.000 ± 0.004	0.0009	0.003
QQ2HLNU_FWDH	1.175 ± 0.008	0.004	0.008
QQ2HLNU_PTV_0_75	1.399 ± 0.004	0.002	0.003
QQ2HLNU_PTV_75_150	0.747 ± 0.004	0.001	0.004
QQ2HLNU_PTV_150_250_0j	0.186 ± 0.002	0.0009	0.001
QQ2HLNU_PTV_150_250_GE1j	0.331 ± 0.005	0.002	0.005
QQ2HLNU_PTV_GT250	0.002 ± 0.003	0.0007	0.003

Table 5.7: Z(ll)H (upper half) and W(lν)H results in STXS bins (Stage1.2)

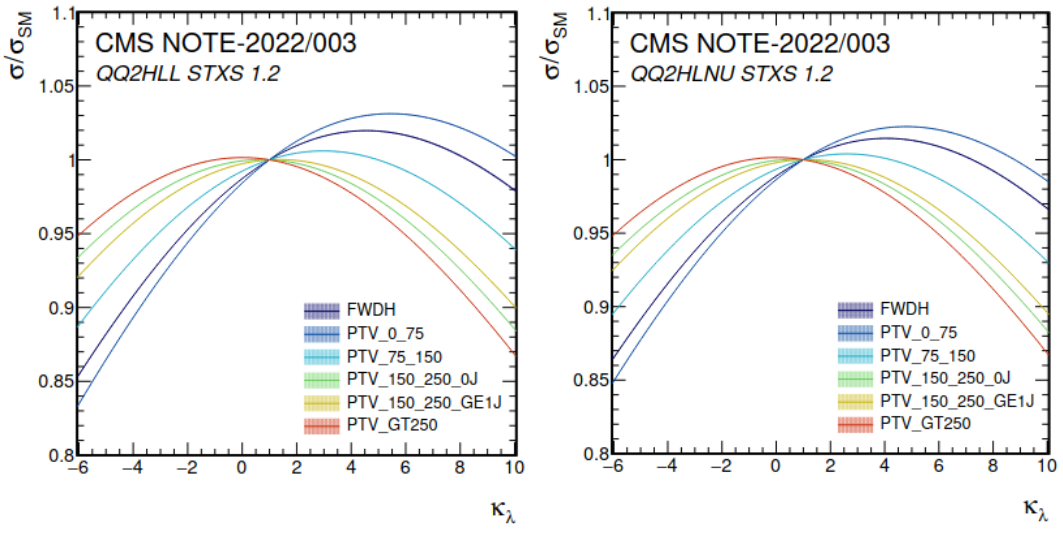

(a) Z(ll)H

(b) W(lν)H

Figure 5.8: Variations in ZH (left) and WH (right) cross-sections as functions of κ_λ

QQ2HQQ STXS Bin	C_1	σ(stat.)	σ(scale + pdf)
FWDH	0.84 ± 0.01	0.02	0.01
0J	0.896 ± 0.009	0.002	0.009
1J	0.777 ± 0.008	0.0008	0.008
GE2J_MJJ_0_60	0.747 ± 0.009	0.004	0.009
GE2J_MJJ_60_120	0.83 ± 0.01	0.002	0.01
GE2J_MJJ_120_350_0j	0.692 ± 0.005	0.001	0.005
GE2J_MJJ_GT350_PTH_GT200	0.508 ± 0.002	0.002	0.0006
GE2J_MJJ_350_700_PTH_0_200_PTHJJ_0_25	0.625 ± 0.001	0.001	0.0007
GE2J_MJJ_350_700_PTH_0_200_PTHJJ_GT25	0.611 ± 0.003	0.002	0.002
GE2J_MJJ_GT700_PTH_0_200_PTHJJ_0_25	0.622 ± 0.001	0.001	0.0003
GE2J_MJJ_GT700_PTH_0_200_PTHJJ_GT25	0.594 ± 0.002	0.001	0.0006

Table 5.8: VBF results in STXS bins (Stage1.2)

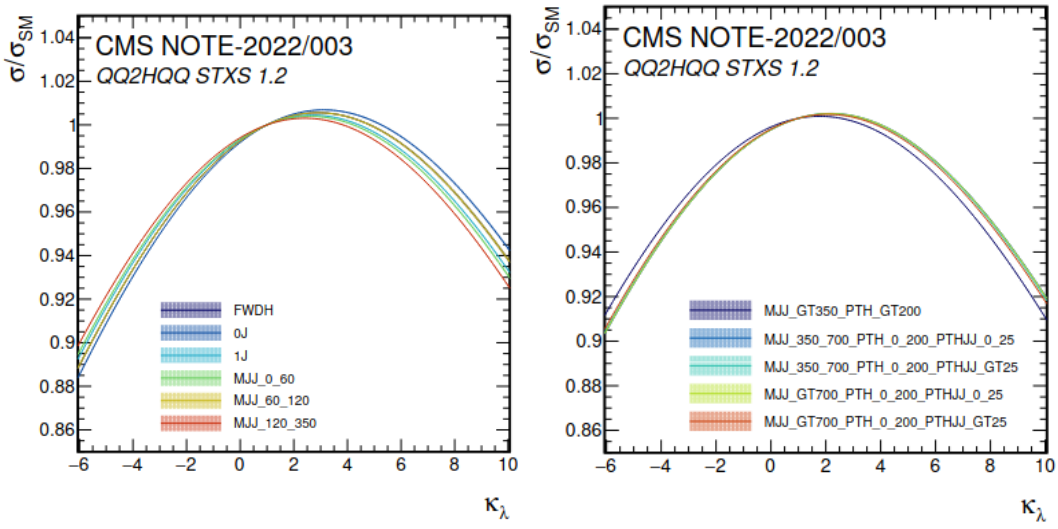

(a) $0 < m_{jj} < 350$

(b) $m_{jj} > 350$

Figure 5.9: Variations in VBF cross-section as functions of κ_λ for m_{jj} less than 350 Mev (left) and greater than 350 MeV (left)

CHAPTER 6

CONCLUSION

After the discovery of the Higgs boson, the experimental searches have been focused on the measurement of its properties. One of the properties of the Higgs boson is the trilinear coupling. It is the coupling of three Higgs particles. This coupling value, unlike the other coupling values of Higgs, is virtually unconstrained. Therefore, there is a need to put further constraints on trilinear Higgs coupling.

The motivation of calculating C_1 comes from the need of constraining the trilinear Higgs coupling further. The precise measurements of the coupling λ_3 is greatly needed. The reason for that is any deviations in λ_3 from the SM value indicates BSM physics. The theoretical framework we have exploits the fact that the C_1 has kinematic and process dependence. Therefore the precise measurements of the C_1 parameter, one is able to measure the trilinear Higgs coupling more precisely as well.

We have constructed a working framework to calculate C_1 values in STXS bins for the production channels of single Higgs except ggF channel. The reason of this exception is the non-existance of technical feasibility for calculating two loop diagrams. Our calculations show slight deviations for VBF and tHj processes when it is compared with the results in [27]. This should be studied further to improve the framework. The rest of the production channels are in very good agreement with the results in [27].

The status of the work at particular times was presented to Higgs Combination Group [18], to the CMS France [19] and to the CMS Lyon Group [20]. There were positive reactions and a high interest to the presented work.

The VBF and tHj channel calculations should be improved in order to match with the results in [27]. After this is done the framework can completely be used in order

to constrain κ_λ further. Our framework will be provided to the Higgs Combination Group in order for them to combine single and double Higgs contributions to put further constraints on κ_λ. The prepared framework might also be used with slight modifications. An example is the possible preparation of the two loop calculation methods. After the necessary tools are provided, ggF processes can be calculated in STXS bins as well. This is possible since the framework allows new integration when the necessary method prepared.

REFERENCES

[1] Serguei Chatrchyan et al. Observation of a New Boson at a Mass of 125 GeV with the CMS Experiment at the LHC. *Phys. Lett. B*, 716:30–61, 2012.

[2] Georges Aad et al. Observation of a new particle in the search for the Standard Model Higgs boson with the ATLAS detector at the LHC. *Phys. Lett. B*, 716:1–29, 2012.

[3] Spencer Chang and Markus Luty. The higgs trilinear coupling and the scale of new physics. *Journal of High Energy Physics*, 2020, 03 2020.

[4] D. A. Dicus and V. S. Mathur. Upper bounds on the values of masses in unified gauge theories. *Phys. Rev. D*, 7:3111–3114, 1973.

[5] Michael S. Chanowitz and Mary K. Gaillard. The TeV Physics of Strongly Interacting W's and Z's. *Nucl. Phys. B*, 261:379–431, 1985.

[6] Fady Bishara, Roberto Contino, and Juan Rojo. Higgs pair production in vector-boson fusion at the LHC and beyond. *Eur. Phys. J. C*, 77(7):481, 2017.

[7] Md Raju, Jyoti Prasad Saha, Dipankar Das, and Anirban Kundu. Double Higgs boson production as an exclusive probe for a sequential fourth generation with wrong-sign Yukawa couplings. *Phys. Rev. D*, 101(5):055036, 2020.

[8] F. Maltoni, E. Vryonidou, and M. Zaro. Top-quark mass effects in double and triple Higgs production in gluon-gluon fusion at NLO. *JHEP*, 11:079, 2014.

[9] Daniel de Florian and Javier Mazzitelli. Higgs pair production at next-to-next-to-leading logarithmic accuracy at the LHC. *JHEP*, 09:053, 2015.

[10] S. Borowka, N. Greiner, G. Heinrich, S. P. Jones, M. Kerner, J. Schlenk, U. Schubert, and T. Zirke. Higgs Boson Pair Production in Gluon Fusion at Next-to-Leading Order with Full Top-Quark Mass Dependence. *Phys. Rev. Lett.*, 117(1):012001, 2016. [Erratum: Phys.Rev.Lett. 117, 079901 (2016)].

[11] Charalampos Anastasiou, Claude Duhr, Falko Dulat, Elisabetta Furlan, Thomas Gehrmann, Franz Herzog, Achilleas Lazopoulos, and Bernhard Mistlberger. High precision determination of the gluon fusion Higgs boson cross-section at the LHC. *JHEP*, 05:058, 2016.

[12] Matthew McCullough. An Indirect Model-Dependent Probe of the Higgs Self-Coupling. *Phys. Rev. D*, 90(1):015001, 2014. [Erratum: Phys.Rev.D 92, 039903 (2015)].

[13] Martin Gorbahn and Ulrich Haisch. Indirect probes of the trilinear higgs coupling: gg $\rightarrow$ h and h $\rightarrow$. *Journal of High Energy Physics*, 2016(10), Oct 2016.

[14] G. Degrassi, P.P. Giardino, F. Maltoni, and D. Pagani. Probing the higgs self coupling via single higgs production at the lhc. *Journal of High Energy Physics*, 2016(12), Dec 2016.

[15] Wojciech Bizon, Martin Gorbahn, Ulrich Haisch, and Giulia Zanderighi. Constraints on the trilinear Higgs coupling from vector boson fusion and associated Higgs production at the LHC. *JHEP*, 07:083, 2017.

[16] Giuseppe Degrassi, Marco Fedele, and Pier Paolo Giardino. Constraints on the trilinear Higgs self coupling from precision observables. *JHEP*, 04:155, 2017.

[17] Graham D. Kribs, Andreas Maier, Heidi Rzehak, Michael Spannowsky, and Philip Waite. Electroweak oblique parameters as a probe of the trilinear Higgs boson self-interaction. *Phys. Rev. D*, 95(9):093004, 2017.

[18] Ece Asilar and Ozgur Durmus. Trilinear higgs coupling through h differential measurements. Presentation, 20 October 2020.

[19] Ece Asilar and Ozgur Durmus. H to tau tau and kappa lambda scan. Presentation, 7 October 2020.

[20] Ece Asilar and Ozgur Durmus. Calculating kinematic dependent variables for trilinear higgs coupling determination via single-higgs differential measurements in stxs bins. Presentation, 28 January 2021.

[21] Michael E. Peskin and Daniel V. Schroeder. *An Introduction to quantum field theory*. Addison-Wesley, Reading, USA, 1995.

[22] Peter W. Higgs. Broken symmetries, massless particles and gauge fields. *Phys. Lett.*, 12:132–133, 1964.

[23] Peter W. Higgs. Broken Symmetries and the Masses of Gauge Bosons. *Phys. Rev. Lett.*, 13:508–509, 1964.

[24] Emmy Noether. Invariant variation problems. *Transport Theory and Statistical Physics*, 1(3):186–207, jan 1971.

[25] Máximo Bañados and Ignacio A. Reyes. A short review on Noether's theorems, gauge symmetries and boundary terms. *Int. J. Mod. Phys. D*, 25(10):1630021, 2016.

[26] F. Halzen and Alan D. Martin. *QUARKS AND LEPTONS: AN INTRODUCTORY COURSE IN MODERN PARTICLE PHYSICS*. 1984.

[27] Fabio Maltoni, Davide Pagani, Ambresh Shivaji, and Xiaoran Zhao. Trilinear higgs coupling determination via single-higgs differential measurements at the lhc. *The European Physical Journal C*, 77(12), Dec 2017.

[28] Somnath Choudhury. Higgs boson production at the CMS experiment. *Nucl. Part. Phys. Proc.*, 282-284:182–188, 2017.

[29] H. M. Georgi, S. L. Glashow, M. E. Machacek, and Dimitri V. Nanopoulos. Higgs Bosons from Two Gluon Annihilation in Proton Proton Collisions. *Phys. Rev. Lett.*, 40:692, 1978.

[30] CERN. Experiments | cern. `https://home.cern/science/experiments`. (accessed: April 27, 2022).

[31] G. Aad et al. The ATLAS Experiment at the CERN Large Hadron Collider. *JINST*, 3:S08003, 2008.

[32] S. Chatrchyan et al. The CMS Experiment at the CERN LHC. *JINST*, 3:S08004, 2008.

[33] K. Aamodt et al. The ALICE experiment at the CERN LHC. *JINST*, 3:S08002, 2008.

[34] A. Augusto Alves, Jr. et al. The LHCb Detector at the LHC. *JINST*, 3:S08005, 2008.

[35] G. Anelli et al. The TOTEM experiment at the CERN Large Hadron Collider. *JINST*, 3:S08007, 2008.

[36] O. Adriani et al. The LHCf detector at the CERN Large Hadron Collider. *JINST*, 3:S08006, 2008.

[37] A. M. Sirunyan et al. Particle-flow reconstruction and global event description with the CMS detector. *JINST*, 12(10):P10003, 2017.

[38] G. Aad and ATLAS Collaboration. Measurements of the higgs boson production and decay rates and coupling strengths using pp collision data at $$\sqrt{s}=7$$ s = 7 and 8 TeV in the ATLAS experiment. *The European Physical Journal C*, 76(1), jan 2016.

[39] V. Khachatryan and CMS Collaboration. Precise determination of the mass of the higgs boson and tests of compatibility of its couplings with the standard model predictions using proton collisions at 7 and 8 $$\, \text {TeV}$$ TeV. *The European Physical Journal C*, 75(5), may 2015.

[40] G. Aad and ATLAS Collaboration. Combined measurements of higgs boson production and decay using up to 80 fb-1 of proton-proton collision data at s=13 TeV collected with the ATLAS experiment. *Physical Review D*, 101(1), jan 2020.

[41] A. M. Sirunyan and The CMS Collaboration. Combined measurements of higgs boson couplings in proton–proton collisions at $$\sqrt{s}=13\, \text {te}\text {v} $$. *The European Physical Journal C*, 79(5), may 2019.

[42] ATLAS and CMS Collaborations. Measurements of the higgs boson production and decay rates and constraints on its couplings from a combined ATLAS and CMS analysis of the LHC pp collision data at s = 7 $$ \sqrt{s}=7 $$ and 8 TeV. *Journal of High Energy Physics*, 2016(8), aug 2016.

[43] A. M. Sirunyan and CMS Collaboration. Combination of searches for higgs boson pair production in proton-proton collisions at $\sqrt{s} = 13\ \mathrm{TeV}$. *Phys. Rev. Lett.*, 122:121803, Mar 2019.

[44] Combined Higgs boson production and decay measurements with up to 137 fb^{-1} of proton-proton collision data at $\sqrt{s}$ = 13 TeV. 2020.

[45] G. Aad and ATLAS Colaboration. Combination of searches for higgs boson pairs in pp collisions at s=13tev with the atlas detector. *Physics Letters B*, 800:135103, 2020.

[46] Constraints on the Higgs boson self-coupling from the combination of single-Higgs and double-Higgs production analyses performed with the ATLAS experiment. 10 2019.

[47] Stefano Di Vita, Christophe Grojean, Giuliano Panico, Marc Riembau, and Thibaud Vantalon. A global view on the Higgs self-coupling. *JHEP*, 09:069, 2017.

[48] T. Stelzer and W. F. Long. Automatic generation of tree level helicity amplitudes. *Comput. Phys. Commun.*, 81:357–371, 1994.

[49] Fabio Maltoni and Tim Stelzer. MadEvent: Automatic event generation with MadGraph. *JHEP*, 02:027, 2003.

[50] Johan Alwall, Pavel Demin, Simon de Visscher, Rikkert Frederix, Michel Herquet, Fabio Maltoni, Tilman Plehn, David L. Rainwater, and Tim Stelzer. MadGraph/MadEvent v4: The New Web Generation. *JHEP*, 09:028, 2007.

[51] A. Pukhov, E. Boos, M. Dubinin, V. Edneral, V. Ilyin, D. Kovalenko, A. Kryukov, V. Savrin, S. Shichanin, and A. Semenov. CompHEP: A Package for evaluation of Feynman diagrams and integration over multiparticle phase space. 8 1999.

[52] E. Boos, V. Bunichev, M. Dubinin, L. Dudko, V. Ilyin, A. Kryukov, V. Edneral, V. Savrin, A. Semenov, and A. Sherstnev. CompHEP 4.4: Automatic computations from Lagrangians to events. *Nucl. Instrum. Meth. A*, 534:250–259, 2004.

[53] A. Pukhov. CalcHEP 2.3: MSSM, structure functions, event generation, batchs, and generation of matrix elements for other packages. 12 2004.

[54] Tanju Gleisberg, Stefan Hoeche, Frank Krauss, Andreas Schalicke, Steffen

Schumann, and Jan-Christopher Winter. SHERPA 1. alpha: A Proof of concept version. *JHEP*, 02:056, 2004.

[55] W. Kilian. WHIZARD manual. pages 1924–1980, 1 2001.

[56] Johan Alwall, Michel Herquet, Fabio Maltoni, Olivier Mattelaer, and Tim Stelzer. MadGraph 5 : Going Beyond. *JHEP*, 06:128, 2011.

[57] Adam Alloul, Neil D. Christensen, Céline Degrande, Claude Duhr, and Benjamin Fuks. FeynRules 2.0 - A complete toolbox for tree-level phenomenology. *Comput. Phys. Commun.*, 185:2250–2300, 2014.

[58] Wolfram Research, Inc. Mathematica, Version 13.0.0. Champaign, IL, 2021.

[59] Celine Degrande, Claude Duhr, Benjamin Fuks, David Grellscheid, Olivier Mattelaer, and Thomas Reiter. UFO - The Universal FeynRules Output. *Comput. Phys. Commun.*, 183:1201–1214, 2012.

[60] Stefano Frixione and Bryan R. Webber. Matching NLO QCD computations and parton shower simulations. *JHEP*, 06:029, 2002.

[61] J. Alwall, R. Frederix, S. Frixione, V. Hirschi, F. Maltoni, O. Mattelaer, H.-S. Shao, T. Stelzer, P. Torrielli, and M. Zaro. The automated computation of tree-level and next-to-leading order differential cross sections, and their matching to parton shower simulations. *Journal of High Energy Physics*, 2014(7), Jul 2014.

[62] R. Frederix, S. Frixione, V. Hirschi, D. Pagani, H. S. Shao, and M. Zaro. The automation of next-to-leading order electroweak calculations. *JHEP*, 07:185, 2018. [Erratum: JHEP 11, 085 (2021)].

[63] D. de Florian et al. Handbook of LHC Higgs Cross Sections: 4. Deciphering the Nature of the Higgs Sector. 2/2017, 10 2016.

[64] CMS Collaboration. A Study of the Single Higgs Modelling for Constraining Higgs Boson Trilinear Self-coupling in STXS (1.2) Measurements. Technical report, CERN, Geneva, Jan 2022.

[65] Jon Butterworth et al. PDF4LHC recommendations for LHC Run II. *J. Phys. G*, 43:023001, 2016.

Appendix A

COMPLETE DIAGRAMS

All diagrams that is produced from the calculations, both LO and NLO ($\mathcal{O}(\lambda)$), are presented here. The diagrams automatically created by MADGRAPH5_AMC@NLO . The package used for the calculation and creation of the diagrams is Trilinear-RW package with its own UFO model. See Chapter 4 for more details.

A.1 HW

A.1.1 LO diagrams of HW channel

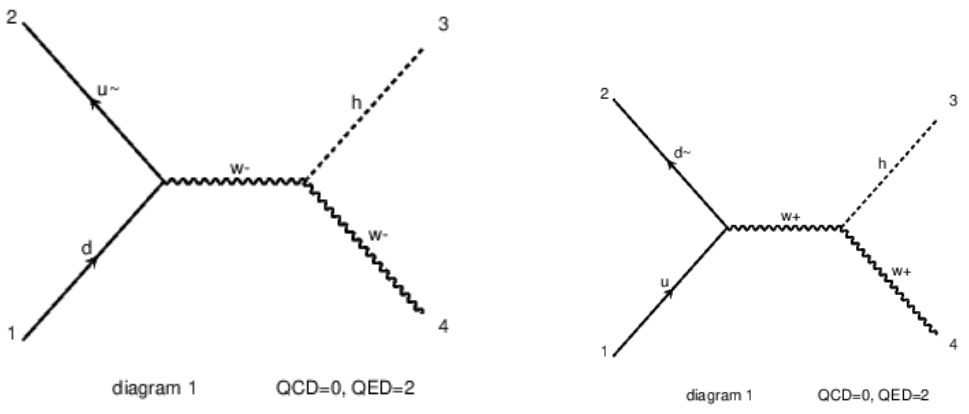

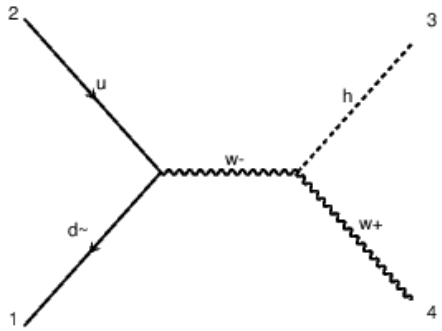

diagram 1 QCD=0, QED=2

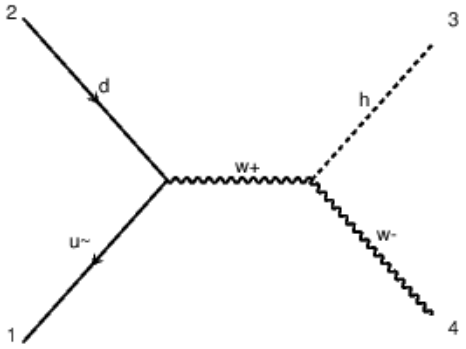

diagram 1 QCD=0, QED=2

A.1.2 $\mathcal{O}(\lambda)$ diagrams of HW channel

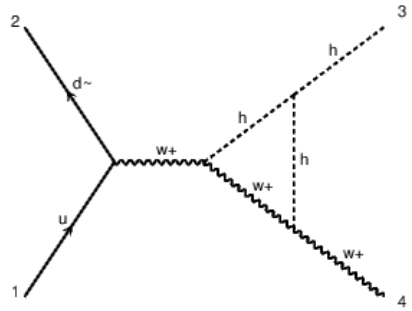

diagram 1 QCD=0, QED=4

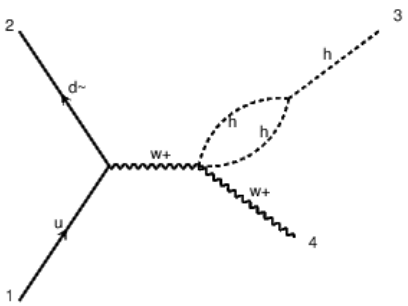

diagram 2 QCD=0, QED=4

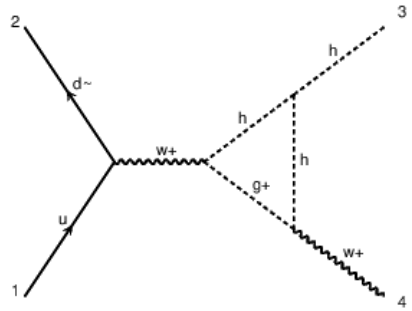

diagram 3 QCD=0, QED=4

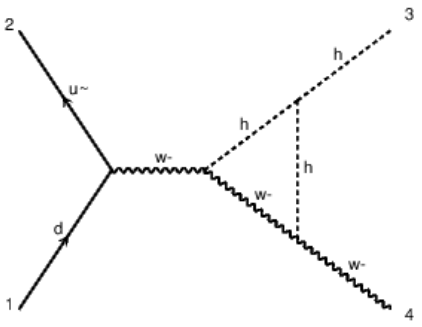

diagram 1 QCD=0, QED=4

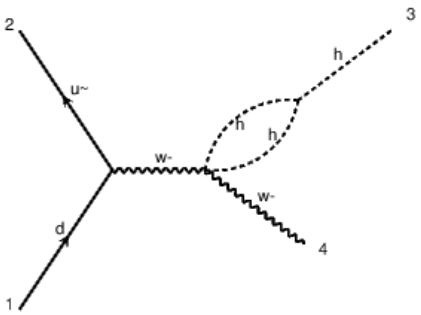

diagram 2 QCD=0, QED=4

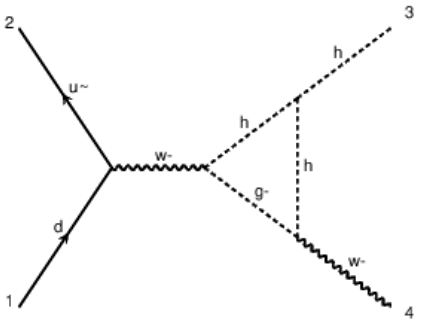

diagram 3 QCD=0, QED=4

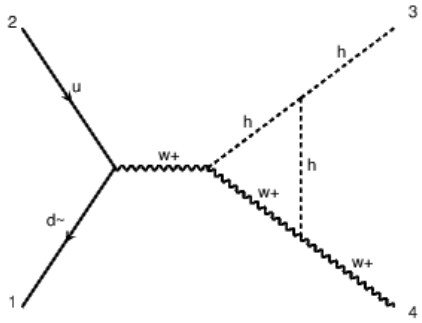

diagram 1 QCD=0, QED=4

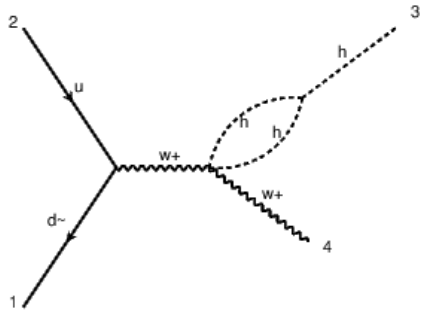

diagram 2 QCD=0, QED=4

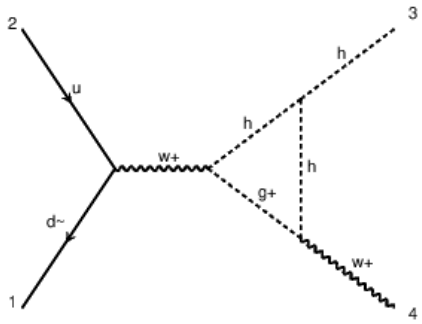

diagram 3 QCD=0, QED=4

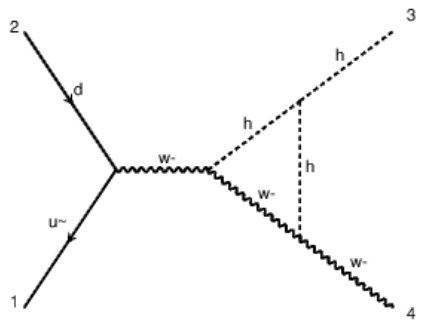

diagram 1 QCD=0, QED=4

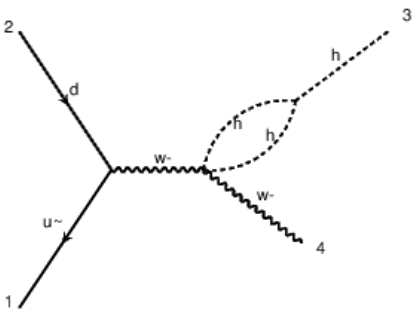

diagram 2 QCD=0, QED=4

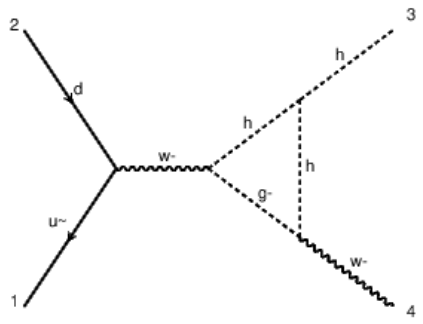

diagram 3 QCD=0, QED=4

A.2 HZ

A.2.1 LO diagrams of HZ channel

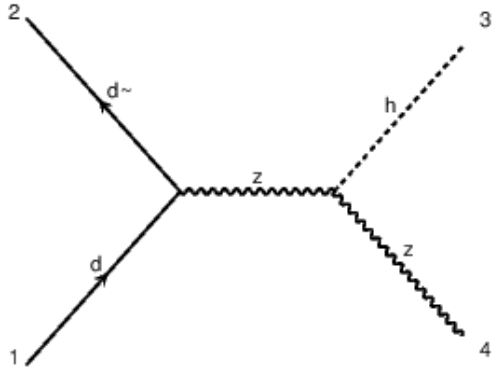

diagram 1 QCD=0, QED=2

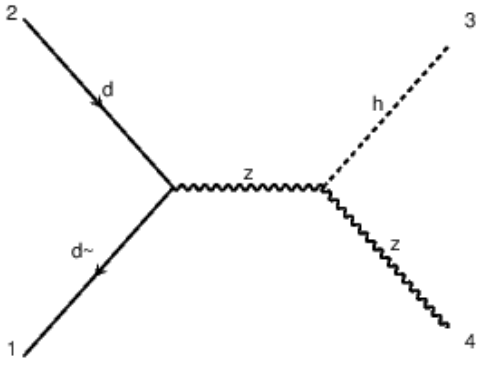

diagram 1 QCD=0, QED=2

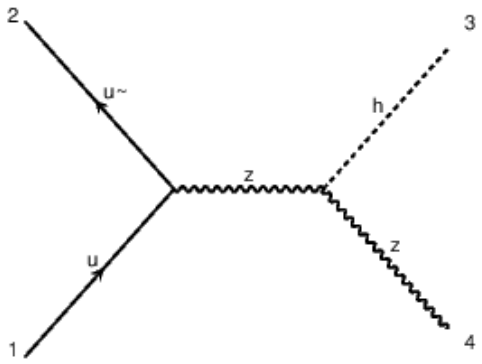

diagram 1 QCD=0, QED=2

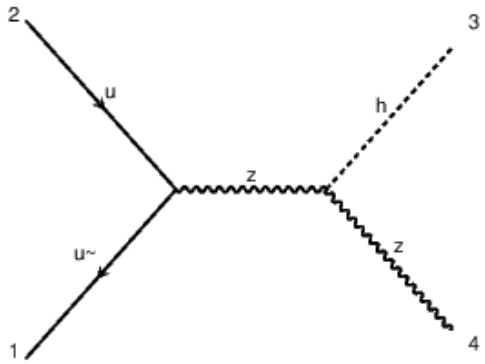

diagram 1 QCD=0, QED=2

A.2.2 $\mathcal{O}(\lambda)$ diagrams of HZ channel

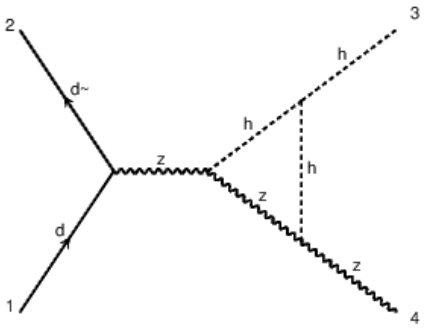

diagram 1 QCD=0, QED=4

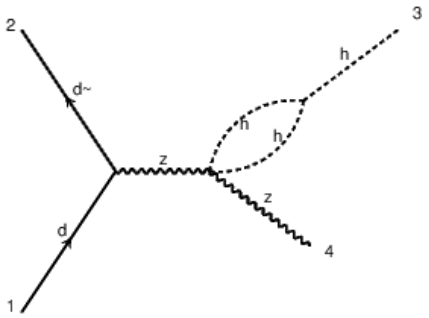

diagram 2 QCD=0, QED=4

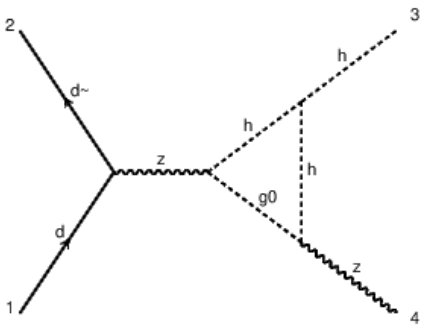

diagram 3 QCD=0, QED=4

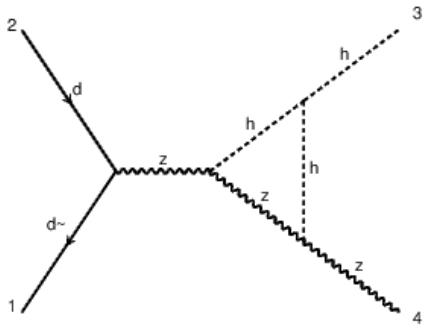

diagram 1 QCD=0, QED=4

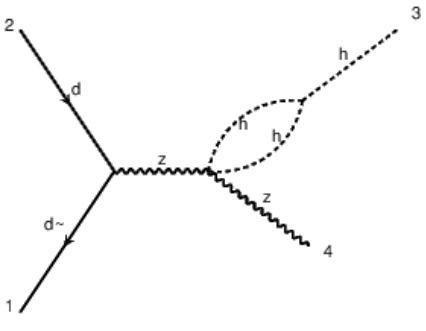

diagram 2 QCD=0, QED=4

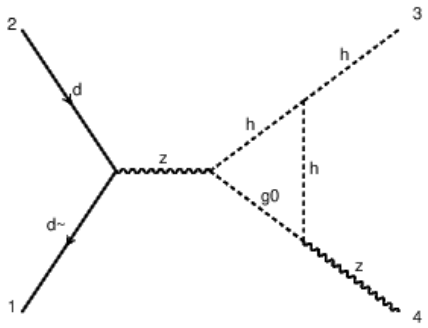

diagram 3 QCD=0, QED=4

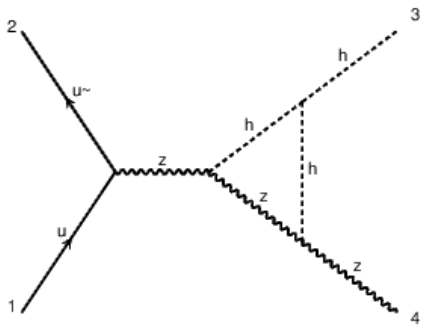

diagram 1 QCD=0, QED=4

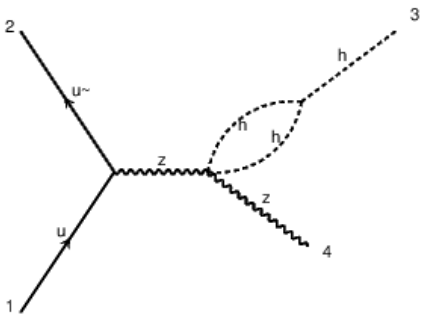

diagram 2 QCD=0, QED=4

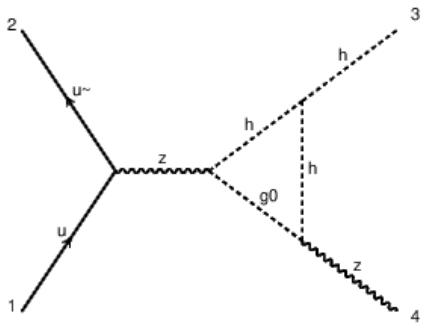

diagram 3 QCD=0, QED=4

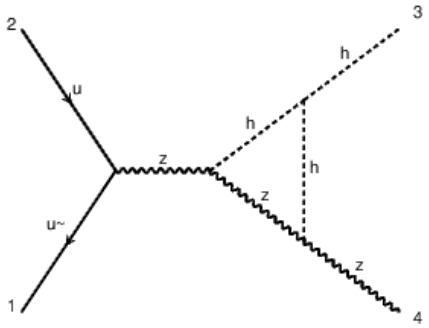

diagram 1 QCD=0, QED=4

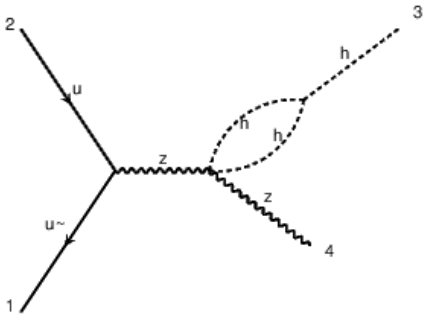

diagram 2 QCD=0, QED=4

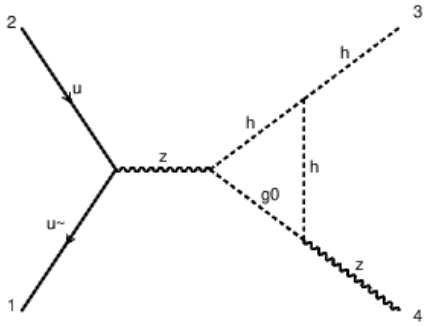

diagram 3 QCD=0, QED=4

A.3 $t\bar{t}H$

A.3.1 LO diagrams of $t\bar{t}H$ channel

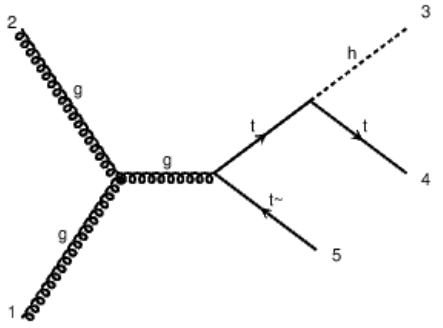

born diagram 1 QCD=2, QED=1

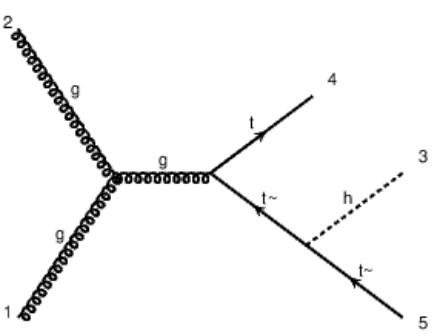

born diagram 2 QCD=2, QED=1

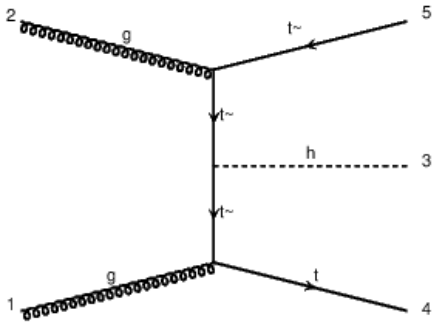

born diagram 3 QCD=2, QED=1

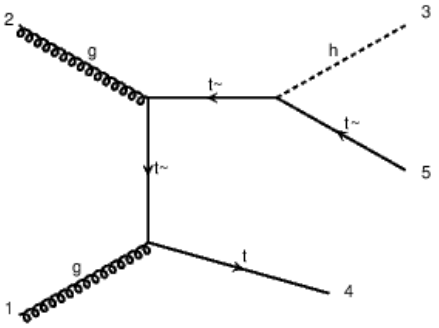

born diagram 4 QCD=2, QED=1

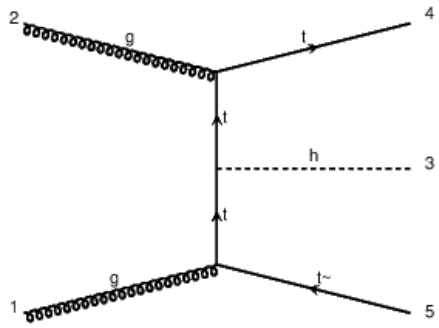

born diagram 5 QCD=2, QED=1

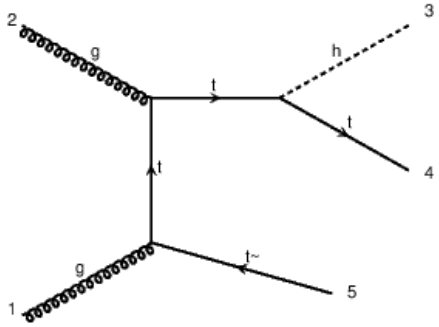

born diagram 6 QCD=2, QED=1

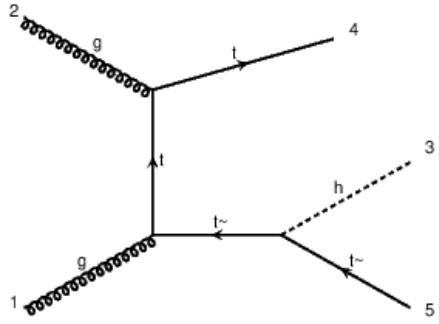

born diagram 7 QCD=2, QED=1

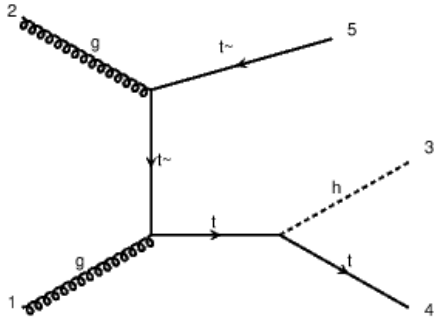

born diagram 8 QCD=2, QED=1

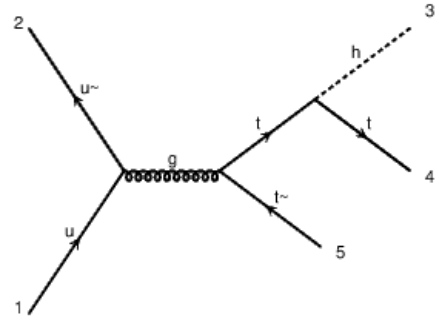

diagram 1 QCD=2, QED=1

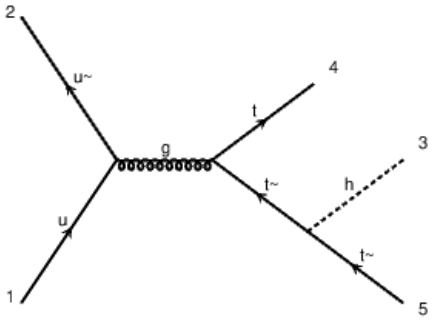

diagram 2 QCD=2, QED=1

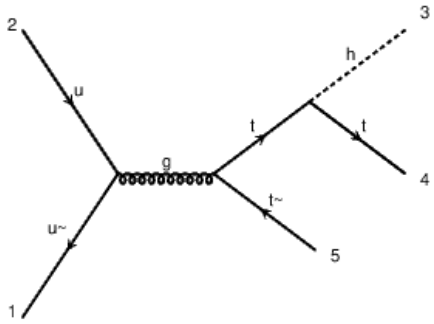

diagram 1 QCD=2, QED=1

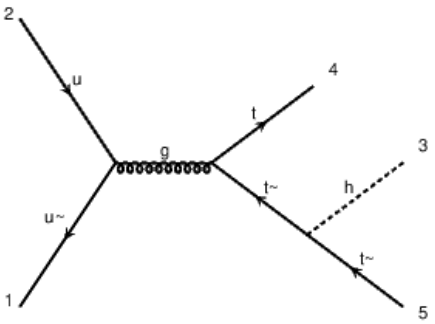

diagram 2 QCD=2, QED=1

A.3.2 $\mathcal{O}(\lambda)$ diagrams of $t\bar{t}H$ channel

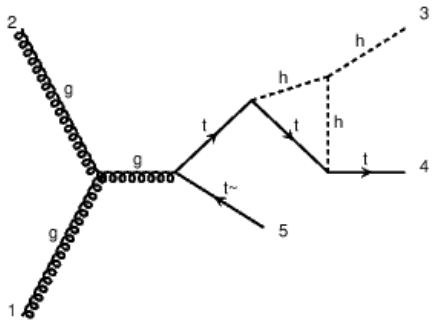

diagram 1 QCD=2, QED=3

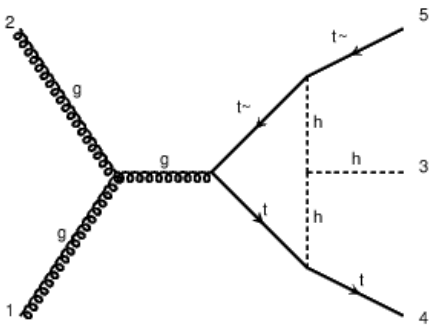

diagram 2 QCD=2, QED=3

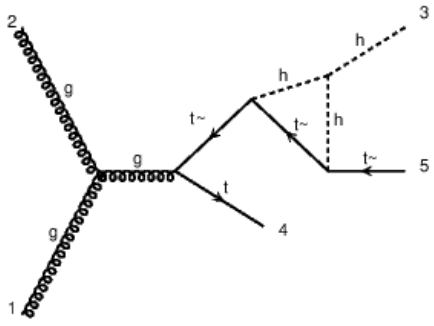

diagram 3 QCD=2, QED=3

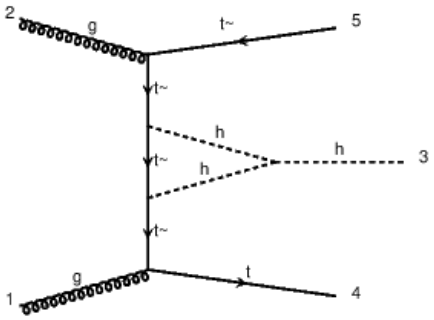

diagram 4 QCD=2, QED=3

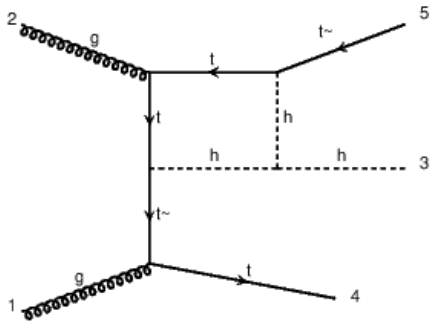

diagram 5 QCD=2, QED=3

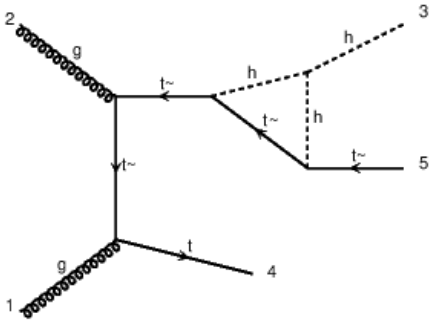

diagram 6 QCD=2, QED=3

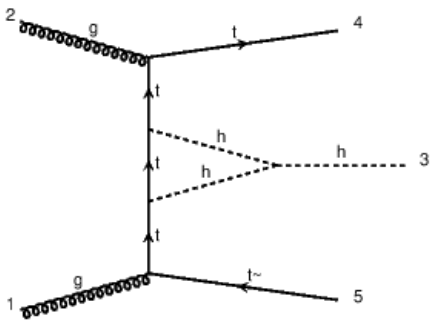

diagram 7 QCD=2, QED=3

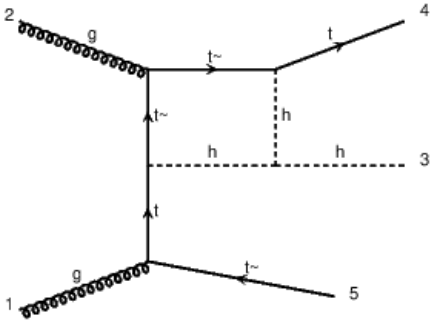

diagram 8 QCD=2, QED=3

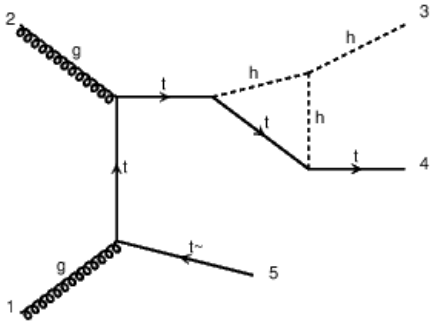

diagram 9 QCD=2, QED=3

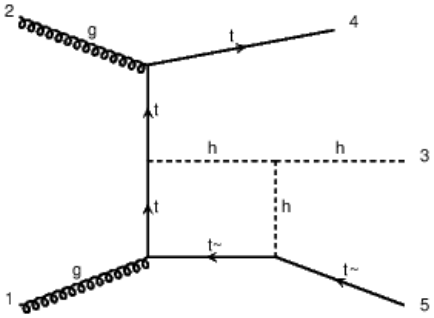

diagram 10 QCD=2, QED=3

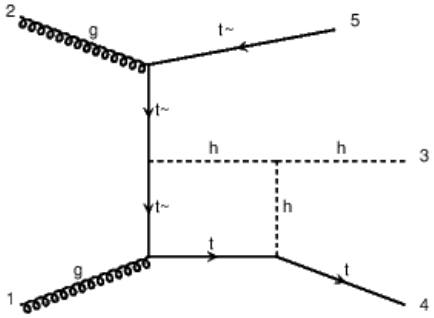

diagram 11 QCD=2, QED=3

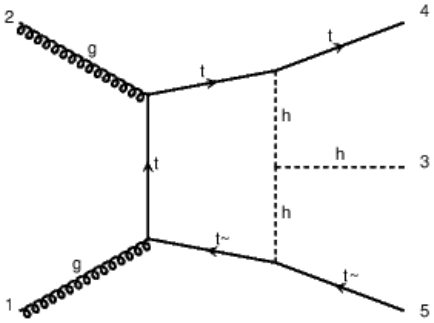

diagram 12 QCD=2, QED=3

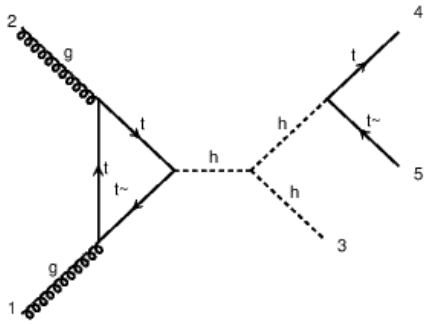

diagram 13 QCD=2, QED=3

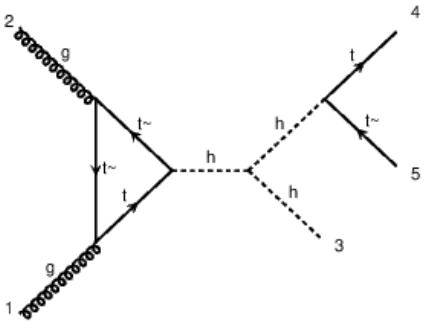

diagram 14 QCD=2, QED=3

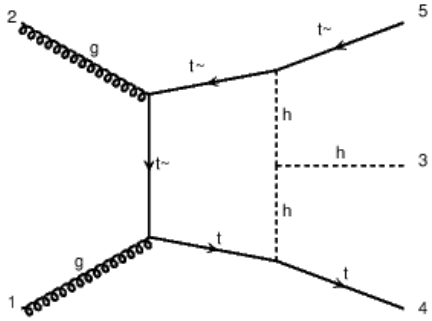

diagram 15 QCD=2, QED=3

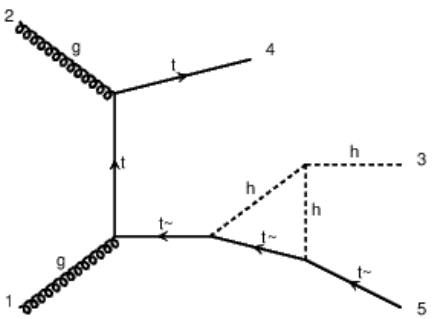

diagram 16 QCD=2, QED=3

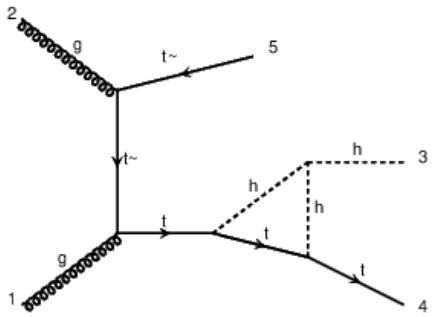

diagram 17 QCD=2, QED=3

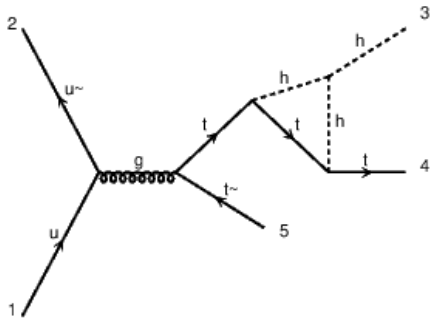

diagram 1 QCD=2, QED=3

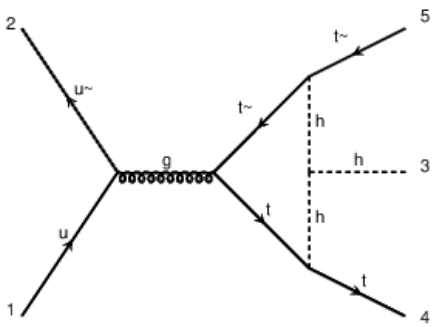

diagram 2 QCD=2, QED=3

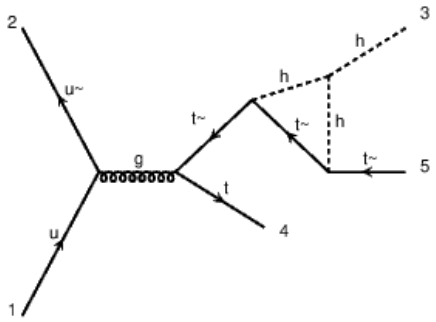

diagram 3 QCD=2, QED=3

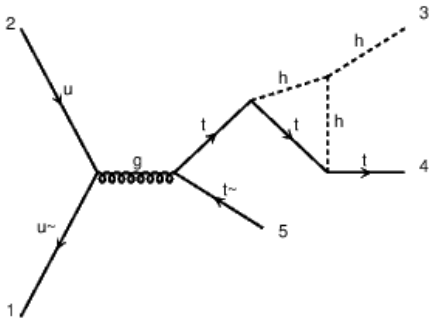

diagram 1 QCD=2, QED=3

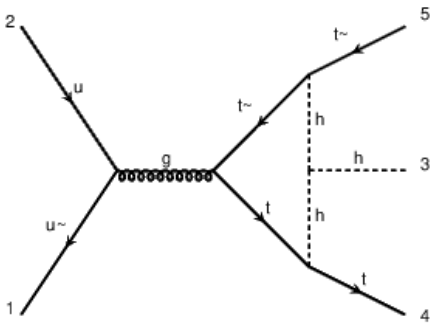

diagram 2 QCD=2, QED=3

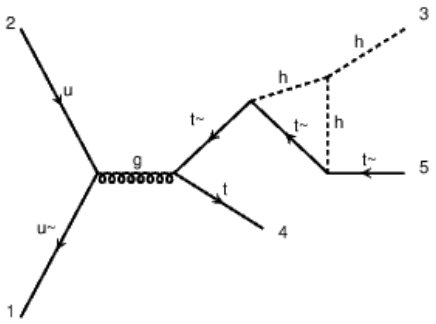

diagram 3 QCD=2, QED=3

A.4 tHj

A.4.1 LO diagrams of tHj channel

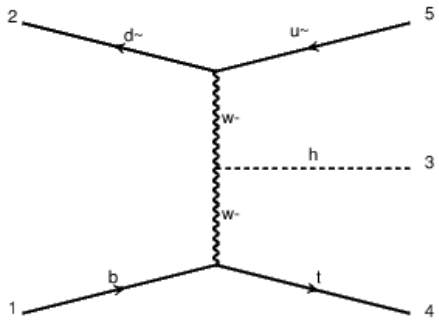

diagram 1 QCD=0, QED=3

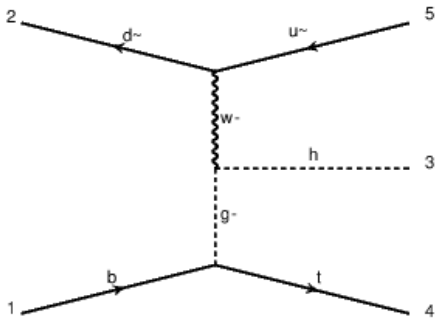

diagram 2 QCD=0, QED=3

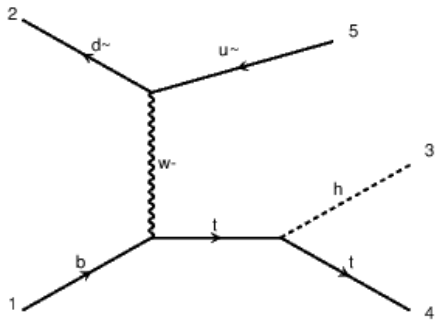

diagram 3 QCD=0, QED=3

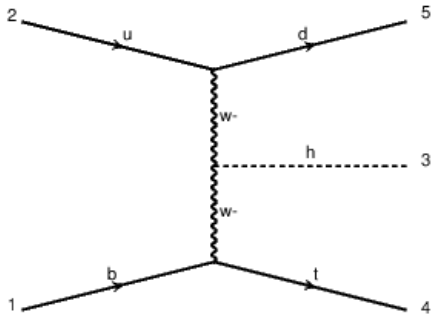

diagram 1 QCD=0, QED=3

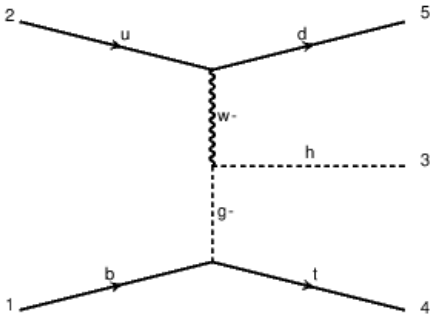

diagram 2 QCD=0, QED=3

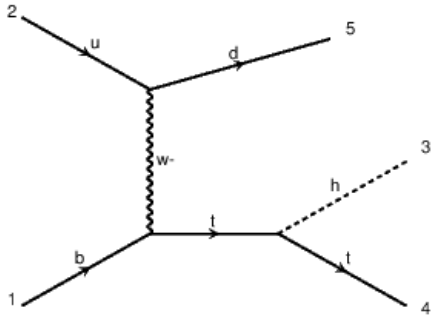

diagram 3 QCD=0, QED=3

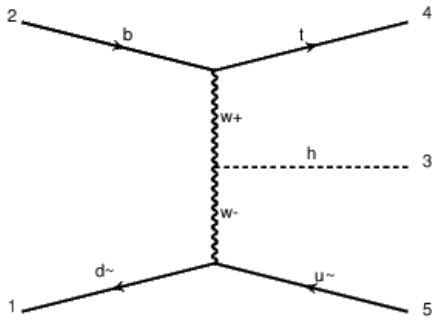

diagram 1 QCD=0, QED=3

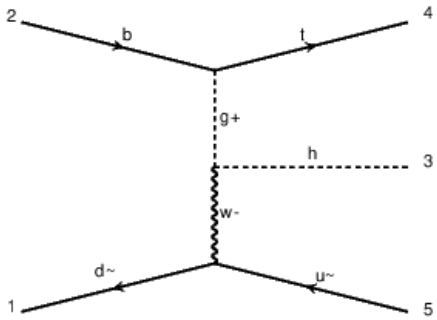

diagram 2 QCD=0, QED=3

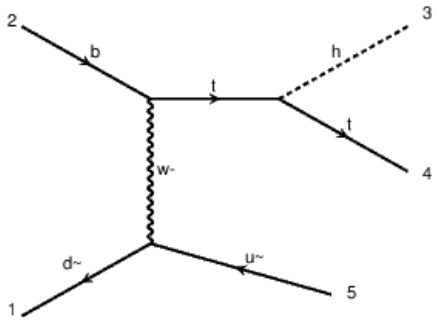

diagram 3 QCD=0, QED=3

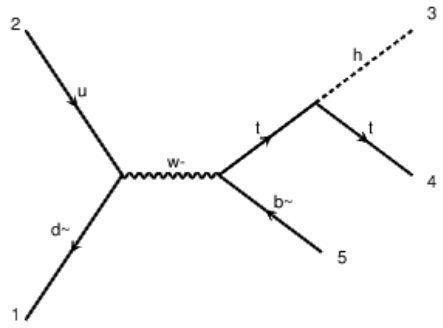

diagram 1 QCD=0, QED=3

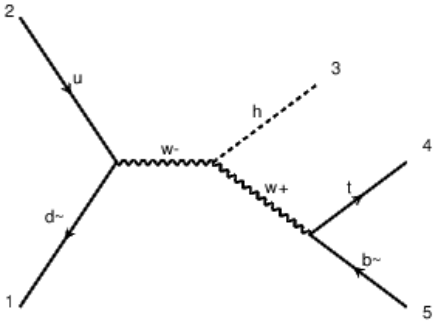

diagram 2 QCD=0, QED=3

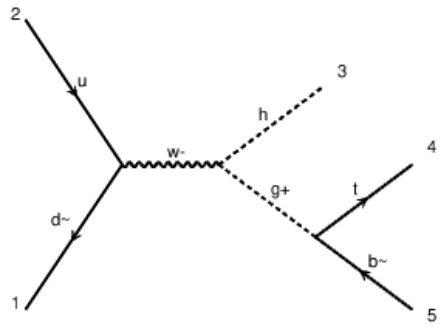

diagram 3 QCD=0, QED=3

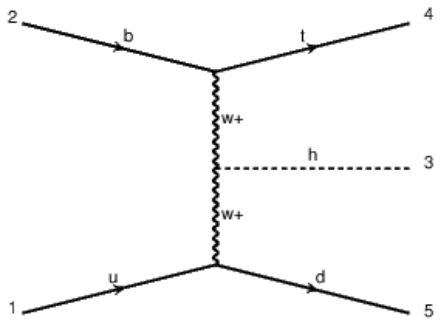

diagram 1 QCD=0, QED=3

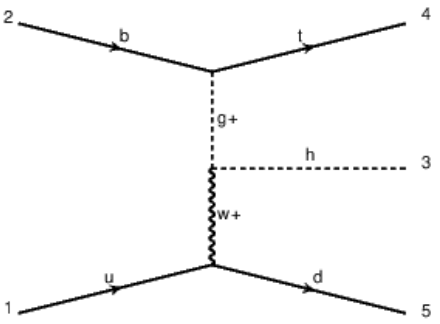

diagram 2 QCD=0, QED=3

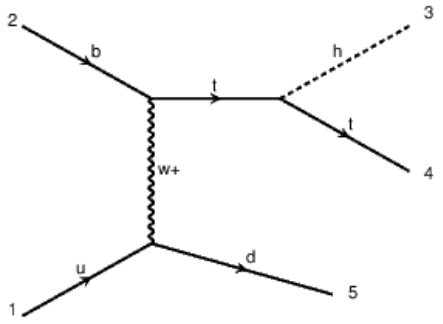

diagram 3 QCD=0, QED=3

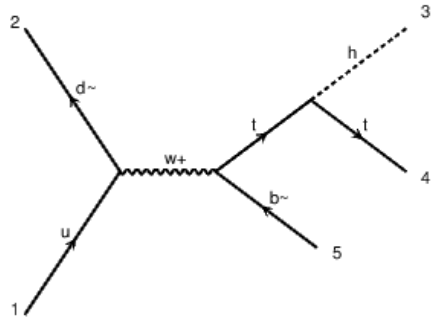

diagram 1 QCD=0, QED=3

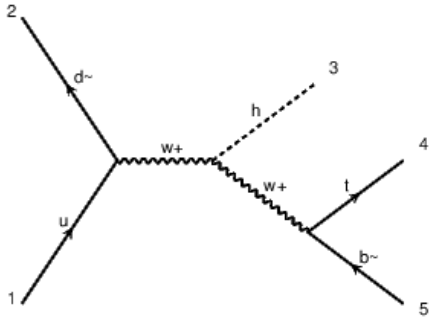

diagram 2 QCD=0, QED=3

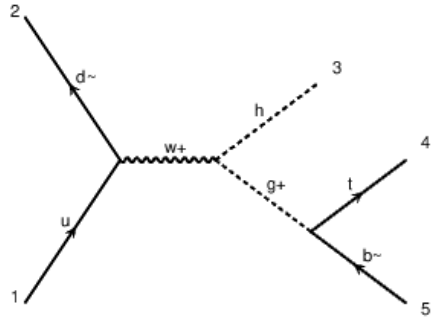

diagram 3 QCD=0, QED=3

A.4.2 $\mathcal{O}(\lambda)$ diagrams of tHj channel

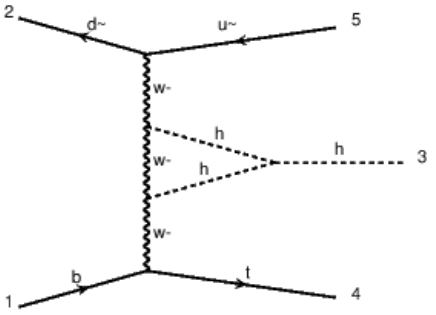

diagram 1 QCD=0, QED=5

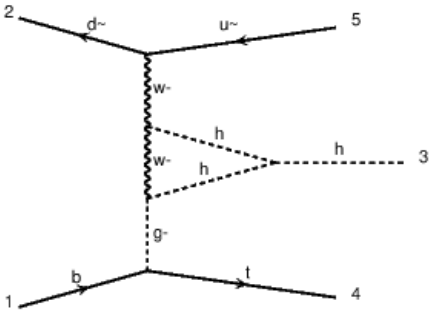

diagram 2 QCD=0, QED=5

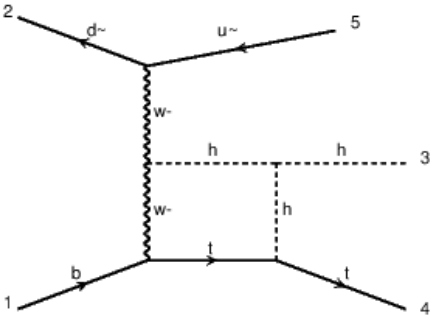

diagram 3 QCD=0, QED=5

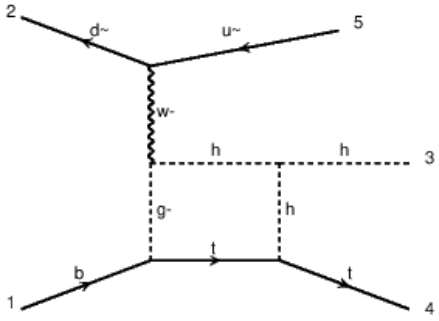

diagram 4 QCD=0, QED=5

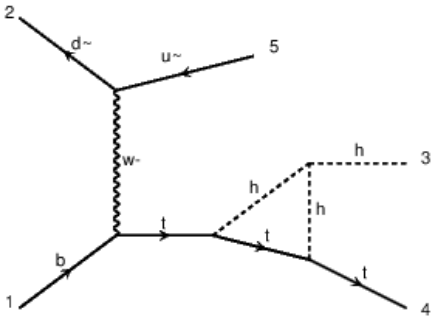

diagram 5 QCD=0, QED=5

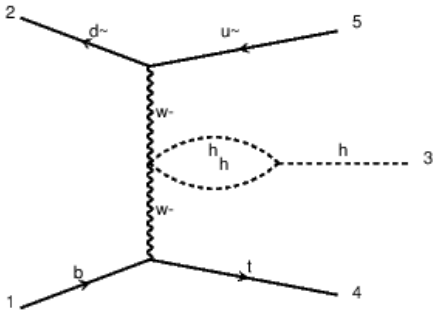

diagram 6 QCD=0, QED=5

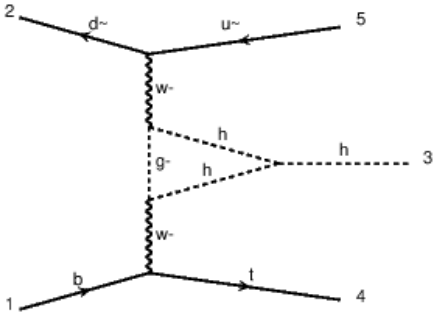

diagram 7 QCD=0, QED=5

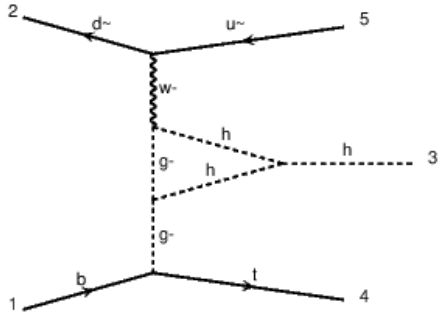

diagram 8 QCD=0, QED=5

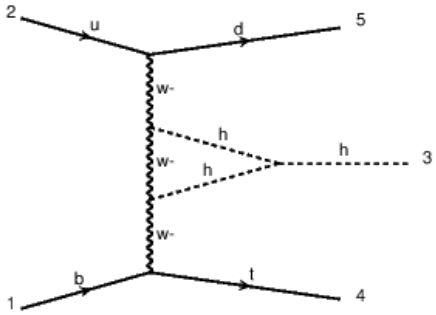

diagram 1 QCD=0, QED=5

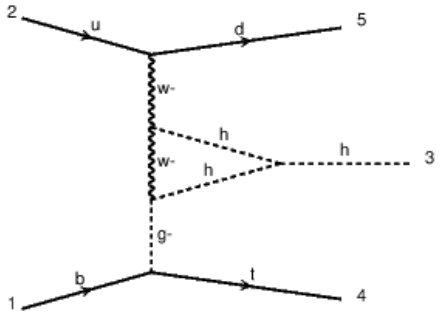

diagram 2 QCD=0, QED=5

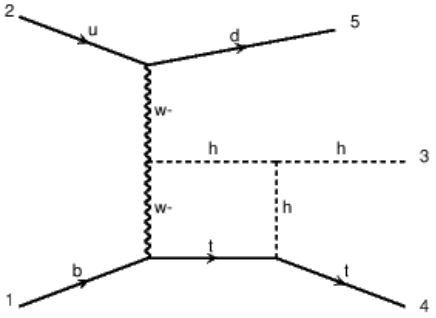

diagram 3 QCD=0, QED=5

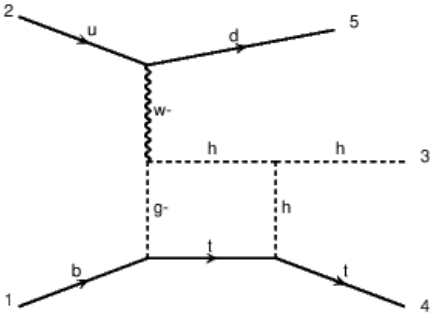

diagram 4 QCD=0, QED=5

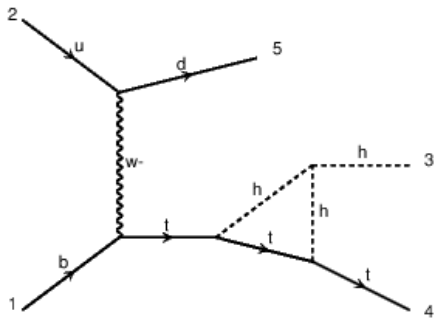

diagram 5 QCD=0, QED=5

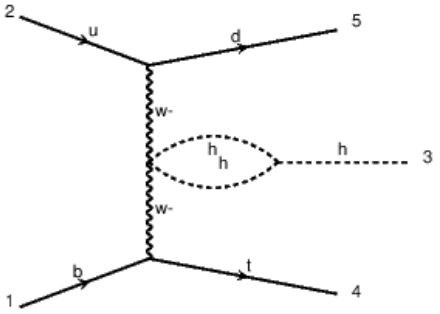

diagram 6 QCD=0, QED=5

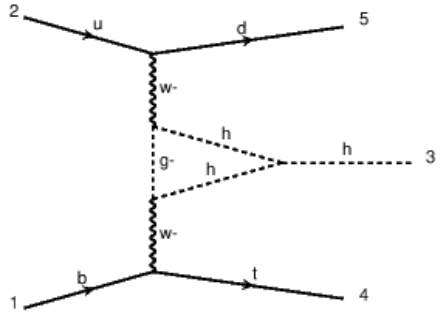

diagram 7 QCD=0, QED=5

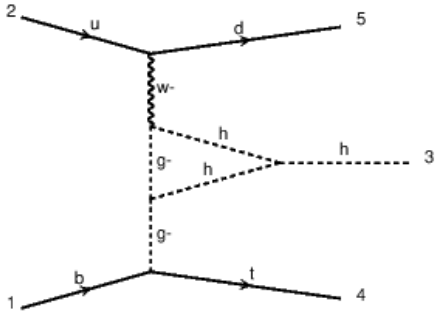

diagram 8 QCD=0, QED=5

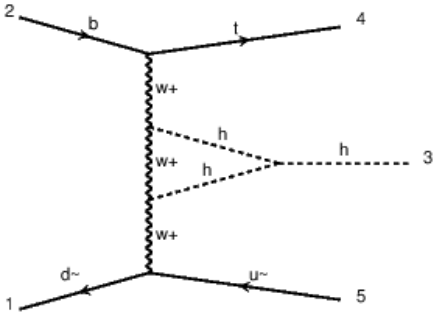

diagram 1 QCD=0, QED=5

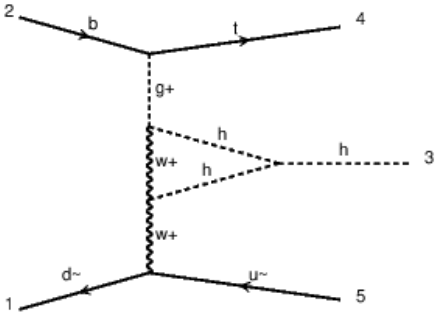

diagram 2 QCD=0, QED=5

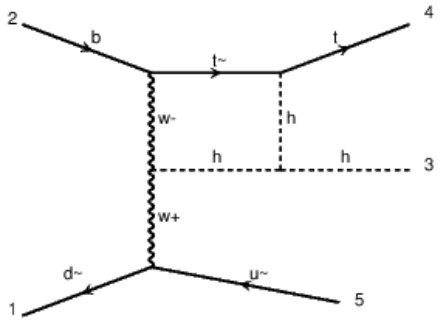

diagram 3 QCD=0, QED=5

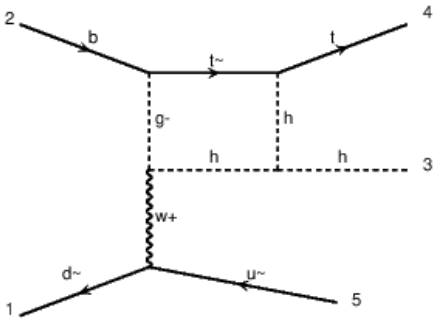

diagram 4 QCD=0, QED=5

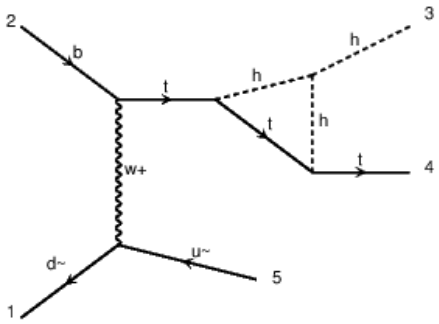

diagram 5 QCD=0, QED=5

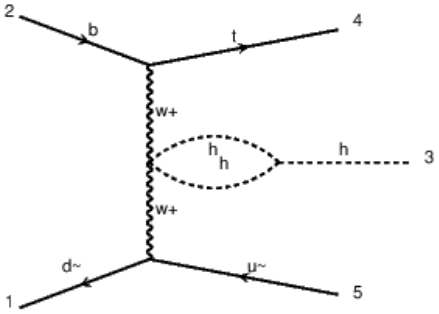

diagram 6 QCD=0, QED=5

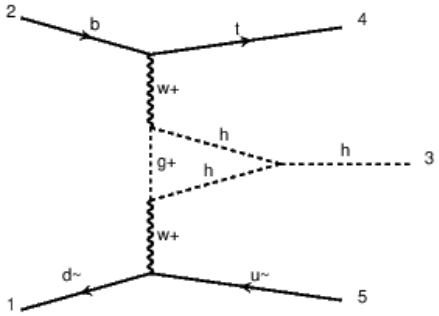

diagram 7 QCD=0, QED=5

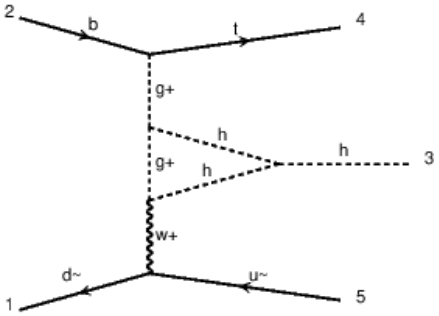

diagram 8 QCD=0, QED=5

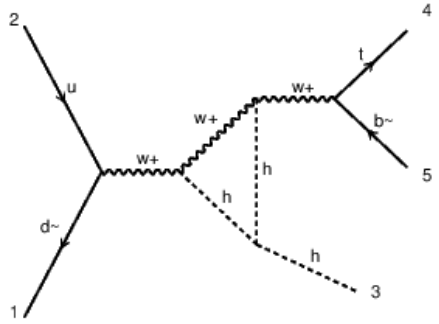

diagram 1 QCD=0, QED=5

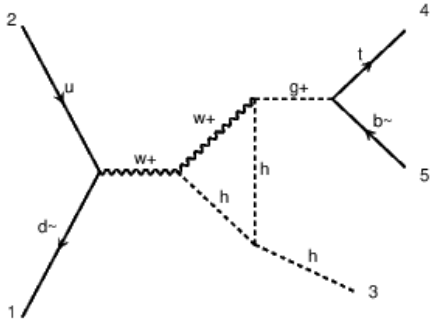

diagram 2 QCD=0, QED=5

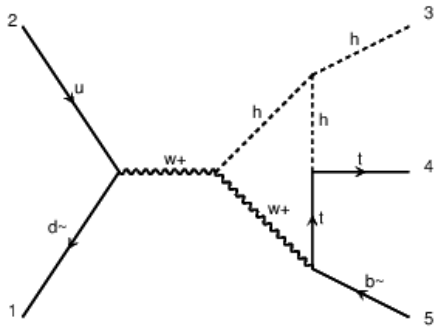

diagram 3 QCD=0, QED=5

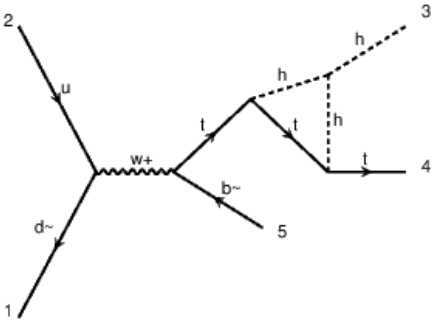

diagram 4 QCD=0, QED=5

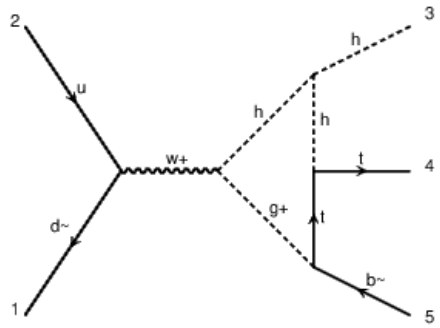

diagram 5 QCD=0, QED=5

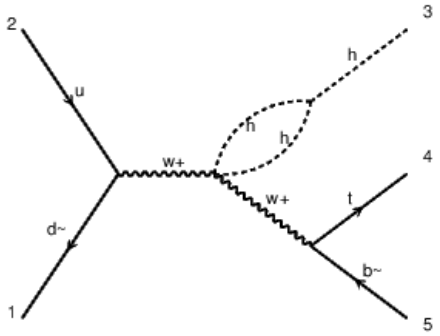

diagram 6 QCD=0, QED=5

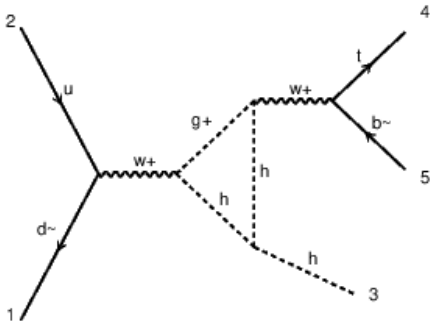

diagram 7 QCD=0, QED=5

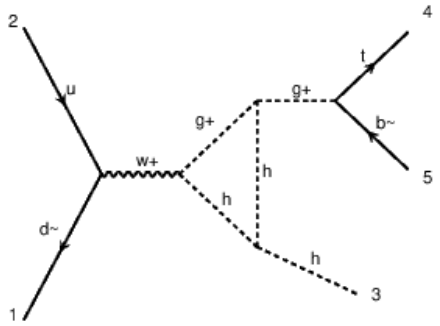

diagram 8 QCD=0, QED=5

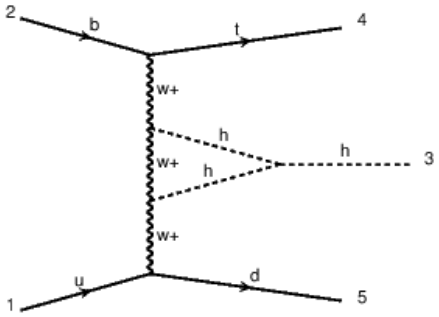

diagram 1 QCD=0, QED=5

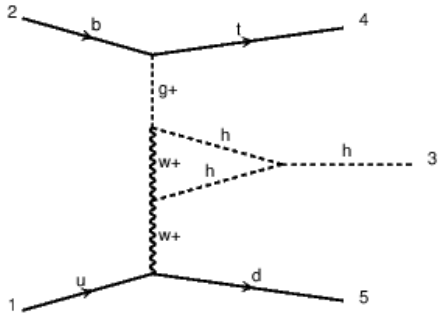

diagram 2 QCD=0, QED=5

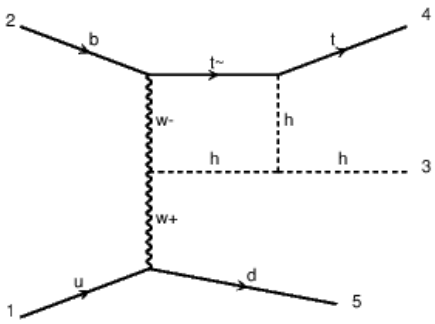

diagram 3 QCD=0, QED=5

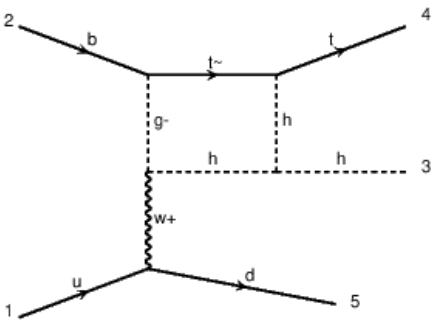

diagram 4 QCD=0, QED=5

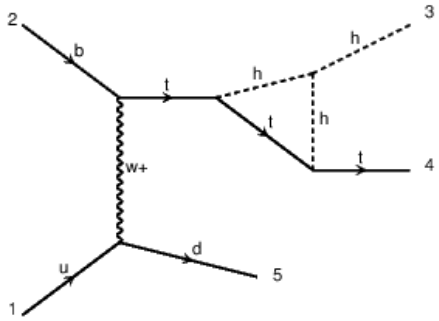

diagram 5 QCD=0, QED=5

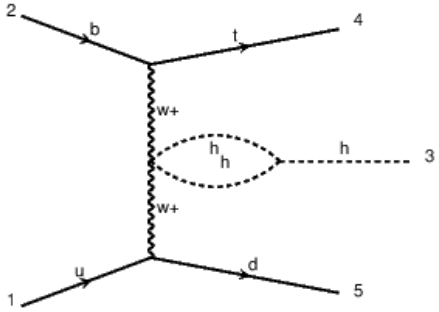

diagram 6 QCD=0, QED=5

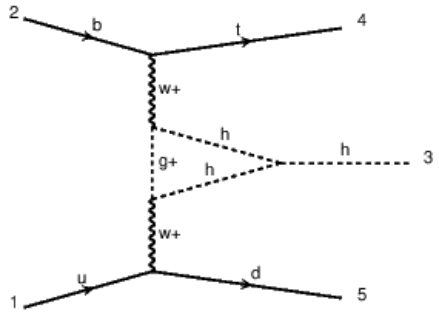

diagram 7 QCD=0, QED=5

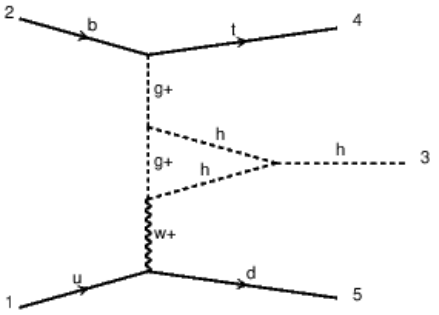

diagram 8 QCD=0, QED=5

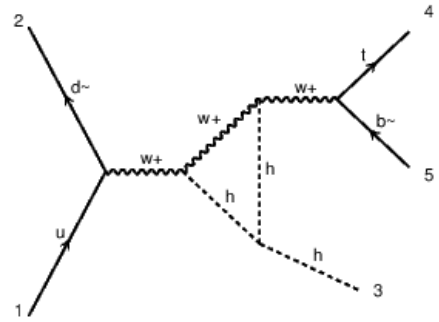

diagram 1 QCD=0, QED=5

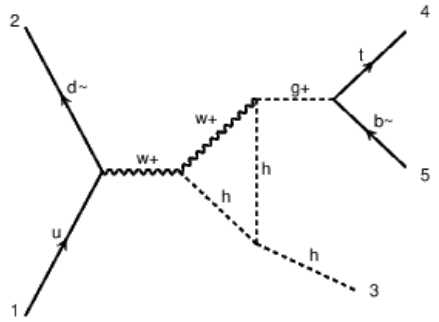

diagram 2 QCD=0, QED=5

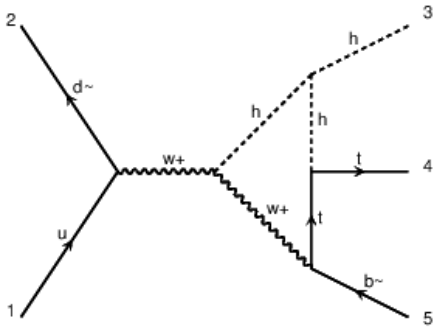

diagram 3 QCD=0, QED=5

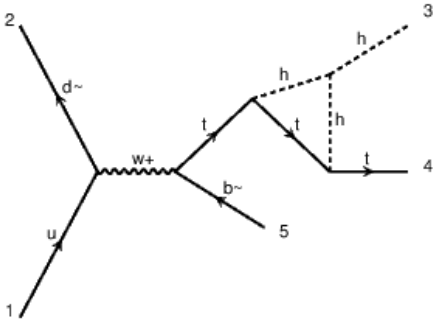

diagram 4 QCD=0, QED=5

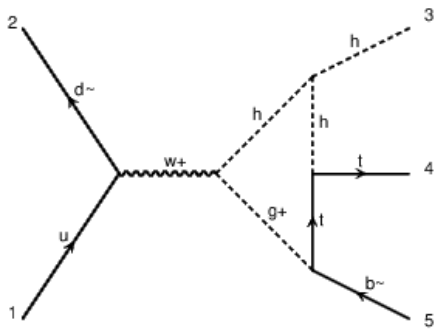

diagram 5 QCD=0, QED=5

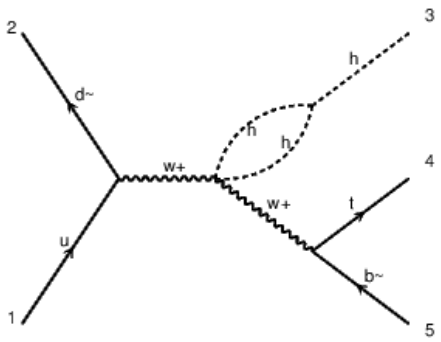

diagram 6 QCD=0, QED=5

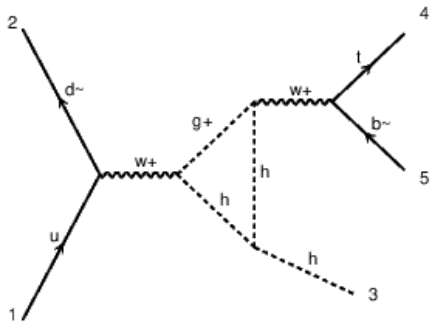

diagram 7 QCD=0, QED=5

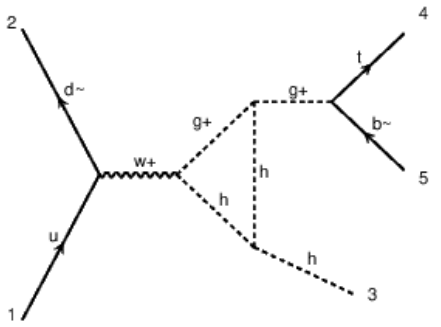

diagram 8 QCD=0, QED=5

A.5 VBF

A.5.1 LO diagrams of VBF channel

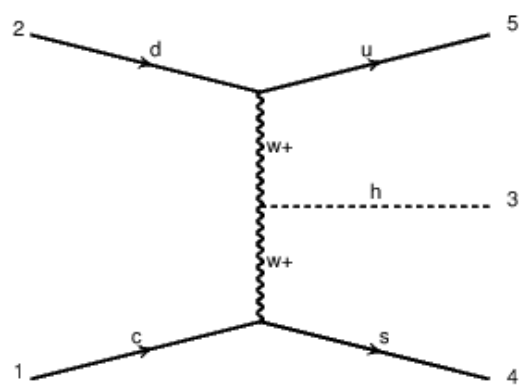

diagram 1 QCD=0, QED=3

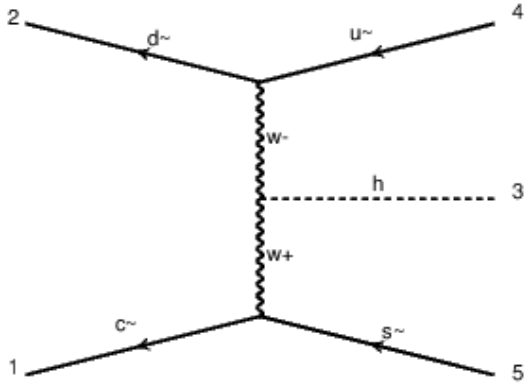

diagram 1 QCD=0, QED=3

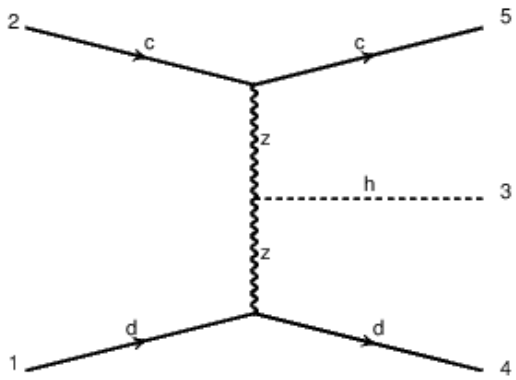

diagram 1 QCD=0, QED=3

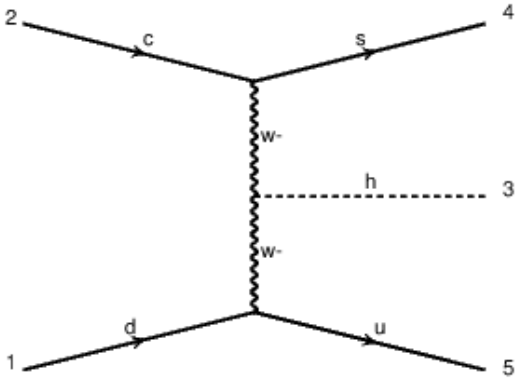

diagram 1 QCD=0, QED=3

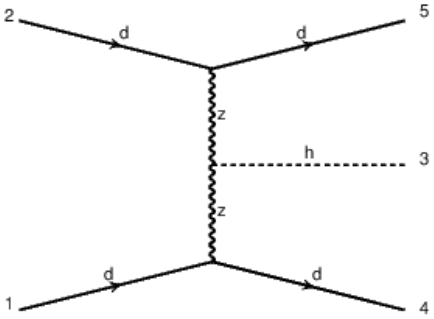

diagram 1 QCD=0, QED=3

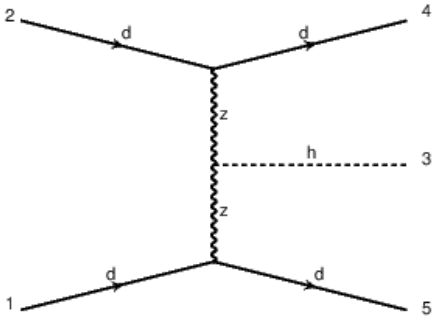

diagram 2 QCD=0, QED=3

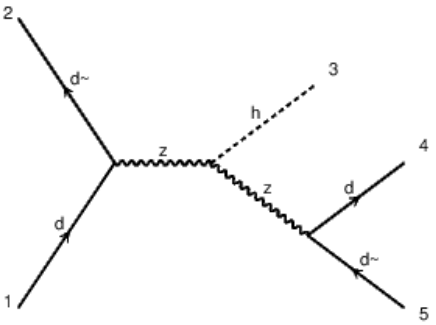

diagram 1 QCD=0, QED=3

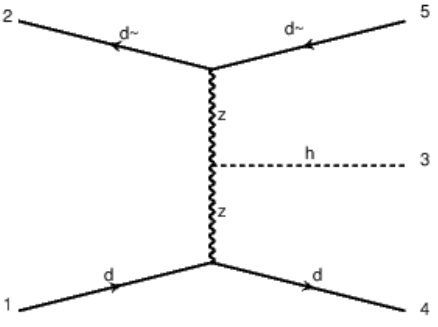

diagram 2 QCD=0, QED=3

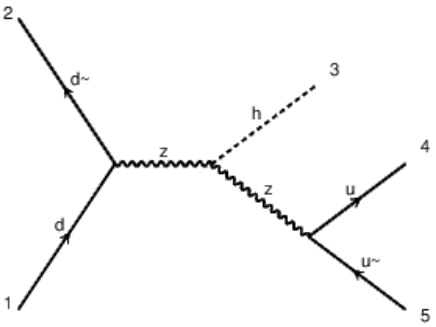

diagram 1 QCD=0, QED=3

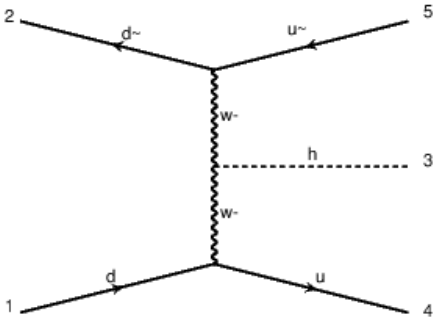

diagram 2 QCD=0, QED=3

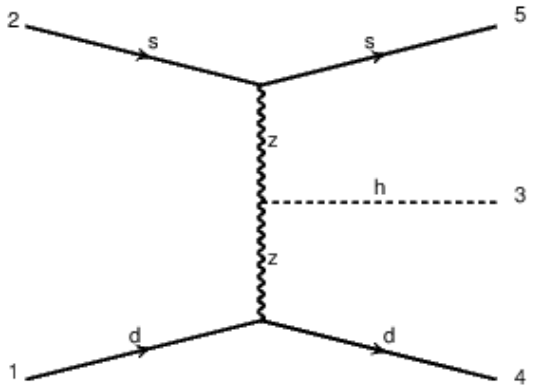

diagram 1 QCD=0, QED=3

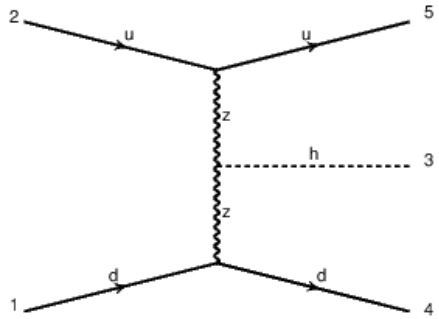

diagram 1 QCD=0, QED=3

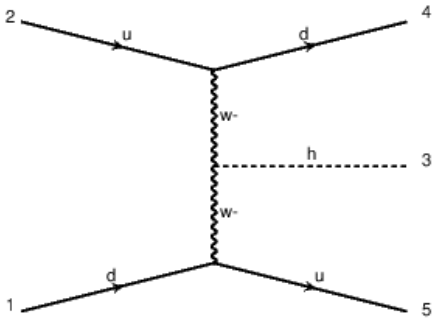

diagram 2 QCD=0, QED=3

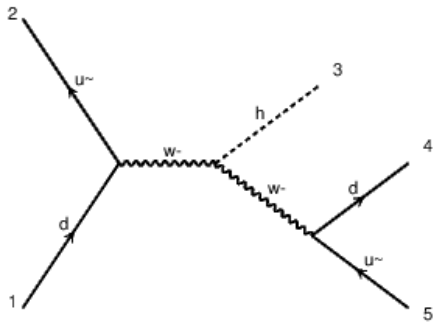

diagram 1 QCD=0, QED=3

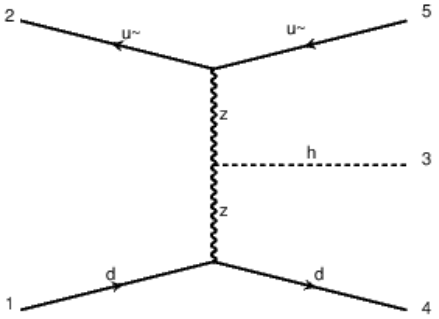

diagram 2 QCD=0, QED=3

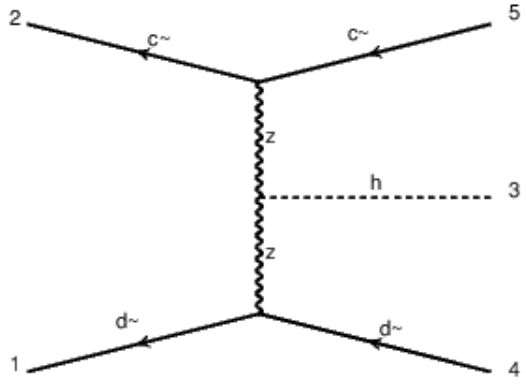

diagram 1 QCD=0, QED=3

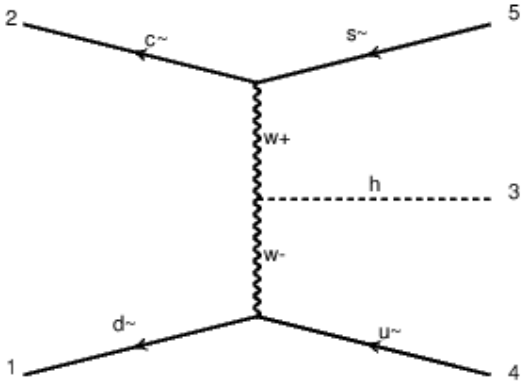

diagram 1 QCD=0, QED=3

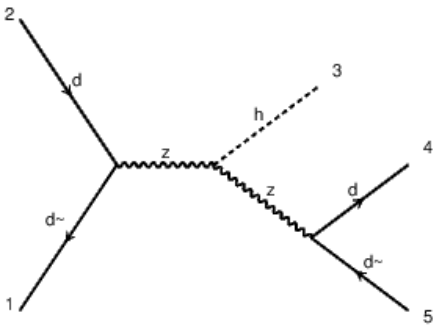

diagram 1 QCD=0, QED=3

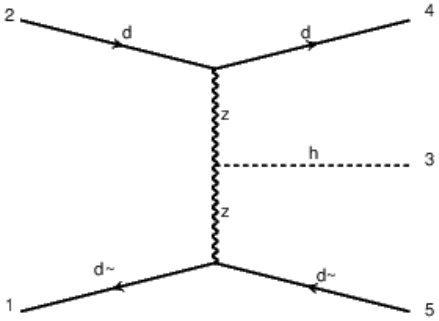

diagram 2 QCD=0, QED=3

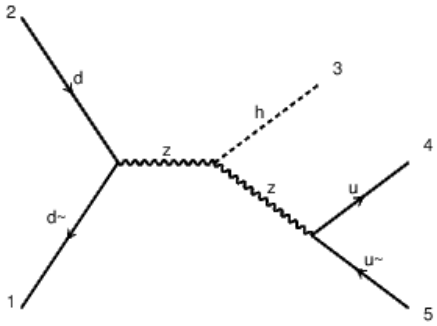

diagram 1 QCD=0, QED=3

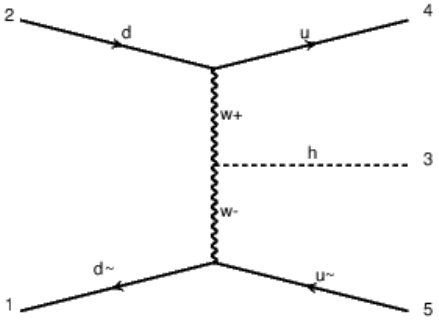

diagram 2 QCD=0, QED=3

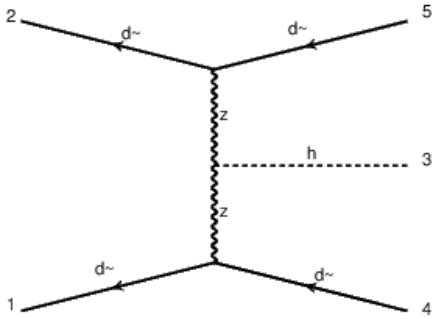

diagram 1 QCD=0, QED=3

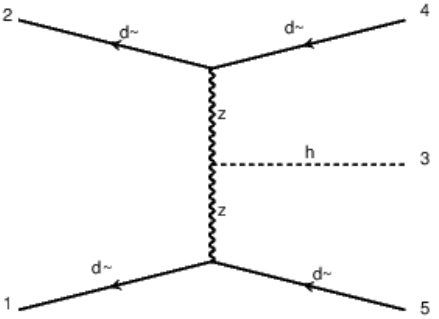

diagram 2 QCD=0, QED=3

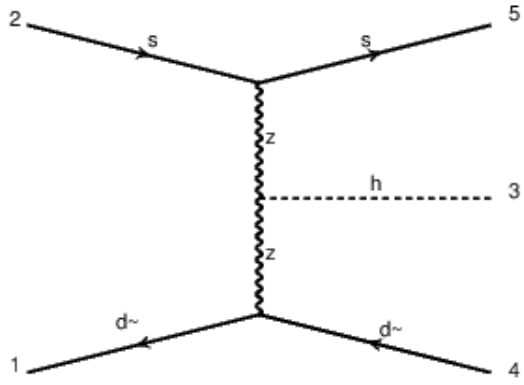

diagram 1 QCD=0, QED=3

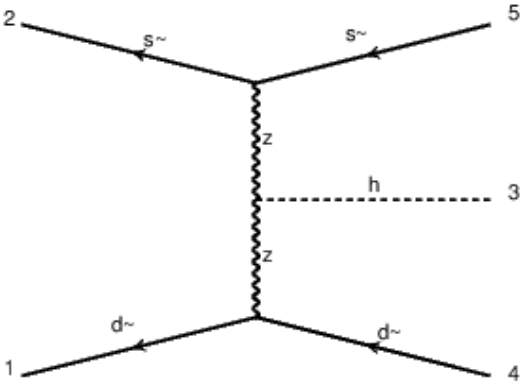

diagram 1 QCD=0, QED=3

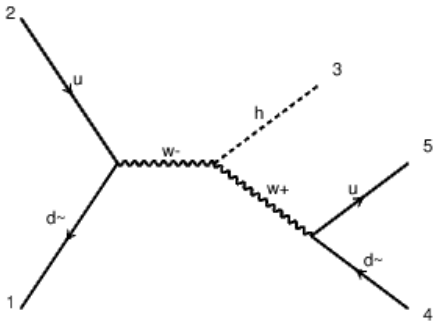

diagram 1 QCD=0, QED=3

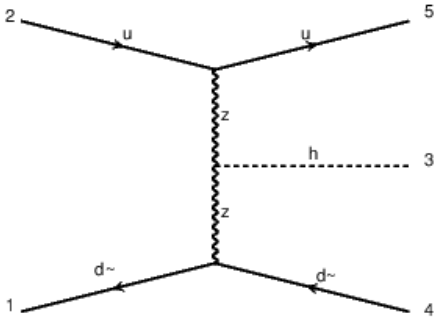

diagram 2 QCD=0, QED=3

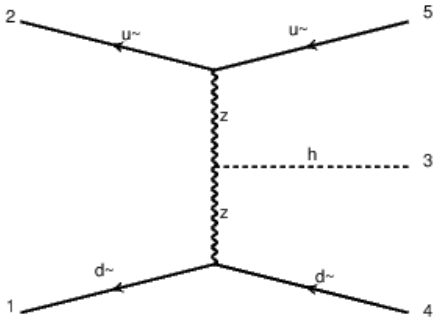

diagram 1 QCD=0, QED=3

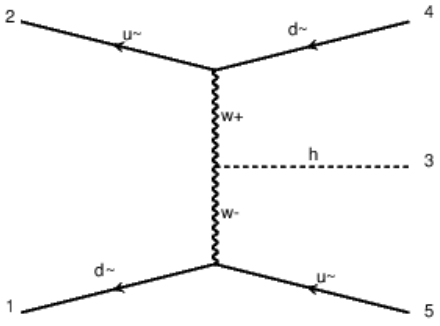

diagram 2 QCD=0, QED=3

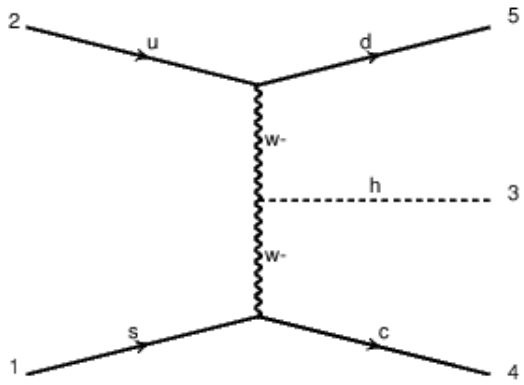

diagram 1 QCD=0, QED=3

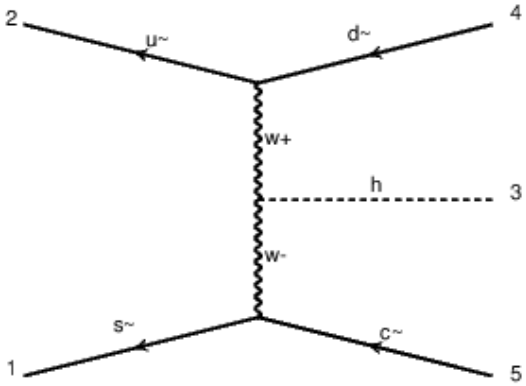

diagram 1 QCD=0, QED=3

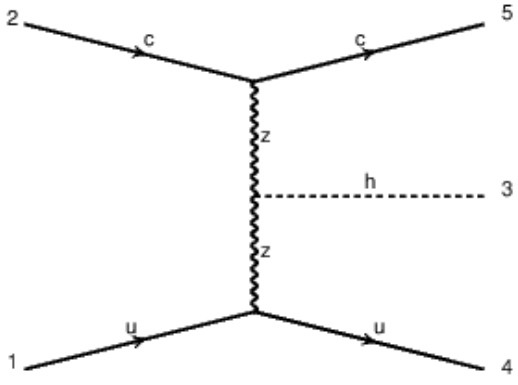

diagram 1 QCD=0, QED=3

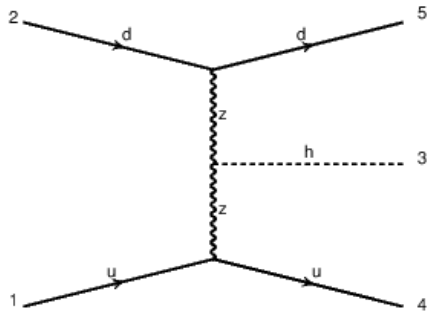

diagram 1 QCD=0, QED=3

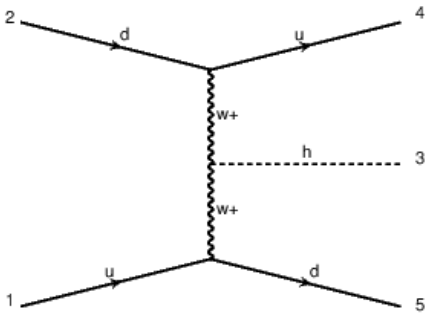

diagram 2 QCD=0, QED=3

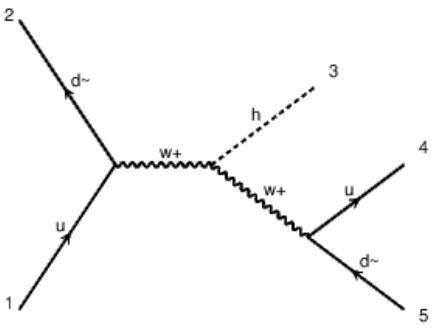

diagram 1 QCD=0, QED=3

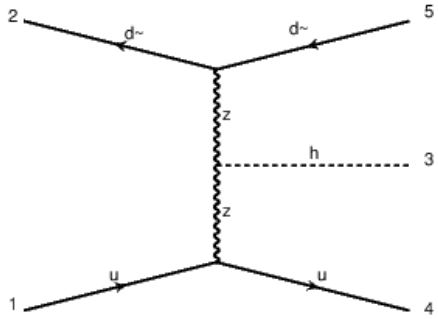

diagram 2 QCD=0, QED=3

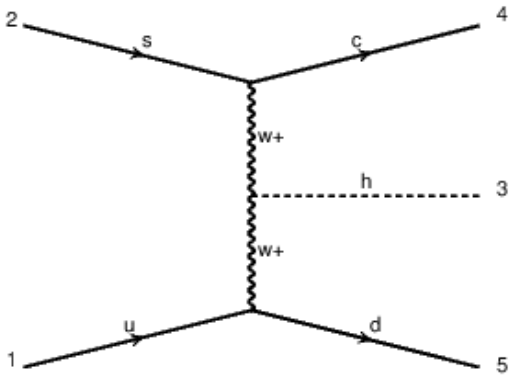

diagram 1 QCD=0, QED=3

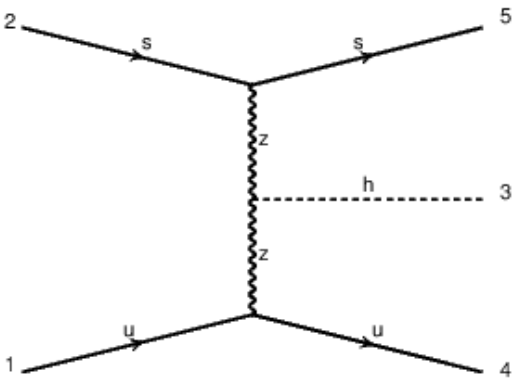

diagram 1 QCD=0, QED=3

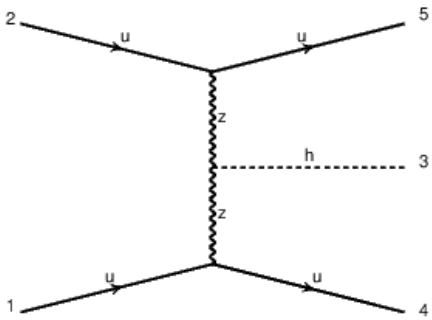

diagram 1 QCD=0, QED=3

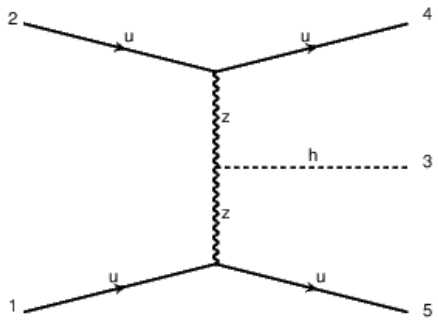

diagram 2 QCD=0, QED=3

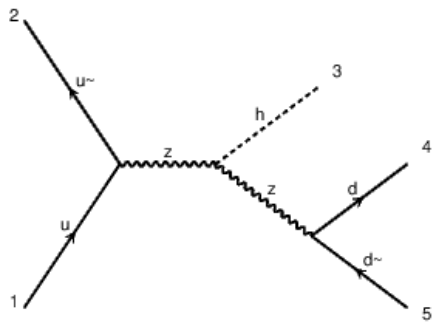

diagram 1 QCD=0, QED=3

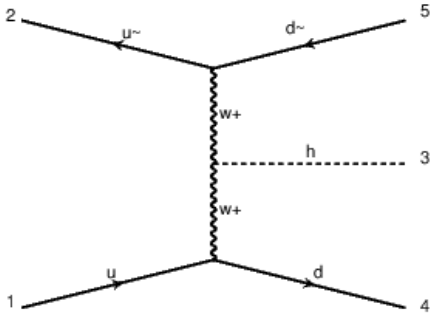

diagram 2 QCD=0, QED=3

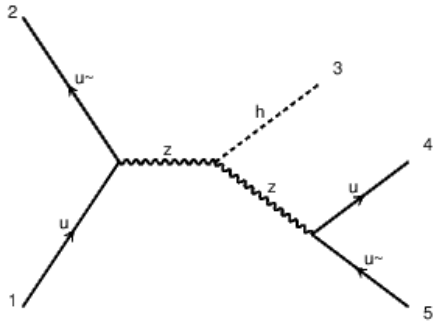

diagram 1 QCD=0, QED=3

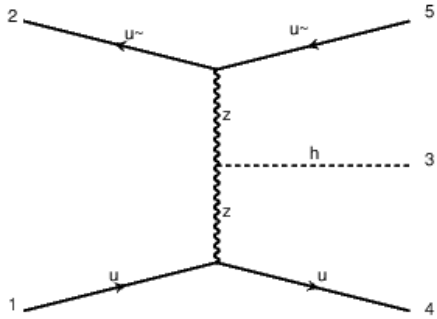

diagram 2 QCD=0, QED=3

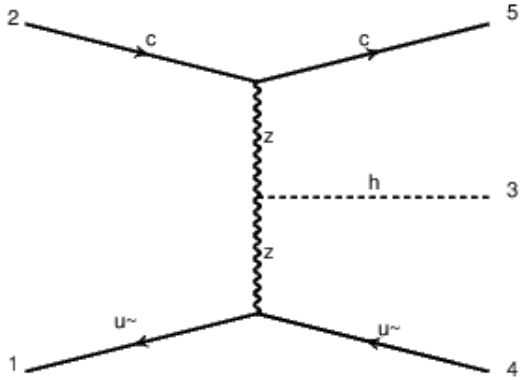

diagram 1 QCD=0, QED=3

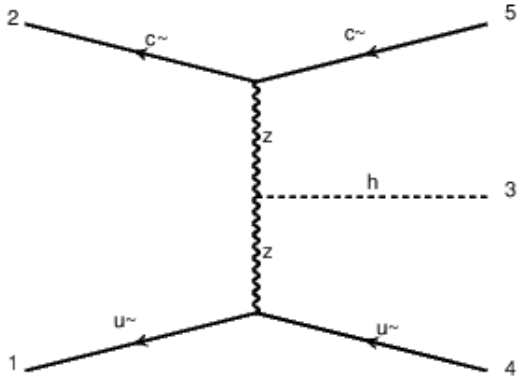

diagram 1 QCD=0, QED=3

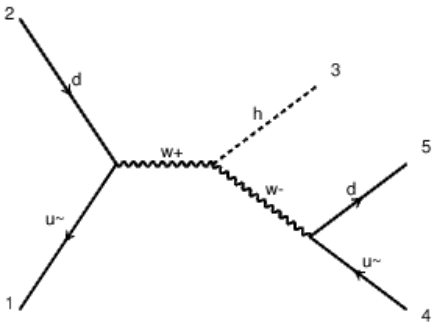

diagram 1 QCD=0, QED=3

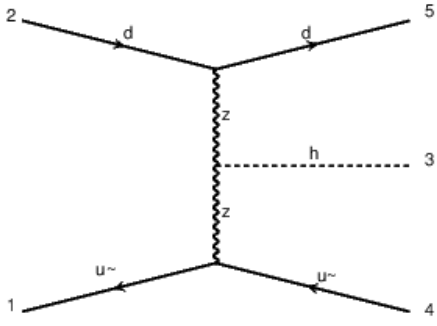

diagram 2 QCD=0, QED=3

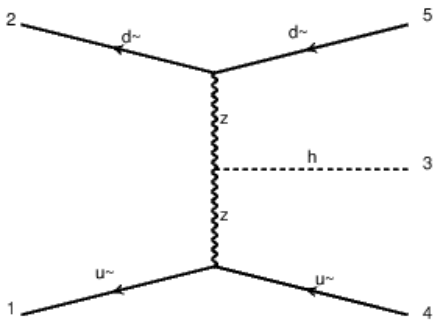

diagram 1 QCD=0, QED=3

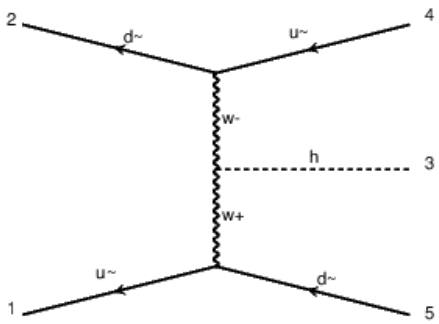

diagram 2 QCD=0, QED=3

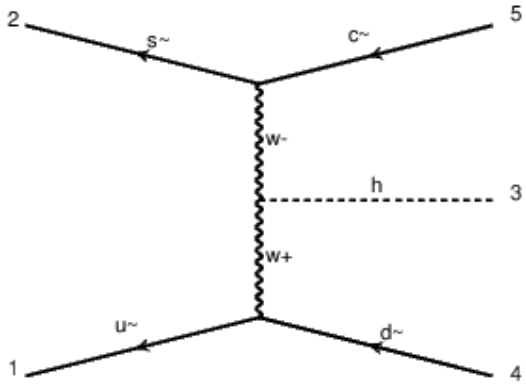

diagram 1 QCD=0, QED=3

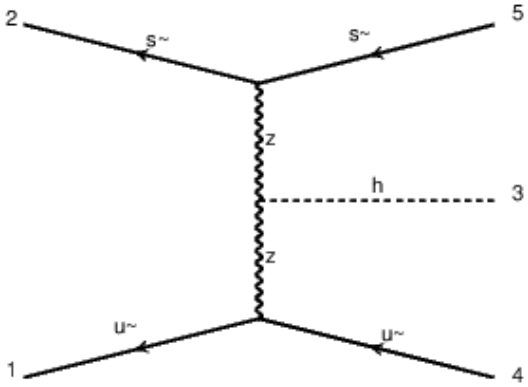

diagram 1 QCD=0, QED=3

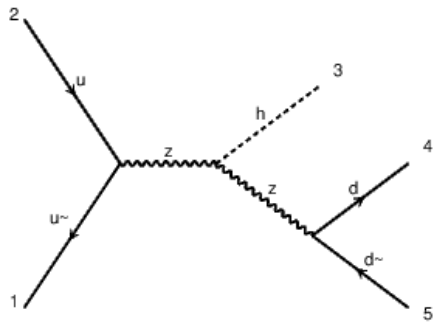

diagram 1 QCD=0, QED=3

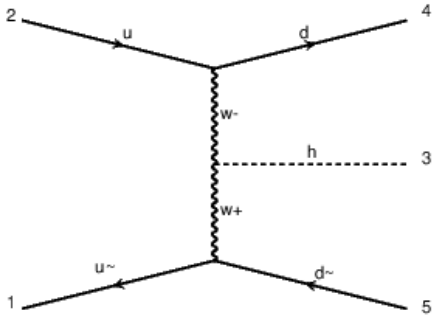

diagram 2 QCD=0, QED=3

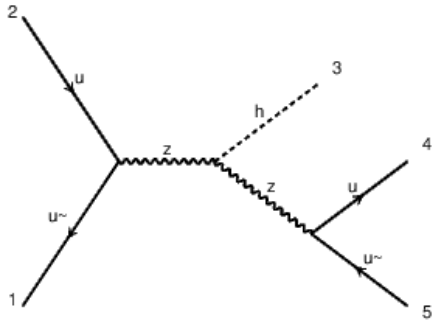

diagram 1 QCD=0, QED=3

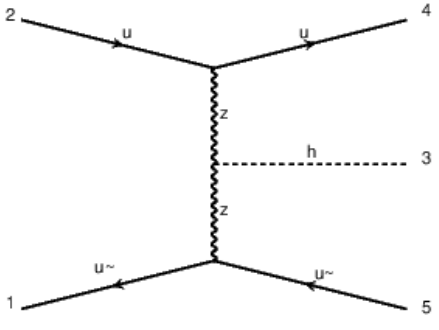

diagram 2 QCD=0, QED=3

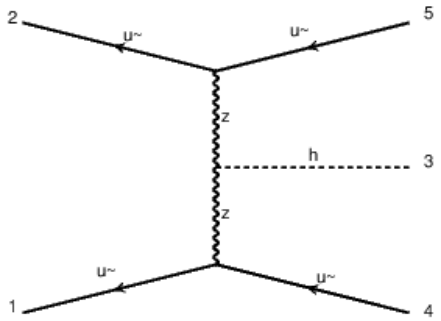

diagram 1 QCD=0, QED=3

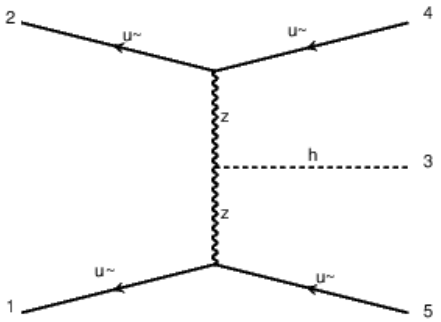

diagram 2 QCD=0, QED=3

A.5.2 $\mathcal{O}(\lambda)$ diagrams of VBF channel

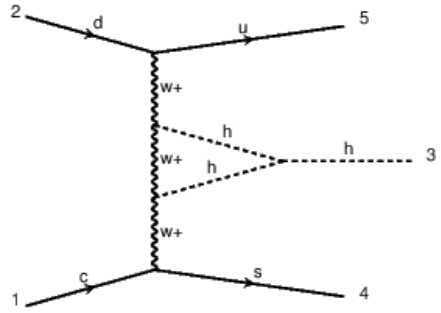

diagram 1 QCD=0, QED=5

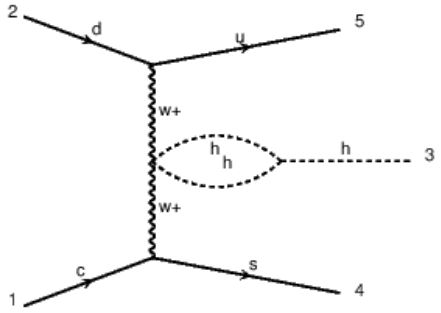

diagram 2 QCD=0, QED=5

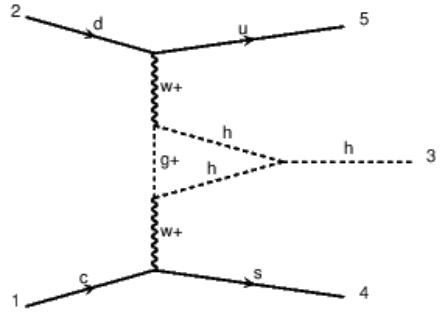

diagram 3 QCD=0, QED=5

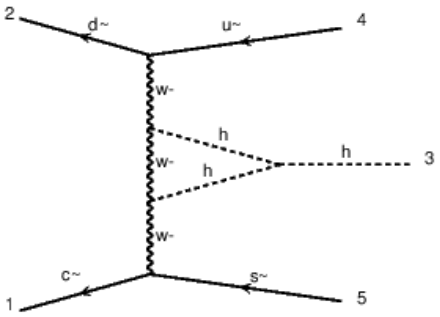

diagram 1 QCD=0, QED=5

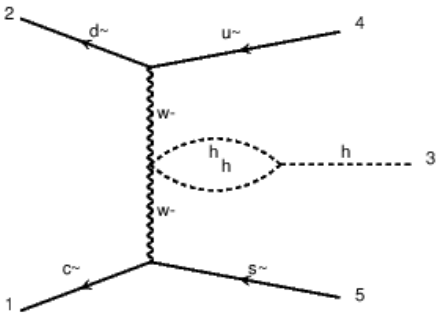

diagram 2 QCD=0, QED=5

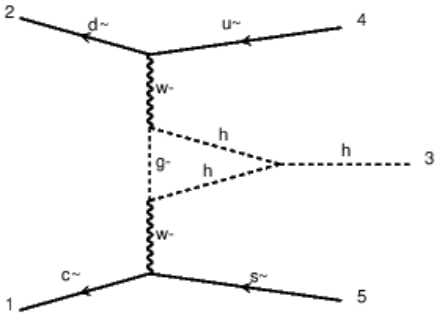

diagram 3 QCD=0, QED=5

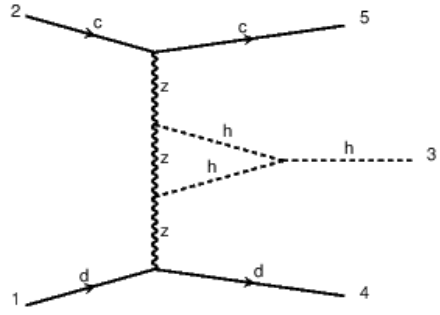

diagram 1 QCD=0, QED=5

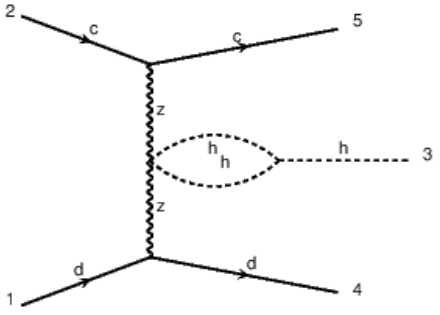

diagram 2 QCD=0, QED=5

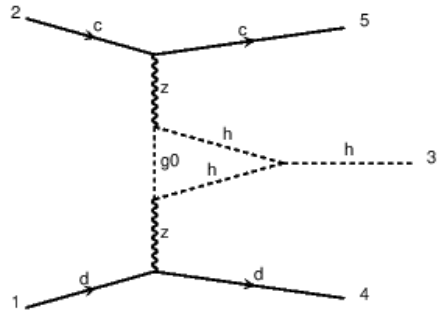

diagram 3 QCD=0, QED=5

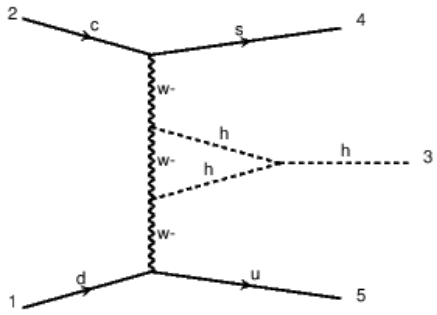

diagram 1 QCD=0, QED=5

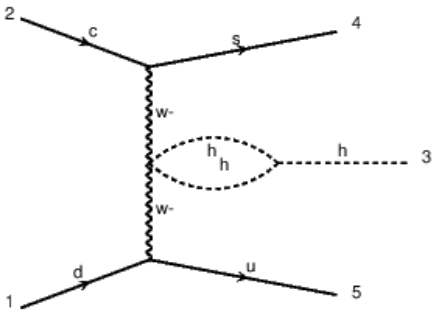

diagram 2 QCD=0, QED=5

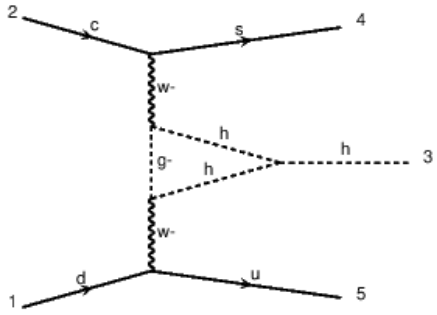

diagram 3 QCD=0, QED=5

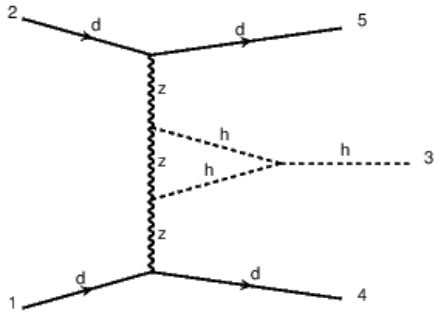

diagram 1 QCD=0, QED=5

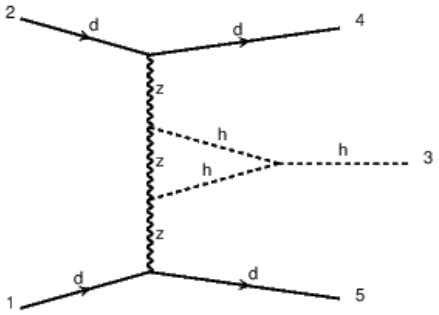

diagram 2 QCD=0, QED=5

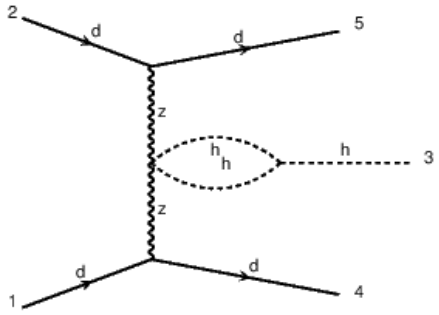

diagram 3 QCD=0, QED=5

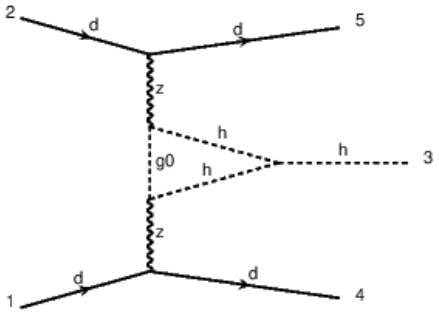

diagram 4 QCD=0, QED=5

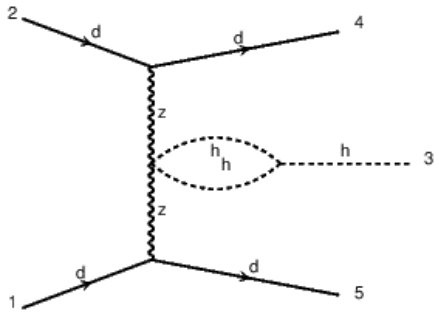

diagram 5 QCD=0, QED=5

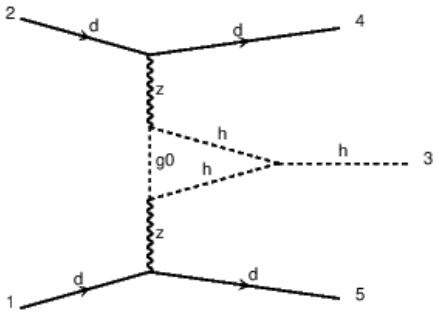

diagram 6 QCD=0, QED=5

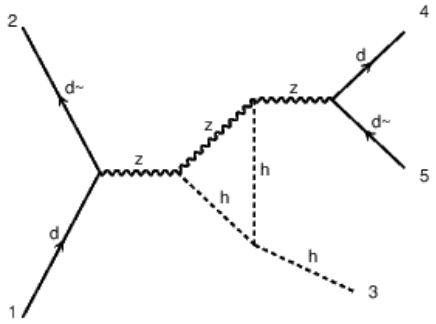

diagram 1 QCD=0, QED=5

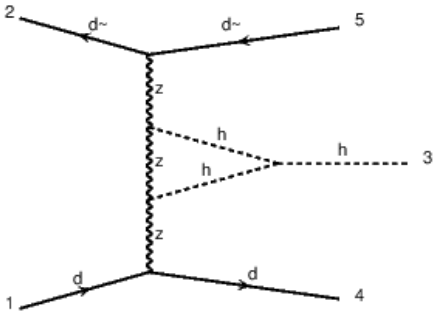

diagram 2 QCD=0, QED=5

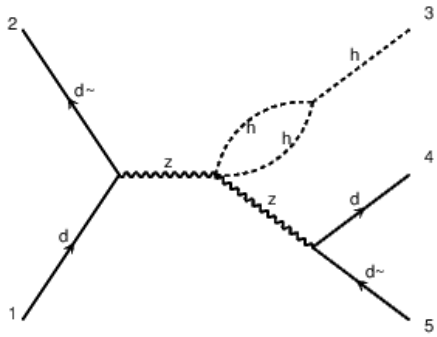

diagram 3 QCD=0, QED=5

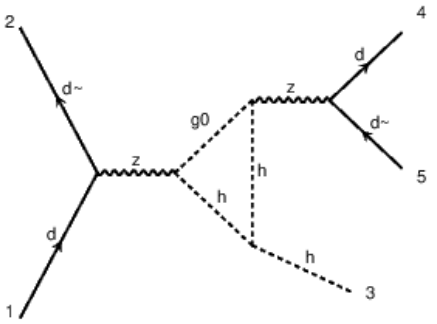

diagram 4 QCD=0, QED=5

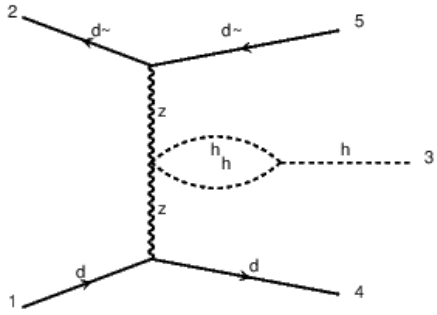

diagram 5 QCD=0, QED=5

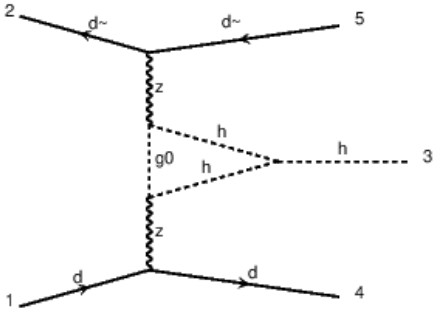

diagram 6 QCD=0, QED=5

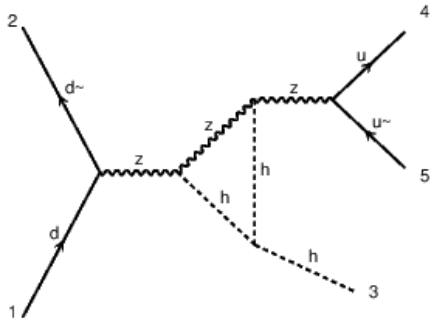

diagram 1 QCD=0, QED=5

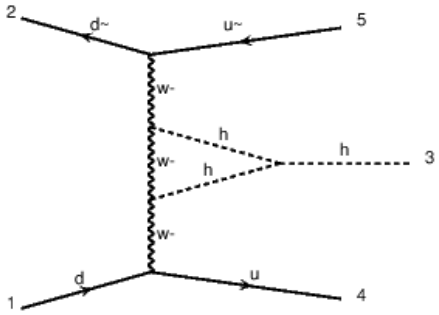

diagram 2 QCD=0, QED=5

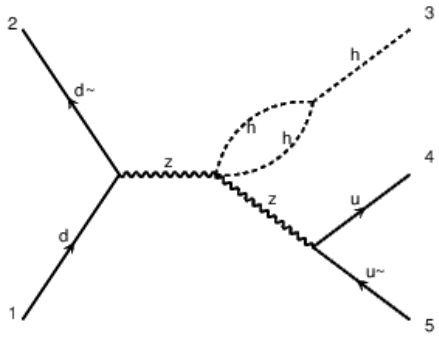

diagram 3 QCD=0, QED=5

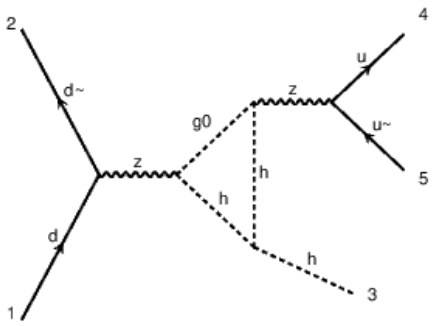

diagram 4 QCD=0, QED=5

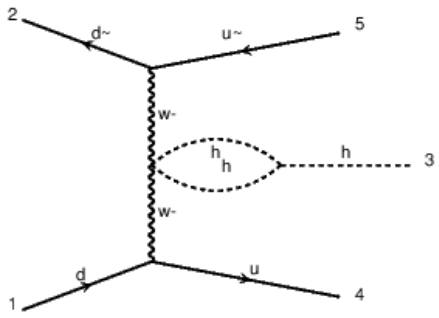

diagram 5 QCD=0, QED=5

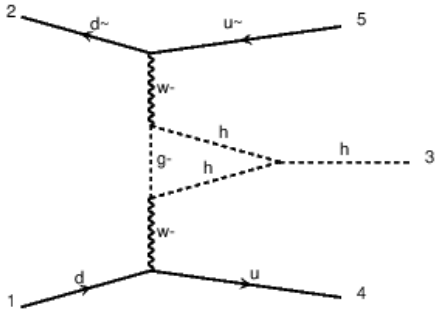

diagram 6 QCD=0, QED=5

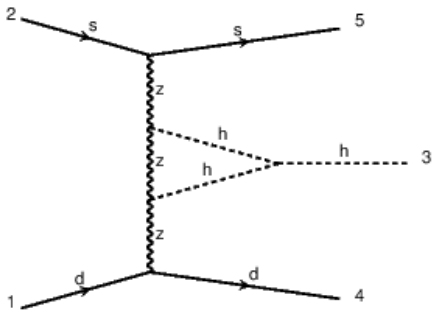

diagram 1 QCD=0, QED=5

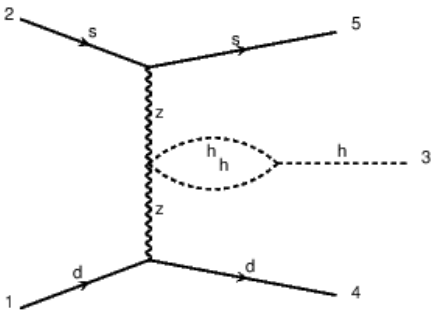

diagram 2 QCD=0, QED=5

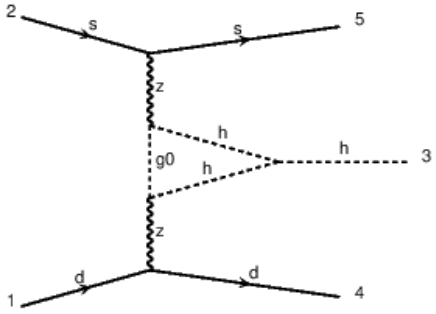

diagram 3 QCD=0, QED=5

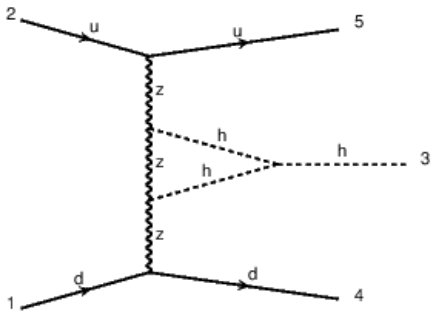

diagram 1 QCD=0, QED=5

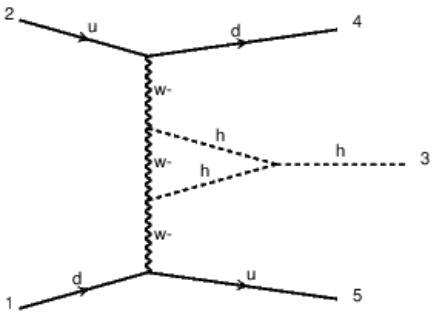

diagram 2 QCD=0, QED=5

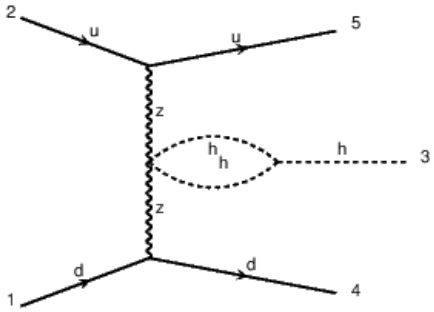

diagram 3 QCD=0, QED=5

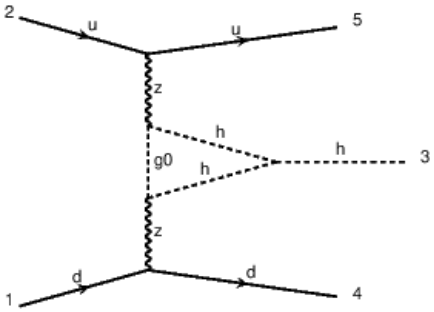

diagram 4 QCD=0, QED=5

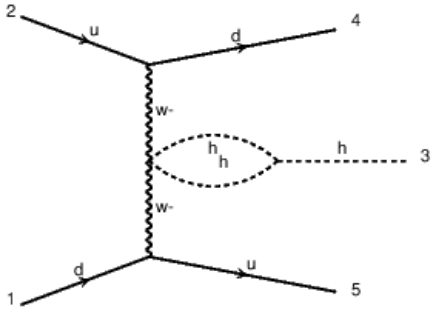

diagram 5 QCD=0, QED=5

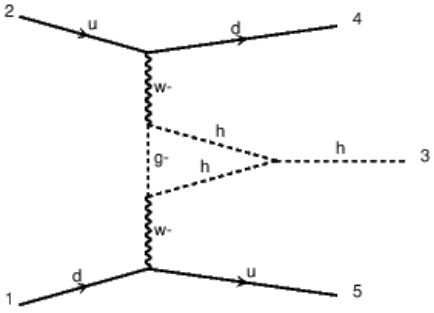

diagram 6 QCD=0, QED=5

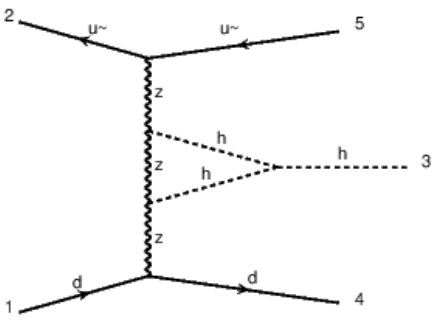

diagram 1 QCD=0, QED=5

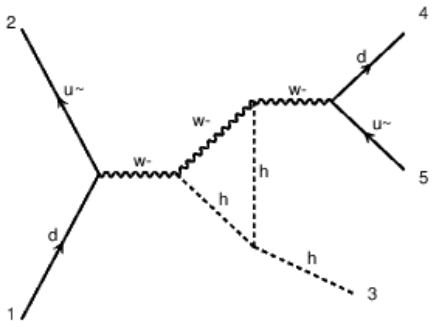

diagram 2 QCD=0, QED=5

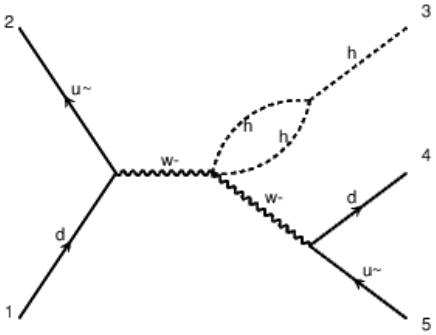

diagram 3 QCD=0, QED=5

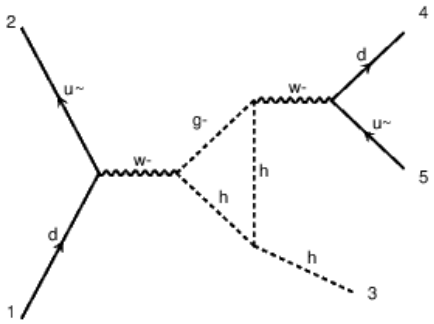

diagram 4 QCD=0, QED=5

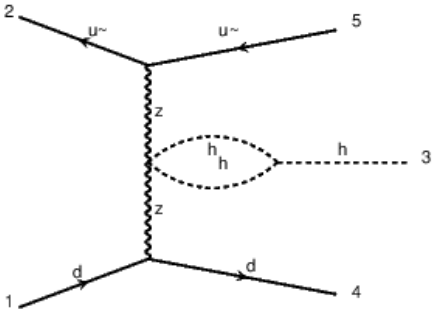

diagram 5 QCD=0, QED=5

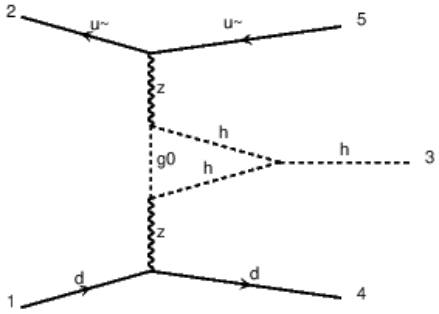

diagram 6 QCD=0, QED=5

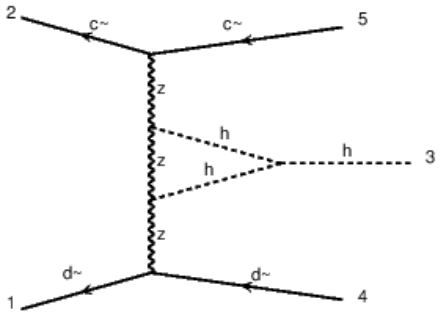

diagram 1 QCD=0, QED=5

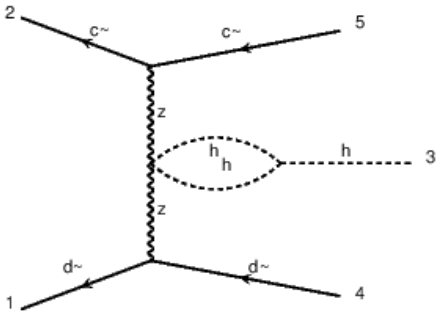

diagram 2 QCD=0, QED=5

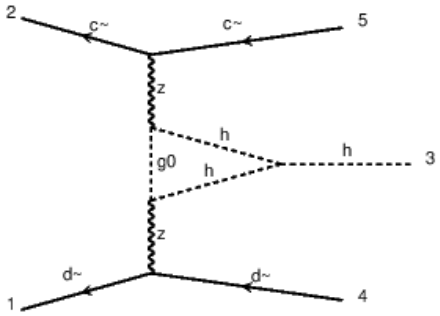

diagram 3 QCD=0, QED=5

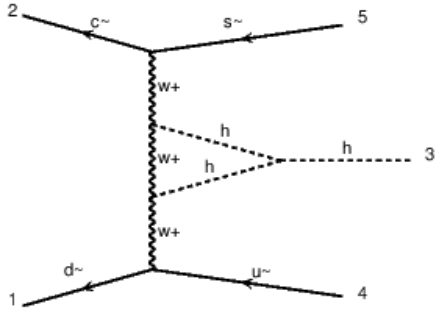

diagram 1 QCD=0, QED=5

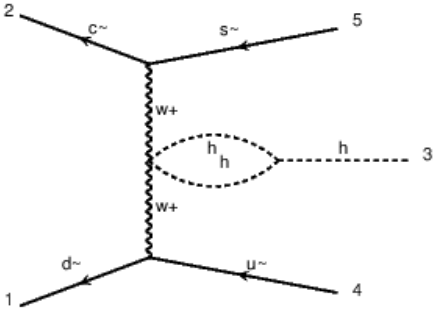

diagram 2 QCD=0, QED=5

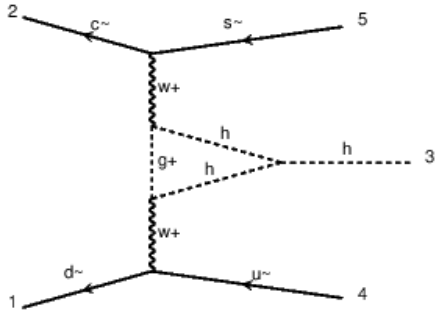

diagram 3 QCD=0, QED=5

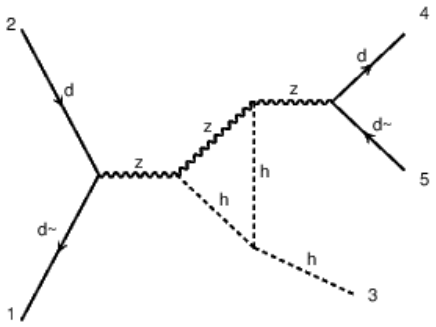

diagram 1 QCD=0, QED=5

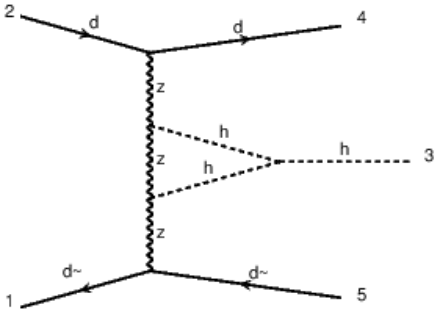

diagram 2 QCD=0, QED=5

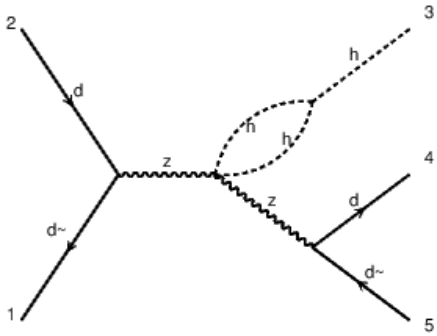

diagram 3 QCD=0, QED=5

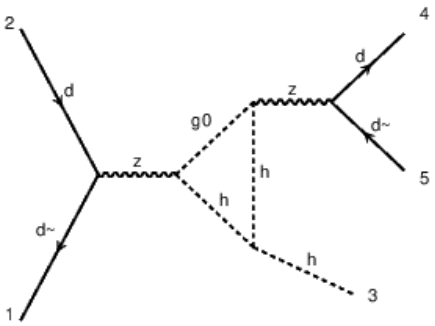

diagram 4 QCD=0, QED=5

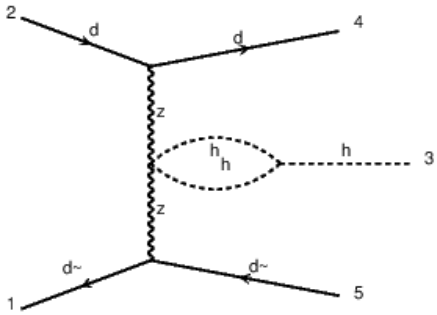

diagram 5 QCD=0, QED=5

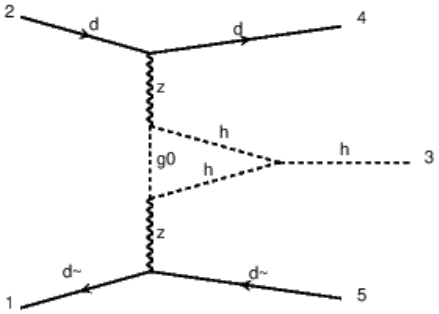

diagram 6 QCD=0, QED=5

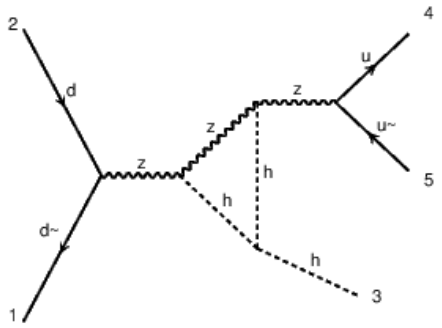

diagram 1 QCD=0, QED=5

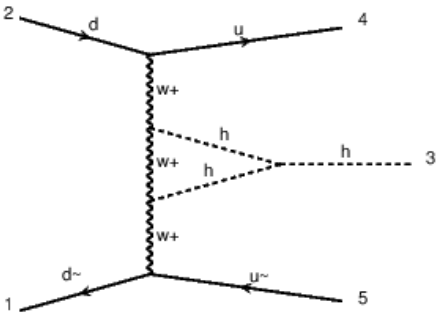

diagram 2 QCD=0, QED=5

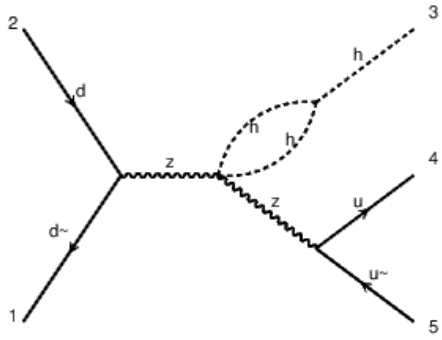

diagram 3 QCD=0, QED=5

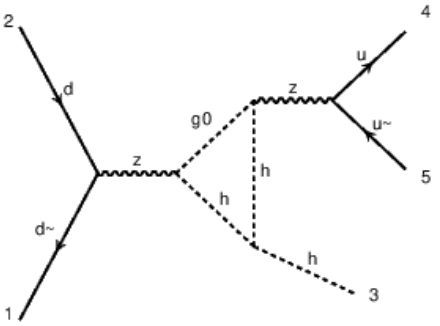

diagram 4 QCD=0, QED=5

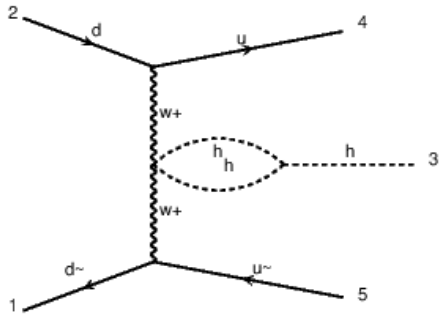

diagram 5 QCD=0, QED=5

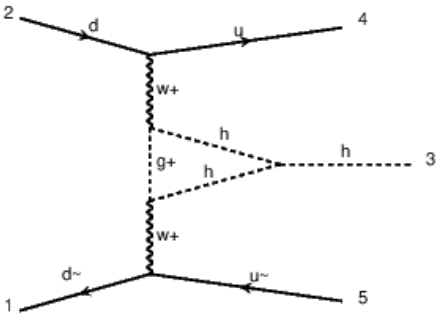

diagram 6 QCD=0, QED=5

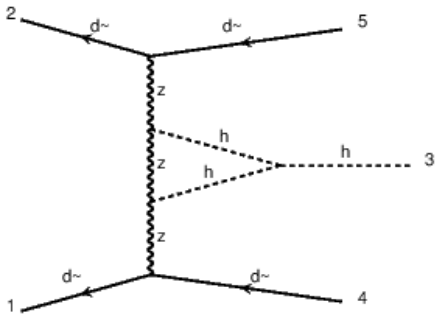

diagram 1 QCD=0, QED=5

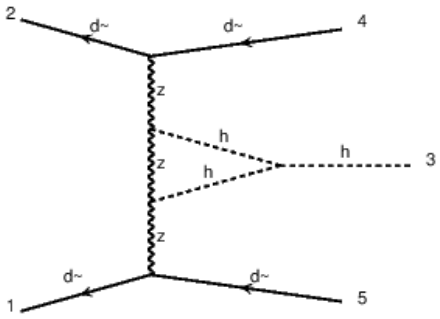

diagram 2 QCD=0, QED=5

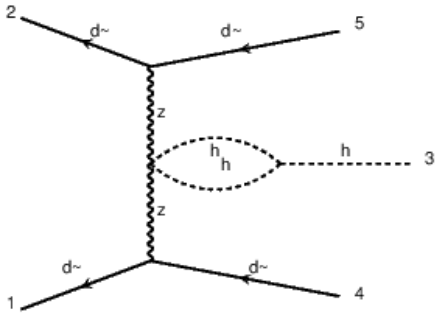

diagram 3 QCD=0, QED=5

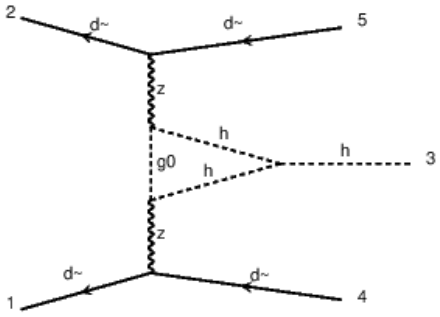

diagram 4 QCD=0, QED=5

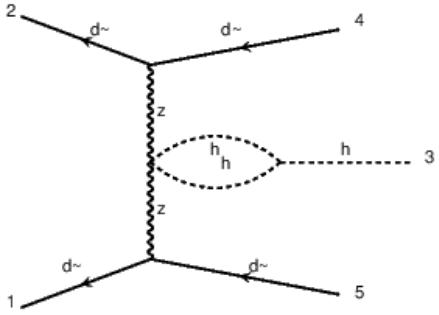

diagram 5 QCD=0, QED=5

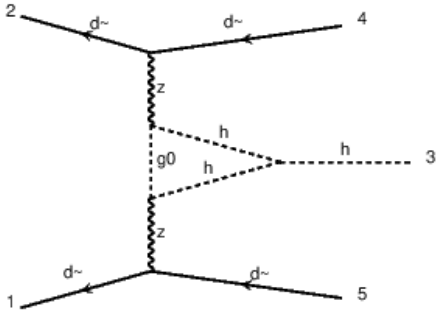

diagram 6 QCD=0, QED=5

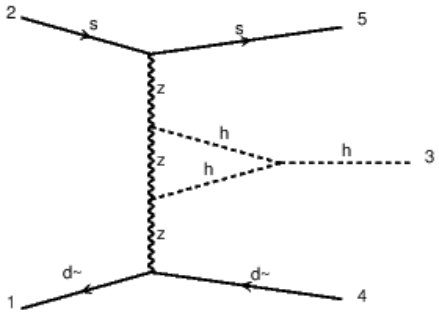

diagram 1 QCD=0, QED=5

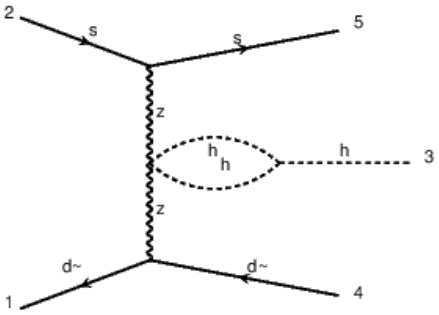

diagram 2 QCD=0, QED=5

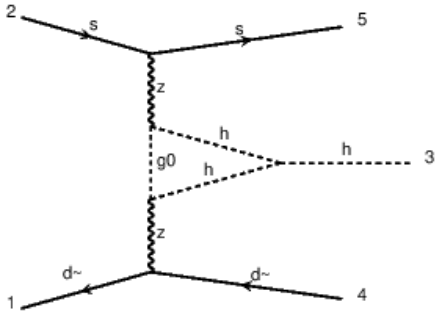

diagram 3 QCD=0, QED=5

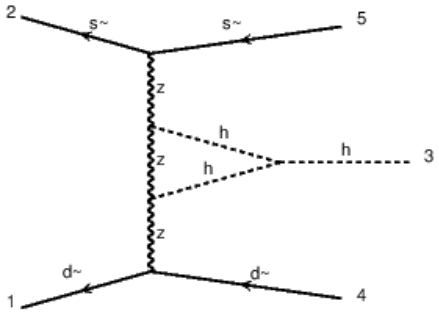

diagram 1 QCD=0, QED=5

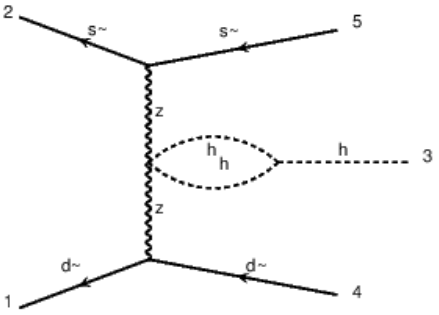

diagram 2 QCD=0, QED=5

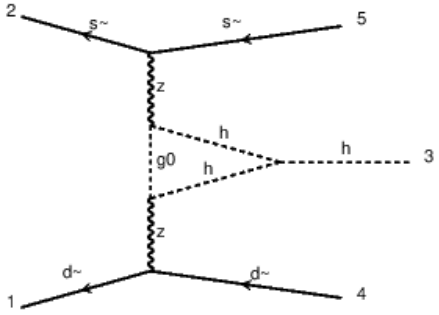

diagram 3 QCD=0, QED=5

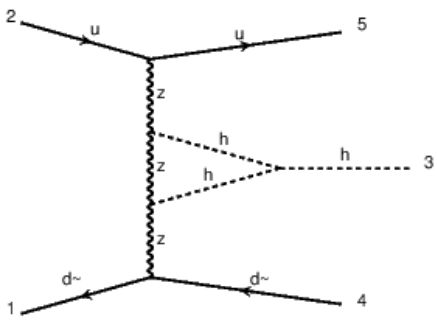

diagram 1 QCD=0, QED=5

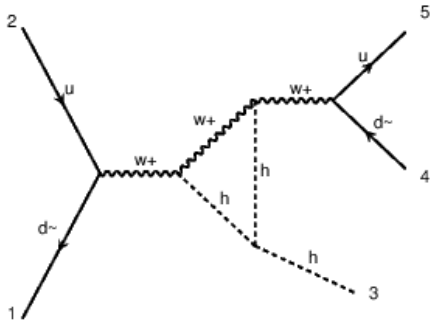

diagram 2 QCD=0, QED=5

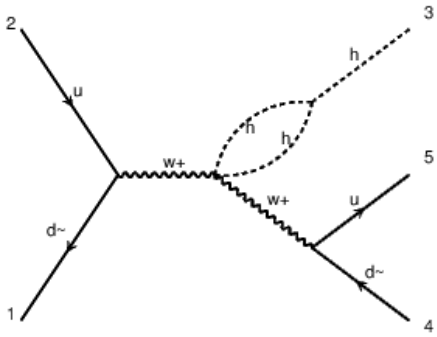

diagram 3 QCD=0, QED=5

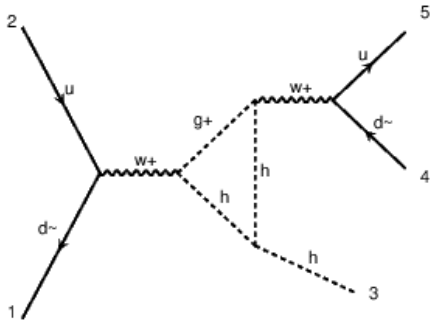

diagram 4 QCD=0, QED=5

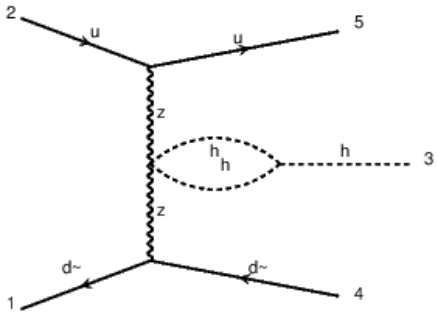

diagram 5 QCD=0, QED=5

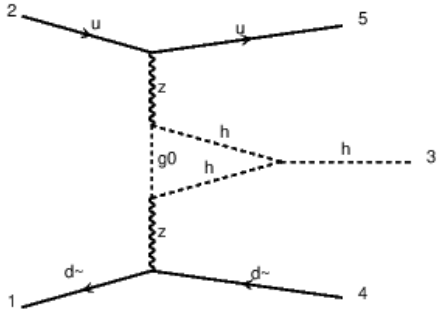

diagram 6 QCD=0, QED=5

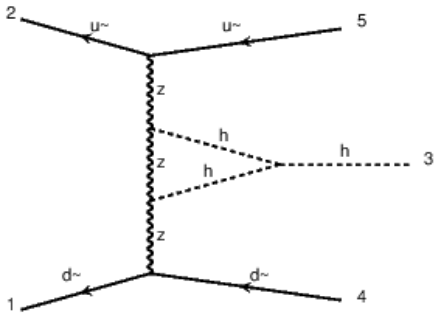

diagram 1 QCD=0, QED=5

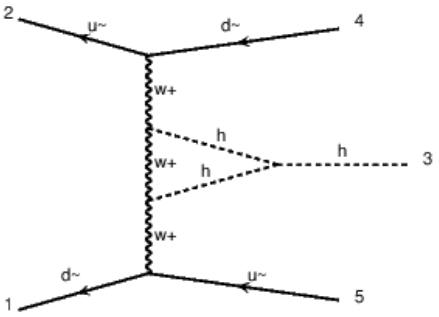

diagram 2 QCD=0, QED=5

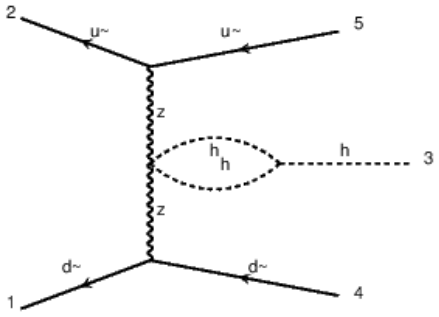

diagram 3 QCD=0, QED=5

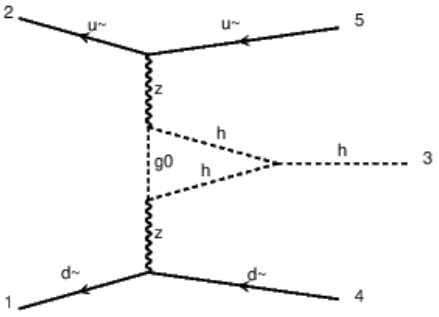

diagram 4 QCD=0, QED=5

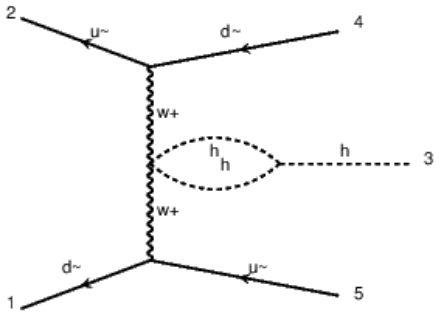

diagram 5 QCD=0, QED=5

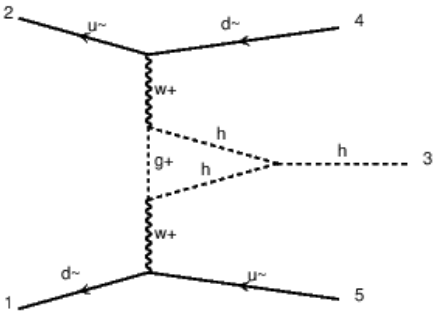

diagram 6 QCD=0, QED=5

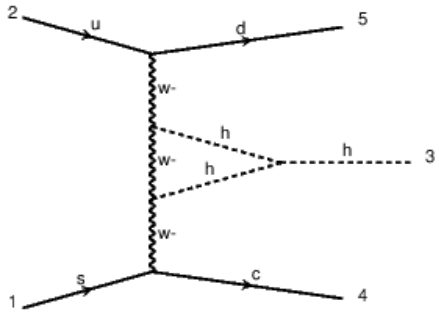

diagram 1 QCD=0, QED=5

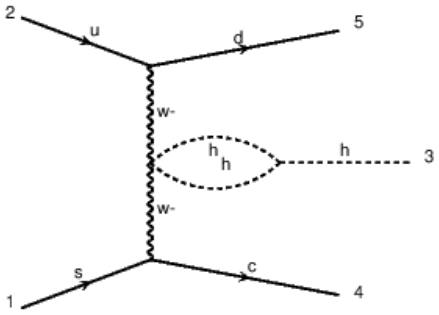

diagram 2 QCD=0, QED=5

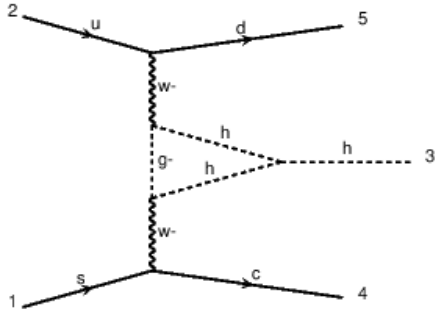

diagram 3 QCD=0, QED=5

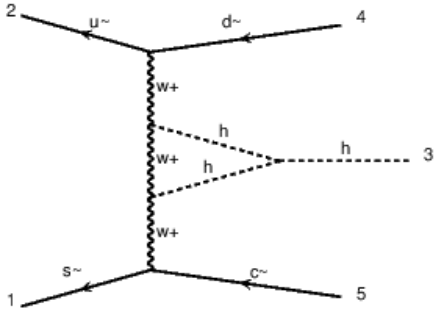

diagram 1 QCD=0, QED=5

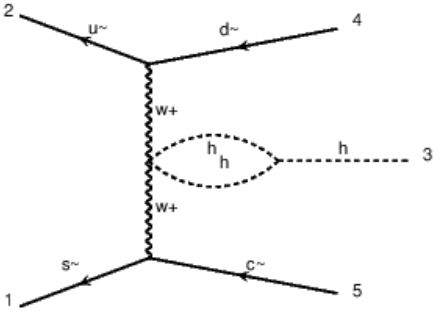

diagram 2 QCD=0, QED=5

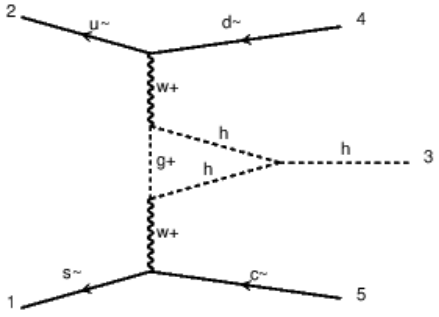

diagram 3 QCD=0, QED=5

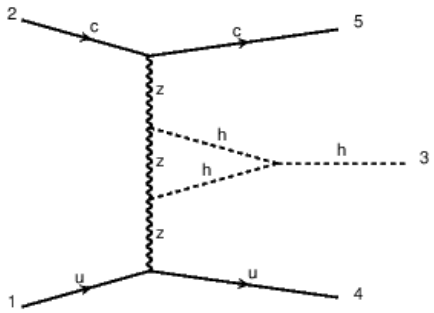

diagram 1 QCD=0, QED=5

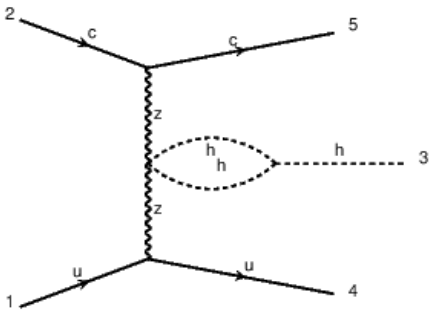

diagram 2 QCD=0, QED=5

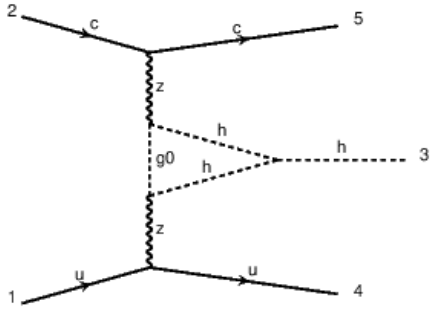

diagram 3 QCD=0, QED=5

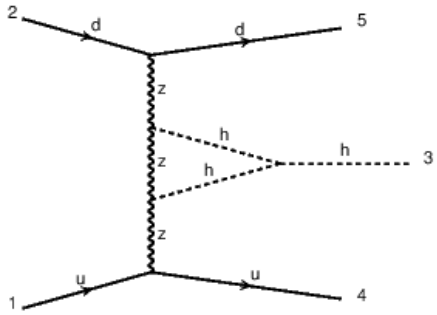

diagram 1 QCD=0, QED=5

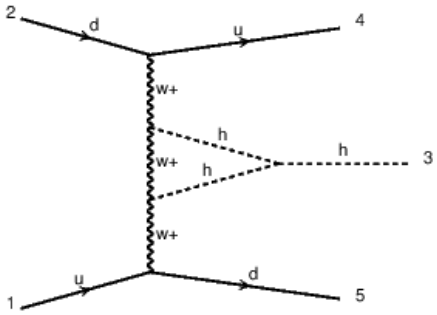

diagram 2 QCD=0, QED=5

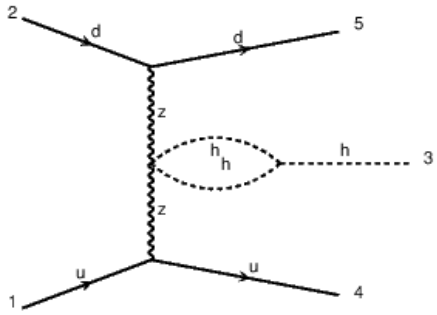

diagram 3 QCD=0, QED=5

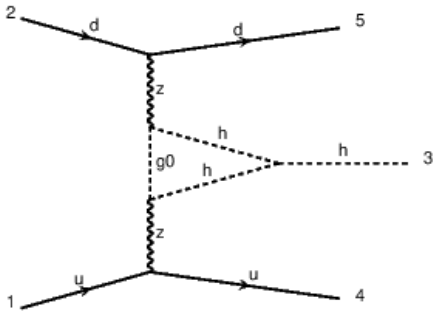

diagram 4 QCD=0, QED=5

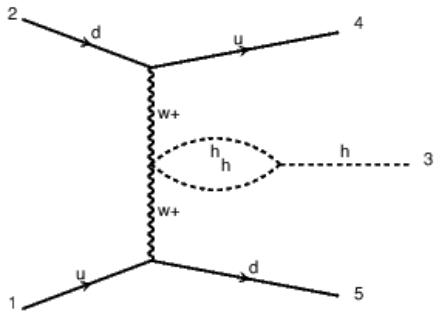

diagram 5 QCD=0, QED=5

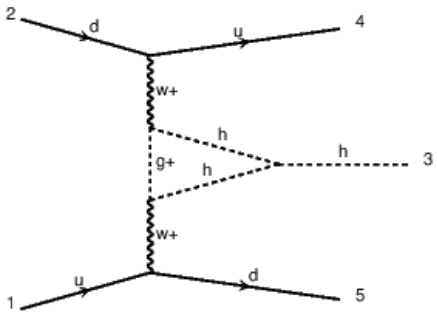

diagram 6 QCD=0, QED=5

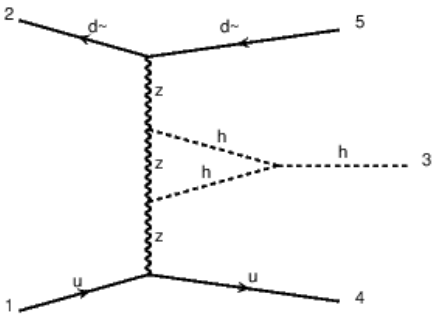

diagram 1 QCD=0, QED=5

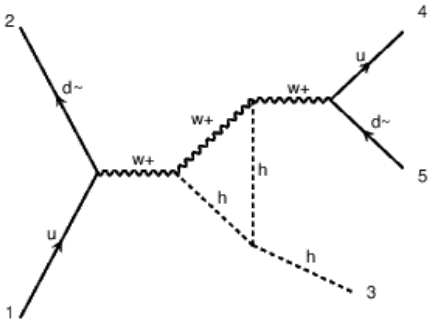

diagram 2 QCD=0, QED=5

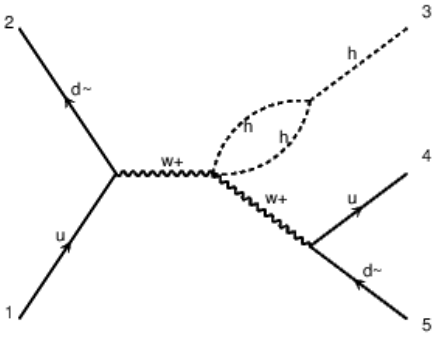

diagram 3 QCD=0, QED=5

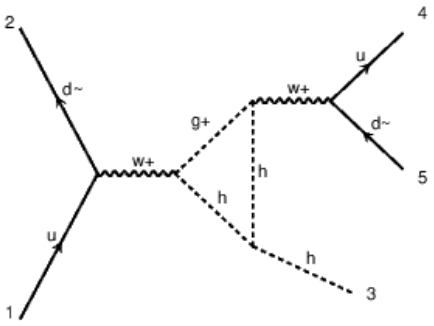

diagram 4 QCD=0, QED=5

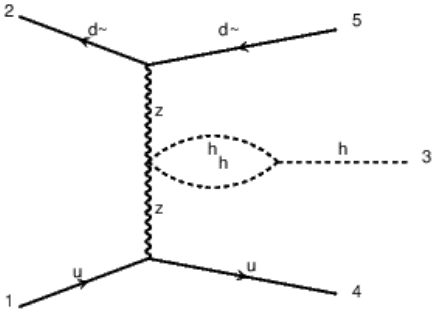

diagram 5 QCD=0, QED=5

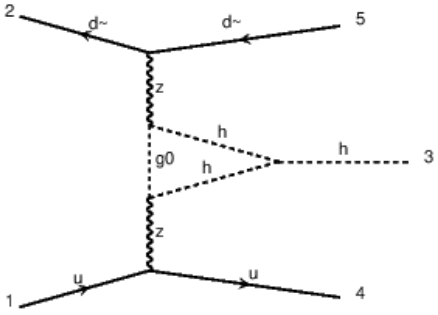

diagram 6 QCD=0, QED=5

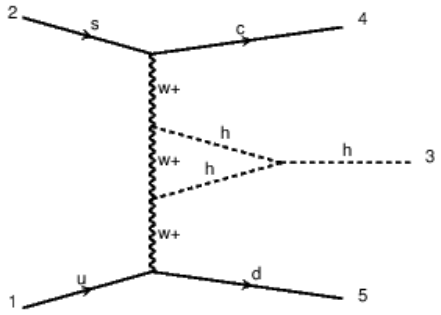

diagram 1 QCD=0, QED=5

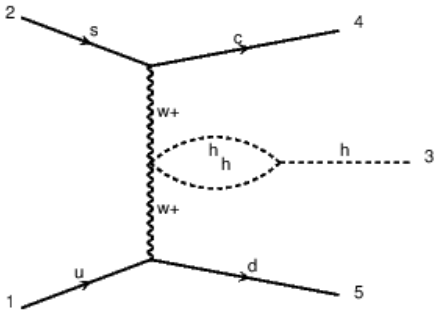

diagram 2 QCD=0, QED=5

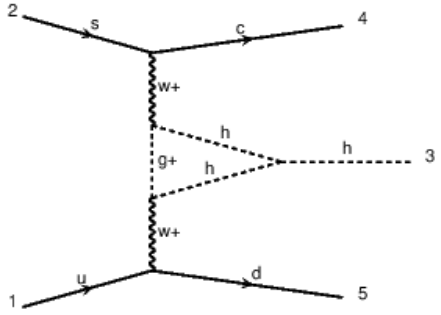

diagram 3 QCD=0, QED=5

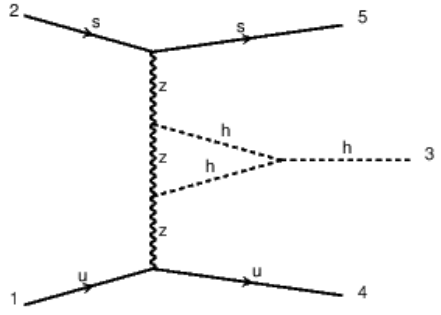

diagram 1 QCD=0, QED=5

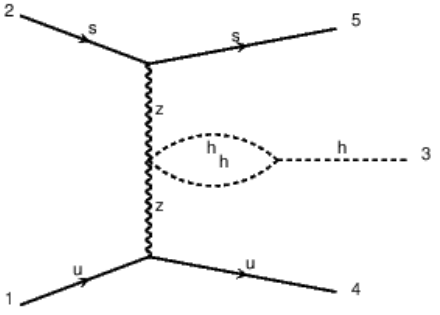

diagram 2 QCD=0, QED=5

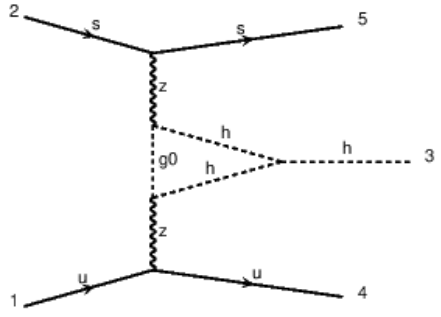

diagram 3 QCD=0, QED=5

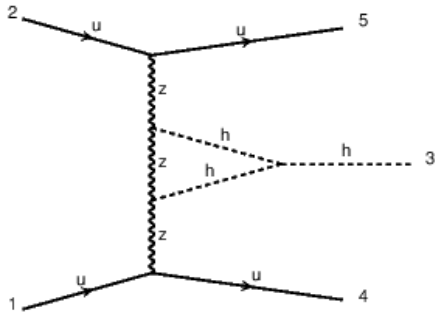

diagram 1 QCD=0, QED=5

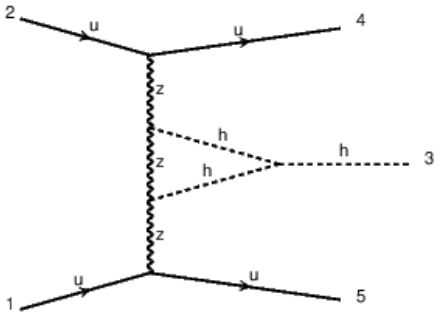

diagram 2 QCD=0, QED=5

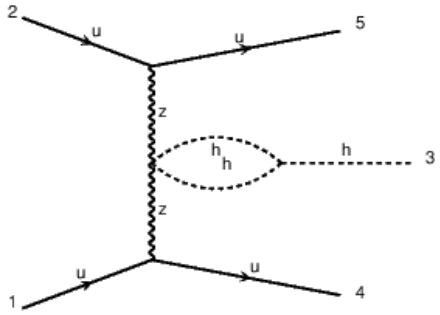

diagram 3 QCD=0, QED=5

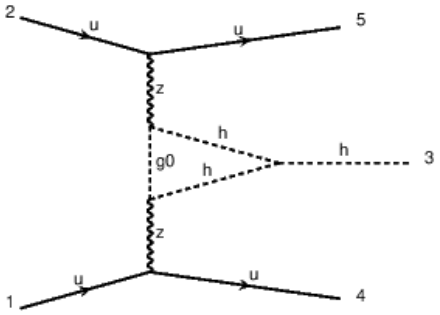

diagram 4 QCD=0, QED=5

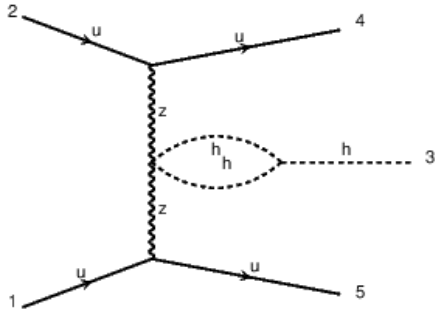

diagram 5 QCD=0, QED=5

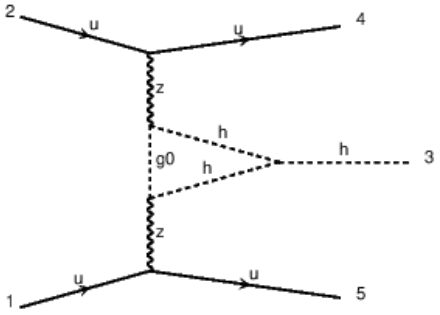

diagram 6 QCD=0, QED=5

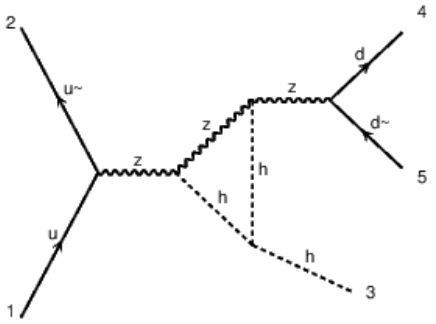

diagram 1 QCD=0, QED=5

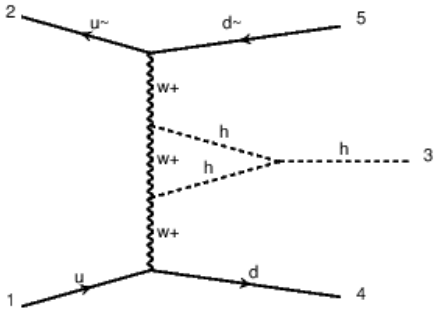

diagram 2 QCD=0, QED=5

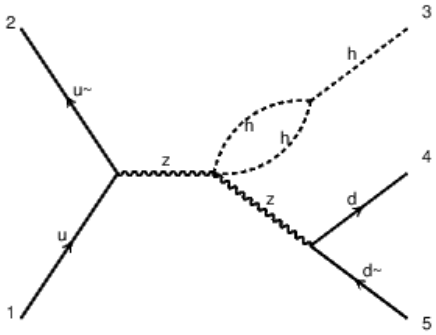

diagram 3 QCD=0, QED=5

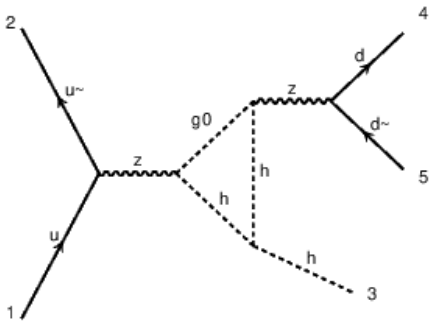

diagram 4 QCD=0, QED=5

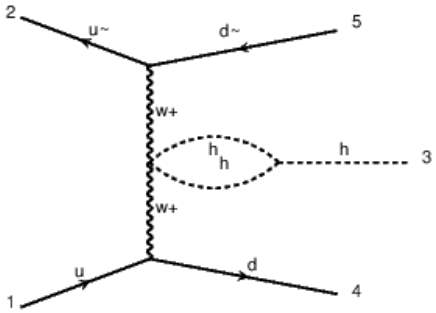

diagram 5 QCD=0, QED=5

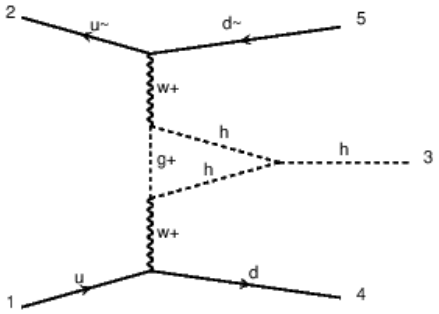

diagram 6 QCD=0, QED=5

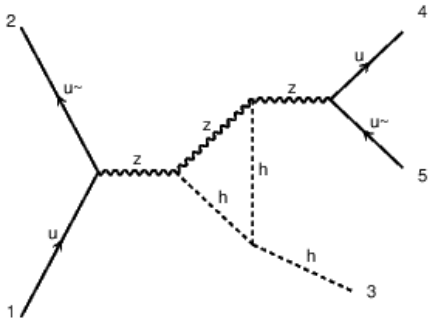

diagram 1 QCD=0, QED=5

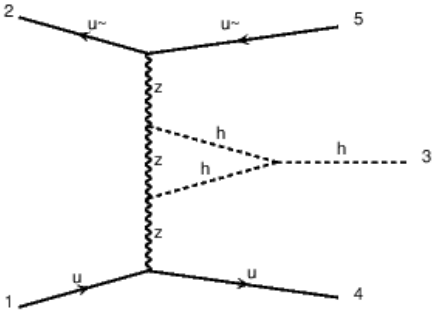

diagram 2 QCD=0, QED=5

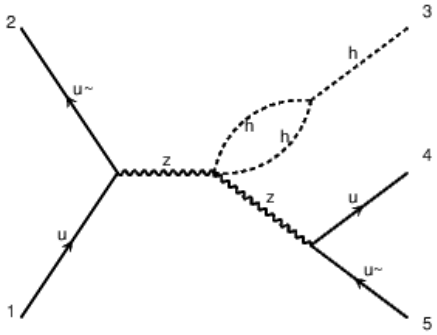

diagram 3 QCD=0, QED=5

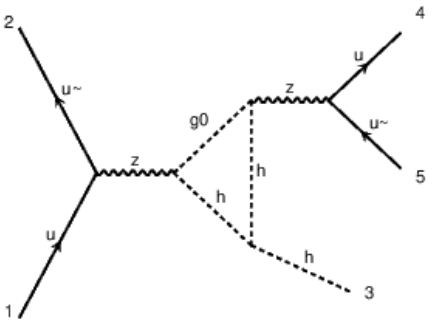

diagram 4 QCD=0, QED=5

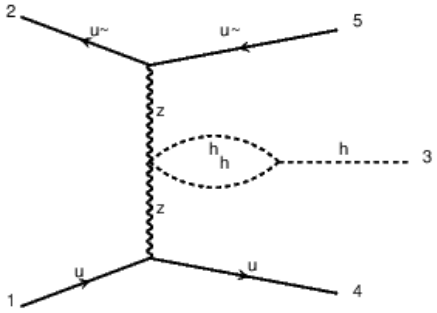

diagram 5 QCD=0, QED=5

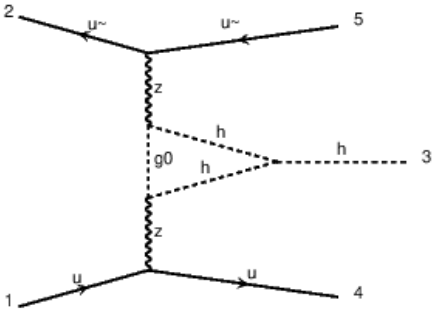

diagram 6 QCD=0, QED=5

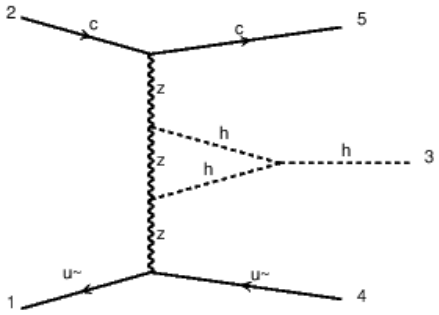

diagram 1 QCD=0, QED=5

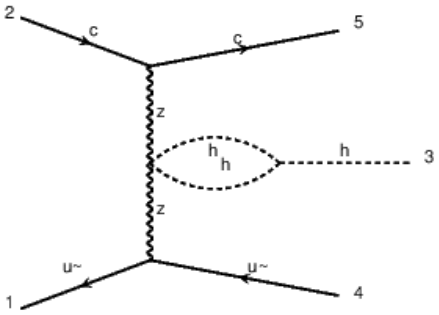

diagram 2 QCD=0, QED=5

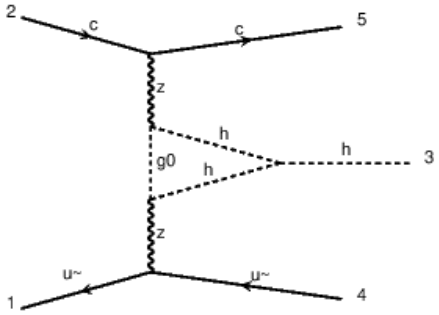

diagram 3 QCD=0, QED=5

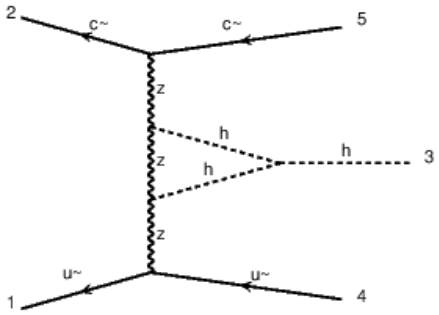

diagram 1 QCD=0, QED=5

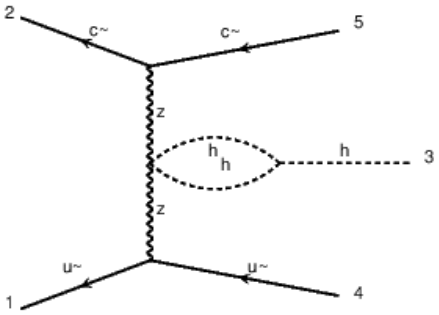

diagram 2 QCD=0, QED=5

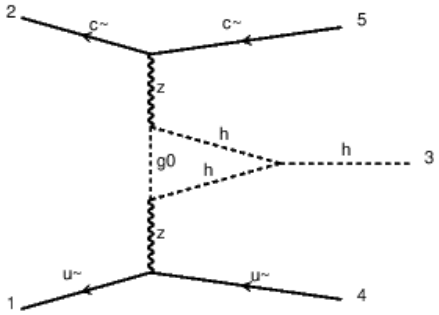

diagram 3 QCD=0, QED=5

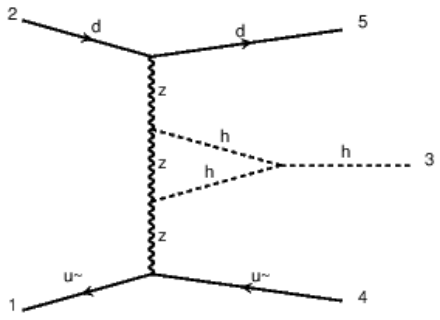

diagram 1 QCD=0, QED=5

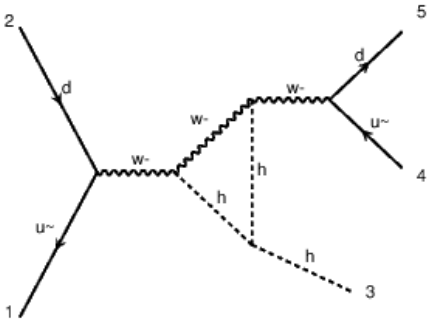

diagram 2 QCD=0, QED=5

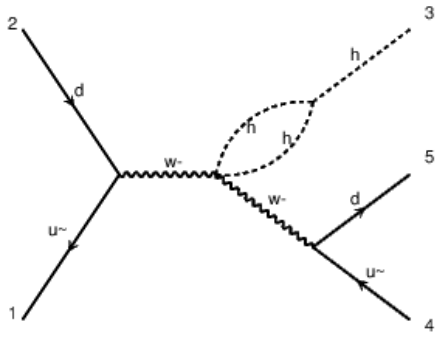

diagram 3 QCD=0, QED=5

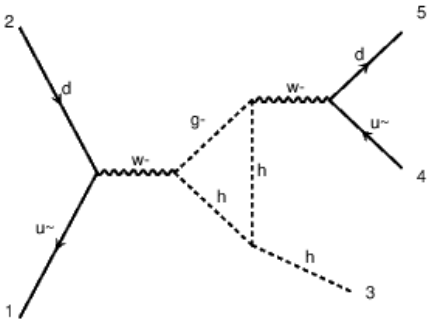

diagram 4 QCD=0, QED=5

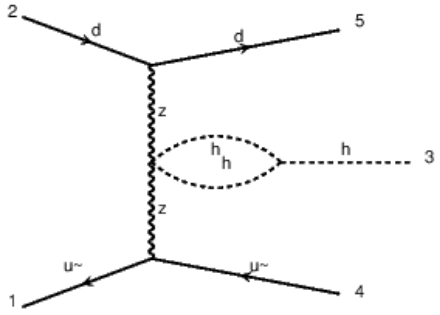

diagram 5 QCD=0, QED=5

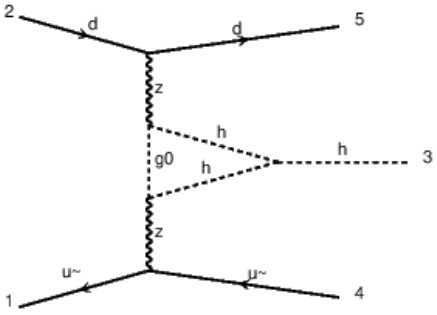

diagram 6 QCD=0, QED=5

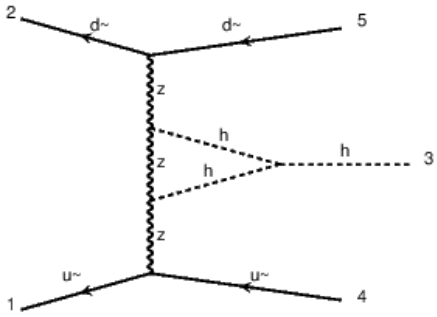

diagram 1 QCD=0, QED=5

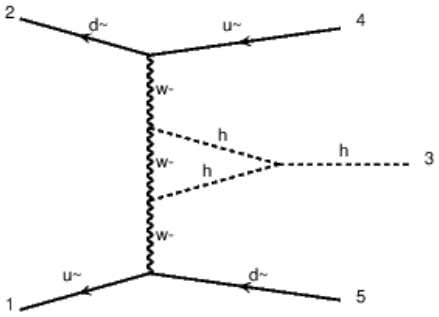

diagram 2 QCD=0, QED=5

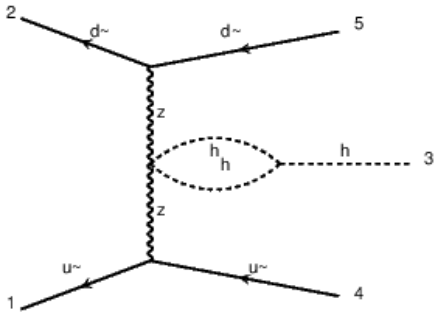

diagram 3 QCD=0, QED=5

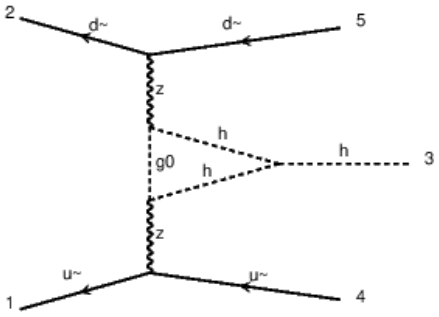

diagram 4 QCD=0, QED=5

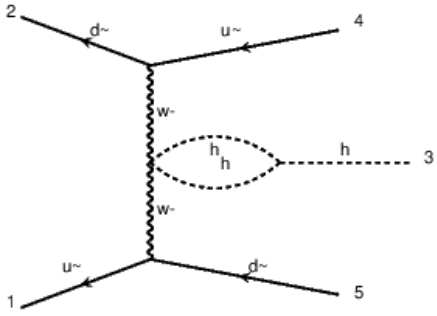

diagram 5 QCD=0, QED=5

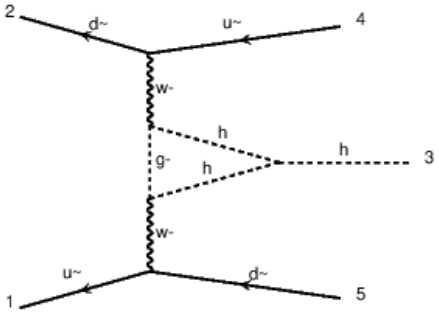

diagram 6 QCD=0, QED=5

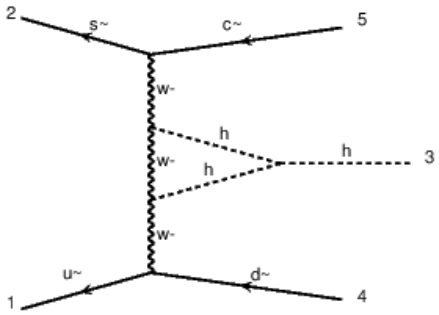

diagram 1 QCD=0, QED=5

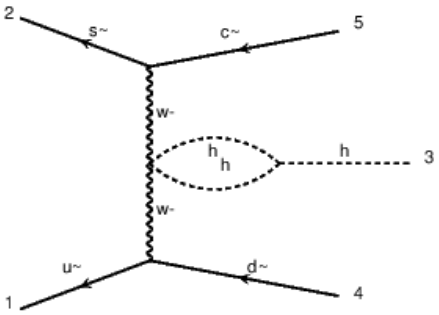

diagram 2 QCD=0, QED=5

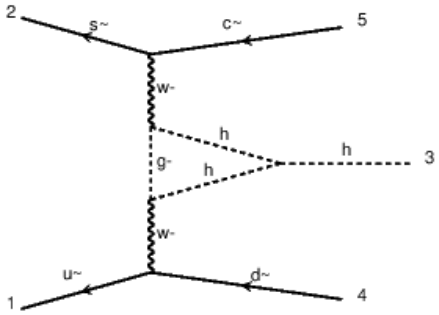

diagram 3 QCD=0, QED=5

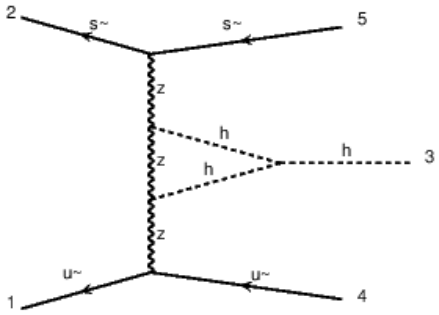

diagram 1 QCD=0, QED=5

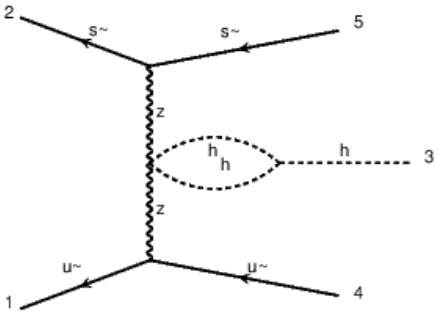

diagram 2 QCD=0, QED=5

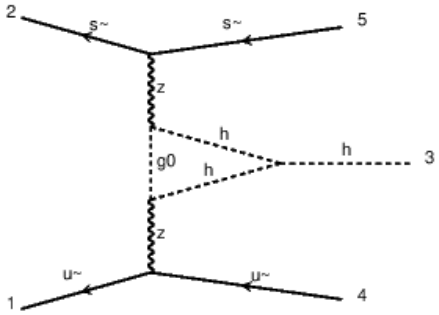

diagram 3 QCD=0, QED=5

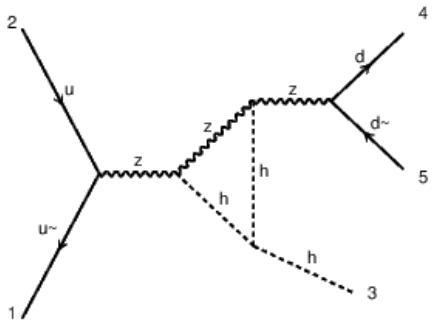

diagram 1 QCD=0, QED=5

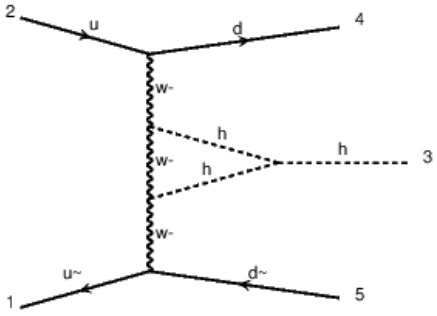

diagram 2 QCD=0, QED=5

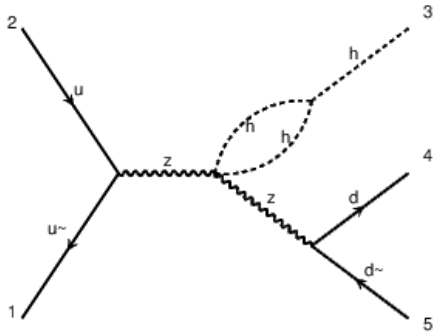

diagram 3 QCD=0, QED=5

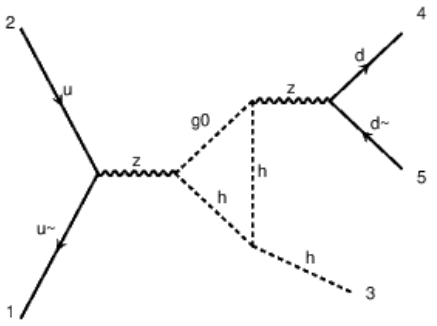

diagram 4 QCD=0, QED=5

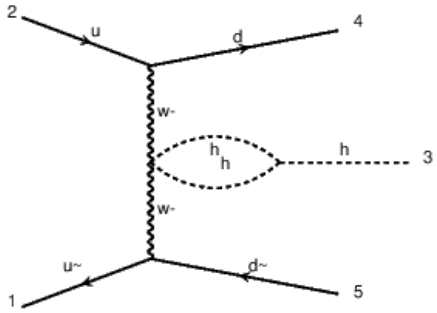

diagram 5 QCD=0, QED=5

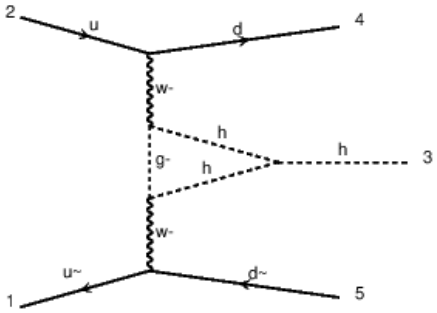

diagram 6 QCD=0, QED=5

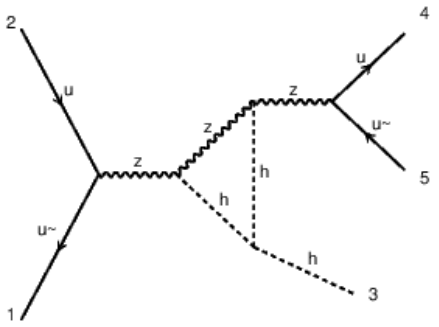

diagram 1 QCD=0, QED=5

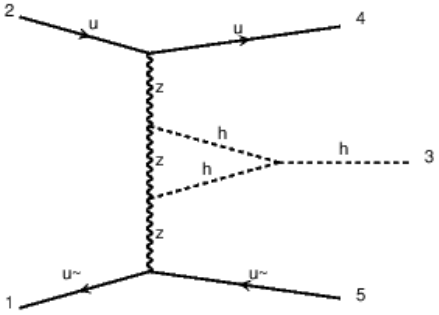

diagram 2 QCD=0, QED=5

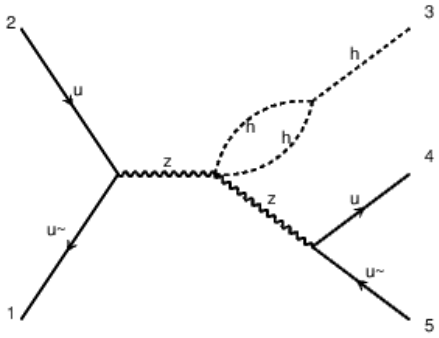

diagram 3 QCD=0, QED=5

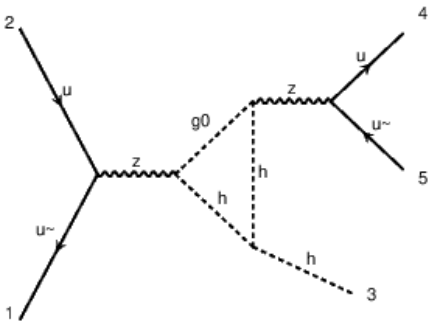

diagram 4 QCD=0, QED=5

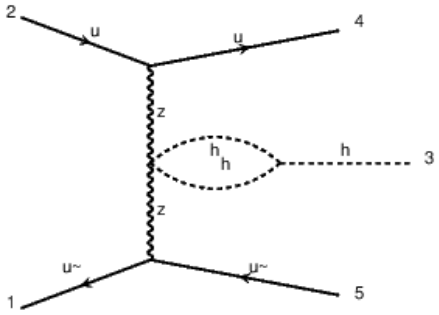

diagram 5 QCD=0, QED=5

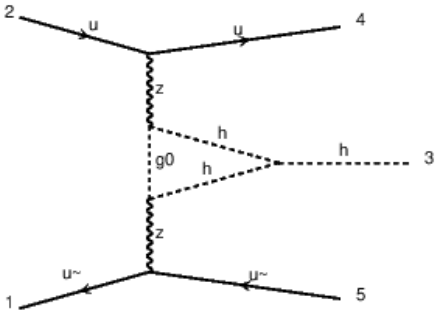

diagram 6 QCD=0, QED=5

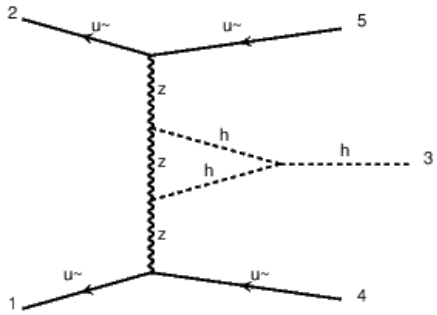

diagram 1 QCD=0, QED=5

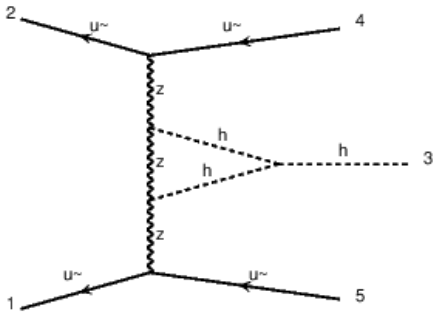

diagram 2 QCD=0, QED=5

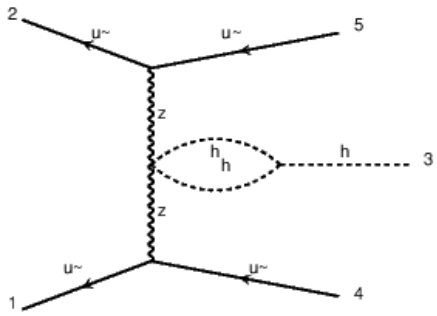

diagram 3 QCD=0, QED=5

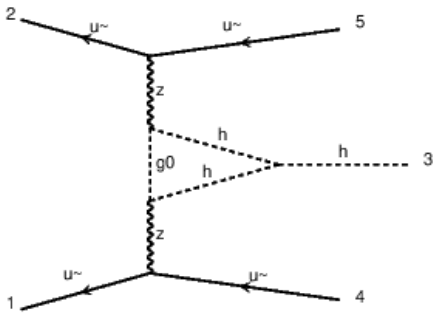

diagram 4 QCD=0, QED=5

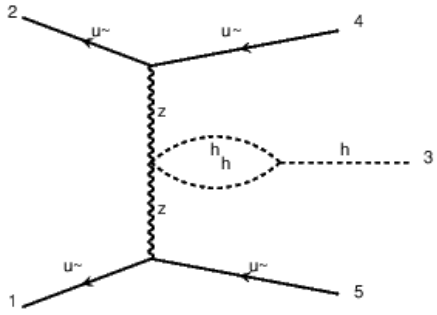

diagram 5 QCD=0, QED=5

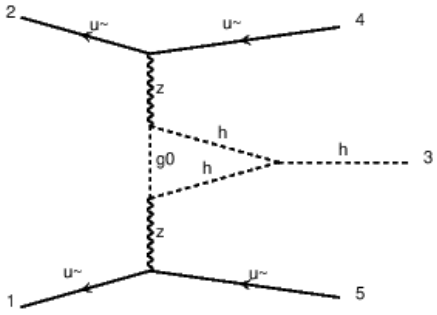

diagram 6 QCD=0, QED=5

Appendix B

INSTALLATION AND THE USE OF THE FRAMEWORK

The installation and Set-Up of the framework is provided. A short examination of the use of Trilinear-RW package is given and the difficulties are discussed. Finally, an example of a script written for our framework is provided explicitly.

B.1 Installation and Set-Up

In order to install the necessary packages open a terminal window and apply the following steps:

1. Set up the working directory.

```
mkdir produce_c1
cd produce_c1
```

2. Download the necessary packages from following links;

```
https://launchpad.net/mg5amcnlo/2.0/2.5.x/+download/
MG5_aMC_v2.5.5.tar.gz
http://www.feynarts.de/looptools/LoopTools-2.13.tar.
gz
https://cp3.irmp.ucl.ac.be/projects/madgraph/
raw-attachment/wiki/HiggsSelfCoupling/trilinear-RW.
tar.gz
```

3. Untar and validate MadGraph installation

```
tar -xzf MG5_aMC_v2.5.5.tar.gz
cd MG5_aMC_v2_5_5/
./bin/mg5_aMC
MG5_aMC> generate p p > t t~
MG5_aMC> display processes
MG5_aMC> display diagrams
MG5_aMC> output testttbar
MG5_aMC> launch
MG5_aMC> quit
```

Obtain the following;

```
=== Results Summary for run: run_01 tag: tag_1 ===

Cross-section :   505.6 +- 1.046 pb
Nb of events :   10000
```

Obtaining this result shows that your MadGraph installation is done properly.

Note that the version of MadGraph is not the latest version. This version is chosen specifically to reproduce the results in [27] with the set-up they used. One might use newer versions to check the validity of the results.

4. Set up LoopTools

```
cd ..
cd produce_c1
produce_c1]$ tar -xzf LoopTools-2.13.tar.gz
produce_c1]$ cd LoopTools-2.13/
LoopTools-2.13]$ ./configure
LoopTools-2.13]$ make
LoopTools-2.13]$ make install
```

5. Install necessary PDF file

```
MG5_aMC_v2_5_5]$ ./bin/mg5_aMC
MG5_aMC>install lhapdf6 --force
```

The PDF set used is from PDF4LHC205 distribution with LHAPDF ID: 90500 [65]. It is named as PDF4LHC15_nlo_mc, meaning that it is prepared for NLO Monte Carlo simulations.

6. Set up Trilinear-RW package

```
cd ..
cd produce_c1
produce_c1]$ tar -xzf trilinear-RW.tar.gz
produce_c1]$ mv trilinear-RW MG5_aMC_v2_5_5/
produce_c1]$ cd MG5_aMC_v2_5_5/
MG5_aMC_v2_5_5]$ cp -r trilinear-RW/hhh-model/
 ↪  models/hhh-model-new/
MG5_aMC_v2_5_5]$ cp trilinear-RW/gevirt.sh .
MG5_aMC_v2_5_5]$ cp
 ↪  trilinear-RW/vvh-loop_diagram_generation.py
 ↪  madgraph/loop/
MG5_aMC_v2_5_5]$ cp
 ↪  trilinear-RW/tth-loop_diagram_generation.py
 ↪  madgraph/loop/
```

Note that this package is necessary to calculate the C_1 parameter. The UFO model coming with this package is hhh-model-new. One has to be careful using the loop diagram generation scripts since the one written for ttH channel is different than the rest. Therefore, it should be noted and emphasized many times to remember using the correct script with each process.

7. Clone the GitHub repository to obtain the running scripts

```
MG5_aMC_v2_5_5]$ git clone
 ↪  https://github.com/easilar/CalculC1.git
MG5_aMC_v2_5_5]$ mv CalculC1/proc_* .
MG5_aMC_v2_5_5]$ mv CalculC1/run* .
```

Cloning the GitHub repository provides necessary scripts to calculate the C_1 values of individual channels with ease. The repository also provides the scripts for calculating C_1 in STXS bins for each production channel as well.

Note that one can simply prepare an *installation* script in order to simplify the process explained above to set-up the necessary programs and packages.

Following is the readme file of the Trilinear-RW package. To run the package, one has to follow the steps carefully each time running it.

```
# ********************************
# INSTRUCTIONS FOR REWEIGHTING CODE
# ********************************

=========================================
Steps to follow: ZH is used as an example
=========================================

You are inside the 'trilinear-RW' folder.

1. Copy hhh-model in 'MG5_aMC_v2_5_5/models/'.
   launch './bin/mg5_aMC' in 'MG5_aMC_v2_5_5' and generate
   ZH process with following syntax,
---------------------------------
>import model hhh-model
>generate p p > h z [LOonly= QCD]
>output hz_MC
>quit
---------------------------------

2. copy "gevirt.sh" from 'trilinear-RW' in 'MG5_aMC_v2_5_5' and run
↪  './gevirt.sh hz_MC'
   (Gives two outputs: "check_olp.inc" & "proc_ml")

3. copy "vvh-loop_diagram_generation.py"  from 'trilinear-RW' in
↪  'madgraph/loop/' and
   rename it as "loop_diagram_generation.py"
```

```
4. generate EW virtual subprocesses collected in "proc_ml" using
↪  'hhh-model' with output 'hz_ME'
   (DO NOT INSTALL 'collier'. In case you end up installing it,
   ↪  disable it in
    "MG5_aMC_v2_5_5/input/mg5_configuration.txt" by setting
    ↪  'collier = None' and remove the # in
    front of it.)

5. copy following files in 'hz_ME/SubProcesses/'
 "makefile", "check_OLP.f", "check_olp.inc" (provided+generated),
 "pmass.inc", "nsqso_born.inc", "nsquaredSO.inc" (from one of the
 ↪  subprocess folders in 'hz_ME'),
 "c_weight.inc" (from 'hz_MC/SubProcesses') and "nexternal.inc"
 ↪  (from one of the subprocess folders in 'hz_MC')

6. copy "libpdf.a", "libLHAPDF.a", 'Pdfdata', 'PDFsets' from the
↪  'lib' folder of any process already generated
   in Madgraph to 'hz_ME/lib/'

7. Go to 'hz_ME/SubProcesses/' folder and,
----------------
make OLP_static
make check_OLP
----------------
   (the output is an executable file 'check_OLP')

8. set 'True = store rwgt info' in "hz_MC/Cards/run_card.dat"

9. generate LO events in 'hz_MC' with following options
-----------------
fixedorder = OFF
shower     = OFF
reweight   = OFF
order      = LO
madspin    = OFF
-----------------
```

```
9. move the LO lhe event file (don't forget to unzip it!) to
↪  'hz_ME/SubProcesses/' and execute './check_OLP'
   (note that the input file name should be
   ↪  "events.lhe"(unweighted) and you get an output file named
   "events_rwgt.lhe" (weighted).)

10. The steps can be repeated for WH, VBF, tHj and ttH processes.
```

B.2 Example Code

In order to calculate the C_1 parameter, one has to follow a particular set of steps carefully. The calculation is more challenging when its done in STXS in the sense that there is too much room for error. The automatizing of the calculation in STXS bins gives a particular relief in that sense. A simple example of the code for HW channel is given below. As given in Chapeter 4 Section 4.5, to run the code, one should enter three inputs:

1. Lower P_T value of the bin
2. Upper P_T value of the bin
3. Number of events

The command should look like this:

```
./script_name.sh low_pt up_pt nevents
```

The code reads as following;

```
#!/bin/bash

# Input values regarding the lower, upper transverse momentum
↪  values and number of events

bin1=$1
bin2=$2
nevents=$3

# Loop diagram generation script copied for the relevant process

cp trilinear-RW/vvh-loop_diagram_generation.py
↪  madgraph/loop/loop_diagram_generation.py

# Defining the output file names monte carlo and madevent

cur_dir=hw_mc_"$bin1"_"$bin2"
cur_dir_me=hw_me_"$bin1"_"$bin2"

rm -r $cur_dir
rm -r $cur_dir_me

echo "The results will be written in the",$cur_dir

sed 's/output hw_MC/output '"$cur_dir"'/g' proc_hw_mc >
↪  proc_hw_mc_"$bin1"_"$bin2"

#

./bin/mg5_aMC < proc_hw_mc_"$bin1"_"$bin2"

sed -i -e "s/10000 = nevents /$nevents = nevents /"
↪  $cur_dir/Cards/run_card.dat
sed -i -e 's/nn23nlo = pdlabel/lhapdf = pdlabel/'
↪  $cur_dir/Cards/run_card.dat
```

```
sed -i -e 's/244600  = lhaid/90500  = lhaid/'
↪  $cur_dir/Cards/run_card.dat
sed -i -e 's/False    = fixed_ren_scale/True    = fixed_ren_scale/'
↪  $cur_dir/Cards/run_card.dat
sed -i -e 's/False    = fixed_fac_scale/True    = fixed_fac_scale/'
↪  $cur_dir/Cards/run_card.dat
sed -i -e 's/91.118   = muR_ref_fixed/102.693   = muR_ref_fixed/'
↪  $cur_dir/Cards/run_card.dat
sed -i -e 's/91.118   = muF_ref_fixed/102.693   = muF_ref_fixed/'
↪  $cur_dir/Cards/run_card.dat
sed -i -e 's/False = store_rwgt_inf/True = store_rwgt_inf/'
↪  $cur_dir/Cards/run_card.dat
#sed -i -e 's/10.0  = ptj/20.0 = ptj/' $cur_dir/Cards/run_card.dat
#sed -i -e 's/-1.0  = etaj/5.0  = etaj/'
↪  $cur_dir/Cards/run_card.dat

echo "run card manipulated"

# Pt cut for differential measurements

# Mind the folder paths!


sed -i '77a\c Pt cut for W' $cur_dir/SubProcesses/cuts.f
sed -i '78a\ ' $cur_dir/SubProcesses/cuts.f
sed -i '79a\       do i=1,nexternal' $cur_dir/SubProcesses/cuts.f
sed -i '80a\         if(istatus(i).eq.1 .and. abs(ipdg(i)).eq.24)
↪  then' $cur_dir/SubProcesses/cuts.f

if [ $bin2 -lt 0 ]
then
sed -i "81a\           if(pt_04(p(0,i)).lt.$bin1) then"
↪  $cur_dir/SubProcesses/cuts.f
else
sed -i "81a\           if(pt_04(p(0,i)).lt.$bin1 .or.
↪  pt_04(p(0,i)).gt.$bin2) then" $cur_dir/SubProcesses/cuts.f
fi
```

```
sed -i '82a\              passcuts_user=.false.'
↪  $cur_dir/SubProcesses/cuts.f
sed -i '83a\            endif' $cur_dir/SubProcesses/cuts.f
sed -i '84a\          endif' $cur_dir/SubProcesses/cuts.f
sed -i '85a\        enddo' $cur_dir/SubProcesses/cuts.f
sed -i '86a\' $cur_dir/SubProcesses/cuts.f

echo "Pt cut established"


./gevirt.sh $cur_dir/

echo import model hhh-model-new > proc_hw_me_"$bin1"_"$bin2"
cat proc_ml >> proc_hw_me_"$bin1"_"$bin2"
echo output $cur_dir_me >> proc_hw_me_"$bin1"_"$bin2"
echo collier noinstall >> proc_hw_me_"$bin1"_"$bin2"
echo quit >> proc_hw_me_"$bin1"_"$bin2"

./bin/mg5_aMC < proc_hw_me_"$bin1"_"$bin2"

cd $cur_dir_me/SubProcesses/
cp ../../trilinear-RW/makefile .
cp ../../trilinear-RW/check_OLP.f .
cp ../../check_olp.inc .
cp P0_udx_hwp/pmass.inc .
cp P0_udx_hwp/nsqso_born.inc .
cp P0_udx_hwp/nsquaredSO.inc .

cp ../../$cur_dir/SubProcesses/c_weight.inc .
cp ../../$cur_dir/SubProcesses/P0_udx_hwp/nexternal.inc .

cd ../lib/
cp ../../HHH-libs/libpdf.a .
cp -r ../../HHH-libs/Pdfdata .
cp ../../HHH-libs/libLHAPDF.a .
cp -r ../../HHH-libs/PDFsets .
```

```
cd ../SubProcesses/

make OLP_static
make check_OLP

cd ../../
cd $cur_dir/

echo order=LO > genEv_hw_mc
echo shower=OFF >> genEv_hw_mc
echo analysis=EXROOTANALYSIS >> genEv_hw_mc

./bin/generate_events < genEv_hw_mc

gunzip Events/run_01_LO/events.lhe.gz Events/run_01_LO/events.lhe
mv Events/run_01_LO/events.lhe ../$cur_dir_me/SubProcesses/

cd ../$cur_dir_me/SubProcesses/
./check_OLP | grep -B 2 "C1:" > ../../result_hw_"$bin1"_"$bin2".txt
```

This code gives a .txt file as an output in which the C_1 value is written.

TEZ İZİN FORMU / THESIS PERMISSION FORM

ENSTİTÜ / INSTITUTE

Fen Bilimleri Enstitüsü / Graduate School of Natural and Applied Sciences ☐

Sosyal Bilimler Enstitüsü / Graduate School of Social Sciences ☐

Uygulamalı Matematik Enstitüsü / Graduate School of Applied Mathematics ☐

Enformatik Enstitüsü / Graduate School of Informatics ☐

Deniz Bilimleri Enstitüsü / Graduate School of Marine Sciences ☐

YAZARIN / AUTHOR

Soyadı / Surname : .....
Adı / Name : .....
Bölümü / Department : .....

TEZİN ADI / TITLE OF THE THESIS (**İngilizce** / English) : .....
.....
.....
.....
.....

TEZİN TÜRÜ / DEGREE: **Yüksek Lisans** / Master ☐ **Doktora** / PhD ☐

1. **Tezin tamamı dünya çapında erişime açılacaktır. /** Release the entire work immediately for access worldwide. ☐
2. **Tez iki yıl süreyle erişime kapalı olacaktır.** / Secure the entire work for patent and/or proprietary purposes for a period of **two year. *** ☐
3. **Tez altı ay süreyle erişime kapalı olacaktır.** / Secure the entire work for period of **six months**. ***** ☐

***** *Enstitü Yönetim Kurulu Kararının basılı kopyası tezle birlikte kütüphaneye teslim edilecektir.*
A copy of the Decision of the Institute Administrative Committee will be delivered to the library together with the printed thesis.

Yazarın imzası / Signature ..... **Tarih** / Date .....